

Quantification of the Activity of Tectonic Fault Systems in the Region of the Gulf of Corinth (Greece)

Dissertation

zur Erlangung des akademischen Grades

Doctor rerum naturalium (Dr. rer. nat.)

vorgelegt der

Mathematisch-Naturwissenschaftlich-Technischen Fakultät

(mathematisch-naturwissenschaftlicher Bereich)

der Martin-Luther-Universität Halle-Wittenberg

von

Georgios Maniatis

geb. am 19.04.1975 in Sparta

Gutachter:

1. Prof. Dr. Christof Lempp, Institut für Geologische Wissenschaften und Geiseltalmuseum,
Martin-Luther-Universität Halle-Wittenberg
2. Prof. Dr. Helmut Heinisch, Institut für Geologische Wissenschaften und Geiseltalmuseum,
Martin-Luther-Universität Halle-Wittenberg
3. Prof. Dr. Edwin Fecker, Geotechnisches Ingenieurbüro Prof. Fecker & Partner GmbH

Verteidigt am 20. 01. 2006

Halle (Saale), 2006

urn:nbn:de:gbv:3-000009931

[<http://nbn-resolving.de/urn/resolver.pl?urn=nbn%3Ade%3A3Agbv%3A3-000009931>]

Acknowledgements

The accomplishment of this study wouldn't have been possible without the support of several persons.

First of all I would like to express my gratitude to Prof. Dr. Ch. Lempp and Prof. Dr. H. Heinisch for offering me the opportunity to undertake this project. I am sincerely thankful for their supervision and guidance throughout this study as well as for their help during the installation of the instruments in the field.

I am also indebted to Prof. Dr. E. Fecker for his interest in this thesis and for investing time and effort on reviewing it.

Furthermore, I would like to thank Prof. Dr. G. Borm and Dr. C. Schmidt-Hattenberger for their support at the beginning of this project and for kindly providing 3 Bragg-Grating-extensometers.

Also, I have to thank E. Bauch for his essential help and recommendations during the instrument installations and Dr. Ch. Hecht for his advice and suggestions throughout the labour of this project. I cannot omit the support of J. Buchantschenko, C. Bönsch, S. Grimmer, I. Patan and E. Schnerch throughout my PhD study in Halle.

In Greece, I have to thank G. Valkanas and T. Linaras for providing transport, accommodation and technical assistance. Last but not least, I am thankful to my parents, to Diana and to Niki for believing in me and supporting me throughout this effort.

The first 2 months of this project were financially supported by a short contract with the GFZ-Potsdam followed by a 6-month DFG grant. The rest of the project until the end of 2004 was financially supported by a scholarship (Jubiläumsstipendium) from the Martin Luther University of Halle.

Table of Contents

| | |
|---|----|
| 1. Introduction | 5 |
| 1.1 Geological setting | 5 |
| 1.2 Aims of the present study | 8 |
| 1.3 Structure of the present study | 10 |
| 2. Structural geology of the central part of the southern coast of Gulf of Corinth | 12 |
| 2.1 Satellite Image Analysis | 12 |
| 2.1.1 Introduction | 12 |
| 2.1.2 Applied image processing methods | 13 |
| 2.1.2.1 Image Enhancement methods | 13 |
| 2.1.2.2 Information Extraction methods | 14 |
| 2.1.3 Lineament Interpretation | 15 |
| 2.1.3.1 Criteria applied to distinguish tectonic lineaments | 18 |
| 2.2 Evaluation of the Tectonic Fabric | 20 |
| 2.2.1 General observations | 20 |
| 2.2.2 Recognized fault systems | 20 |
| 2.2.2.1 The WNW-ESE and NNE-SSW orthogonal fault system | 20 |
| 2.2.2.2 The NNW-SSE and WSW-ENE orthogonal fault system | 22 |
| 2.2.3 Succession of fault systems and variation of lineament density | 23 |
| 2.3 Stress field Evaluation | 25 |
| 2.3.1 Evaluation of stress field by observing the tectonic fabric | 25 |
| 2.3.2 Evaluation of the stress field at two regions within the area of study by the use of the Right Dihedra method | 25 |
| 2.3.3 Current stress field | 27 |
| 2.3.4 Previous stress field | 29 |
| 3. Landslide Phenomena in the Xylokastro area | 31 |
| 3.1 Area of study and collected data | 31 |
| 3.2 The orientation and location of landslides in comparison with the local tectonic fabric | 35 |
| 3.2.1 Correlation of azimuthal distributions | 35 |
| 3.2.2 Correlation of spatial distributions | 36 |
| 3.2.3 Interpretation of the azimuthal and spatial conformity between mass movements and faults | 36 |
| 3.3 Mass movement mechanisms and triggering factors | 38 |
| 3.3.1 Differentiation of factors favouring landslides | 38 |
| 3.3.2 Factors that create unstable conditions prone to accommodate mass movements | 38 |
| 3.3.3 Factors that initiate the mass movement phenomena (triggering factors) | 39 |
| 3.4 Slope examples | 42 |
| 3.4.1 Example I | 42 |
| 3.4.2 Example II | 44 |
| 3.4.3 Example III | 45 |
| 3.4.4 Example IV | 46 |
| 3.5 Finite-Element modelling of the influence of faults on the slope stability | 47 |
| 3.6 Summary and Conclusions | 51 |
| 4. Active fault monitoring at the Perachora peninsula (eastern termination of Gulf of Corinth) | 52 |
| 4.1 Instrumentation | 52 |
| 4.1.1 Introduction | 52 |
| 4.1.2 The Crack Gauge TM 71 device | 52 |

| | |
|--|-----|
| 4.1.2.1 Description and principle of function..... | 52 |
| 4.1.2.2 Methodology of use..... | 54 |
| 4.1.3 The Bragg-Grating Extensometer | 57 |
| 4.1.3.1 Description and principle of function..... | 57 |
| 4.1.3.2 Measurement of strain and deformation of the BGX rod..... | 60 |
| 4.2 The Perachora region (eastern termination of Gulf of Corinth)..... | 62 |
| 4.2.1 Geology, Tectonics and Seismicity | 62 |
| 4.2.2 The Pisias fault zone | 65 |
| 4.2.3 The Shinos fault zone | 66 |
| 4.2.4 Fault kinematics and stress field evaluation along the Pisias-Shinos fault zone.. | 66 |
| 4.3 Selection, location and description of the fault monitoring sites | 69 |
| 4.3.1 Selection of monitoring sites | 69 |
| 4.3.2 The “Pisias” fault monitoring site..... | 69 |
| 4.3.2.1 The TM71 device at the “Pisias” monitoring site..... | 71 |
| 4.3.2.2 The Bragg-Grating Extensometer (BGX) at the “Pisias” monitoring site | 73 |
| 4.3.3 The “Shinos A” monitoring site | 74 |
| 4.3.3.1 The TM71 device at the “Shinos A” monitoring site..... | 75 |
| 4.3.3.2 The Bragg-Grating Extensometer (BGX) at the “Shinos A” monitoring site | 76 |
| 4.3.4 The “Shinos B” monitoring site | 77 |
| 4.3.4.1 The TM71 device at the “Shinos B” monitoring site | 77 |
| 4.4 Evaluation of the monitoring results | 80 |
| 4.4.1 Results from the Moiré extensometer (TM71) at the “Pisias” fault monitoring site | 80 |
| 4.4.2 Results from the Bragg-Grating extensometer (BGX) at the “Pisias” fault monitoring site..... | 82 |
| 4.4.3 Results from the Moiré extensometer (TM71) at the “Shinos A” fault monitoring site | 83 |
| 4.4.4 Results from the Bragg-Grating extensometer (BGX) at the “Shinos A” fault monitoring site..... | 85 |
| 4.4.5 Results from the Moiré extensometer (TM71) at the “Shinos B” fault monitoring site | 85 |
| 4.4.6 Remarks on the observed oscillations of the displacement progress | 88 |
| 4.4.7 Comparison of the results from the Moiré and Bragg-Grating extensometers ... | 91 |
| 4.5 Kinematic evaluation and interpretation of the fault monitoring results | 95 |
| 4.5.1 The fault displacement regime at the “Pisias” monitoring site..... | 95 |
| 4.5.2 The fault displacement regime at the “Shinos A” monitoring site..... | 97 |
| 4.5.3 The fault displacement regime at the “Shinos B” monitoring site..... | 100 |
| 4.6 Correlation between the monitored displacements and the local seismicity..... | 104 |
| 4.7 An approach to the regional extension rate of the eastern Gulf of Corinth | 110 |
| 5. Summary | 113 |
| References | 117 |
| Appendix | 126 |

1 Introduction

1.1 Geological setting

The Aegean region constitutes the overriding plate of the Africa-Eurasia convergent plate system. To the south and west the Aegean micro-plate is confined by the Hellenic trench along which the African plate is consumed northwards (see fig 1.1). The Anatolian block to the east of the Aegean is driven westwards in response to the northward collision of the Arabian plate to into the Eurasian plate and part of this motion is accommodated along the right lateral branches of the North Anatolian fault (see fig 1.1).

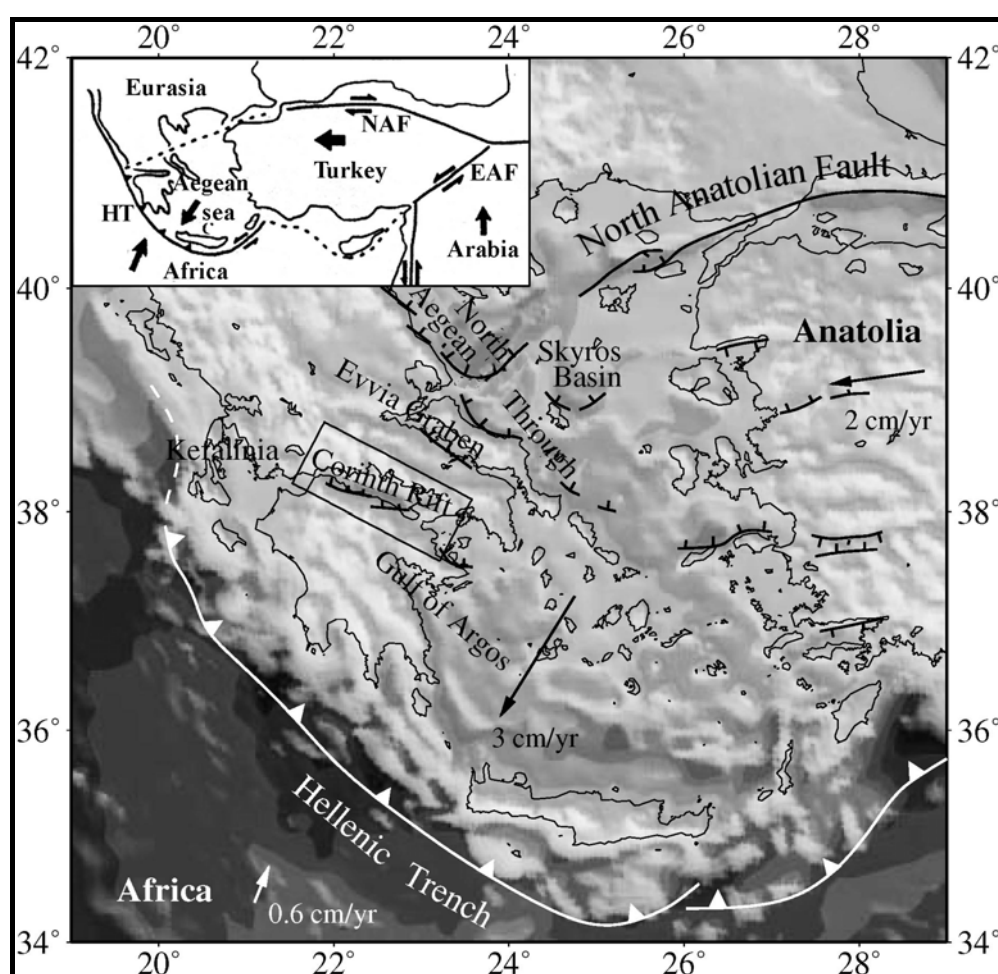


Fig 1.1: Geodynamical overview of the Aegean region (based on TIBERI et al. 2001 and DOUTSOS & KOKKALAS 2001). The arrows indicate the direction of movement relative to Eurasia (NAF: North Anatolian Fault, EAF: East Anatolian Fault, HT: Hellenic Trench; velocities after MCCLUSKY et al. 2000).

Since Miocene times, the Aegean region has been extending (ARMJIO et al. 1996) and the current extension is 3cm/year towards SSW and relative to Eurasia (fig. 1.1) (MCCLUSKY et al. 2000). The extension is attributed to multiple reasons such as the gravitational instability

of the Hellenic mountain chain, the roll back of the subducting African plate, and the westward movement of the Anatolia (DOUTSOS & KOKKALAS, 2001, ARMIJO et al. 1996, MORETTI et al. 2003 and STEFATOS et al. 2002).

The Aegean extension is expressed on the surface along a series of sub-parallel rifts which have a periodic spacing of 70km (fig 1.1)(ARMIJO et al. 1996). The most prominent of these rifts is the Gulf of Corinth rift which separates the Peloponnesus from the Greek mainland and crosses the NNW-SSE trending fabric of the Hellenides. It is WNW-ESE orientated ca. 120km long, with a mean width of 20km and a maximum depth of about 900m (see fig 1.2). In the Corinth rift the approximately N-S directed extension started in Pliocene times and still continues today (DOUTSOS & PIPER 1990, ARMIJO et al. 1996, DOUTSOS & KOKKALAS 2001, DAVIES et al 1997, BRIOLE et al 2000, AVALONE et al 2004).

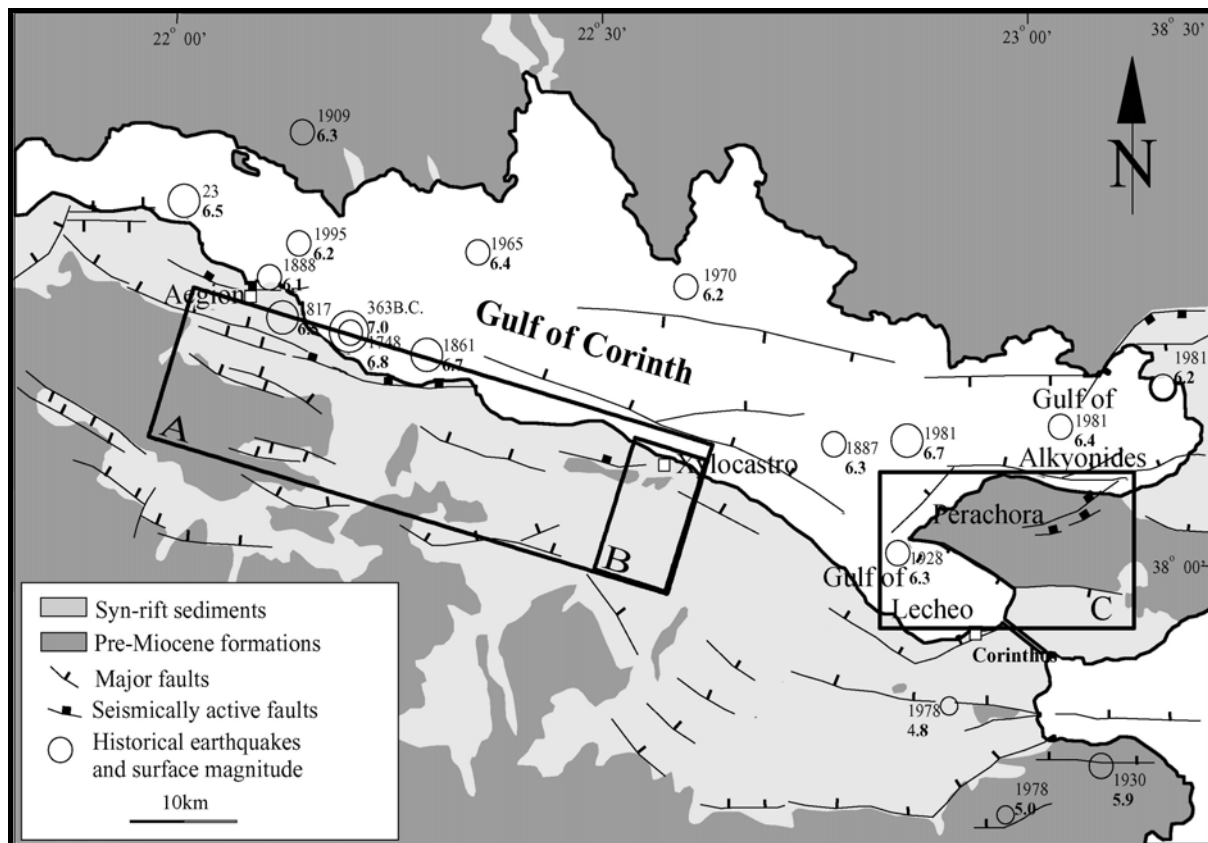


Fig. 1.2: Overview map of the Gulf of Corinth showing the general geological setting of the region (adopted from KOUKOUVELAS et al. 2001). The rectangles A, B and C indicate the respective areas of study as described in paragraph 1.3.

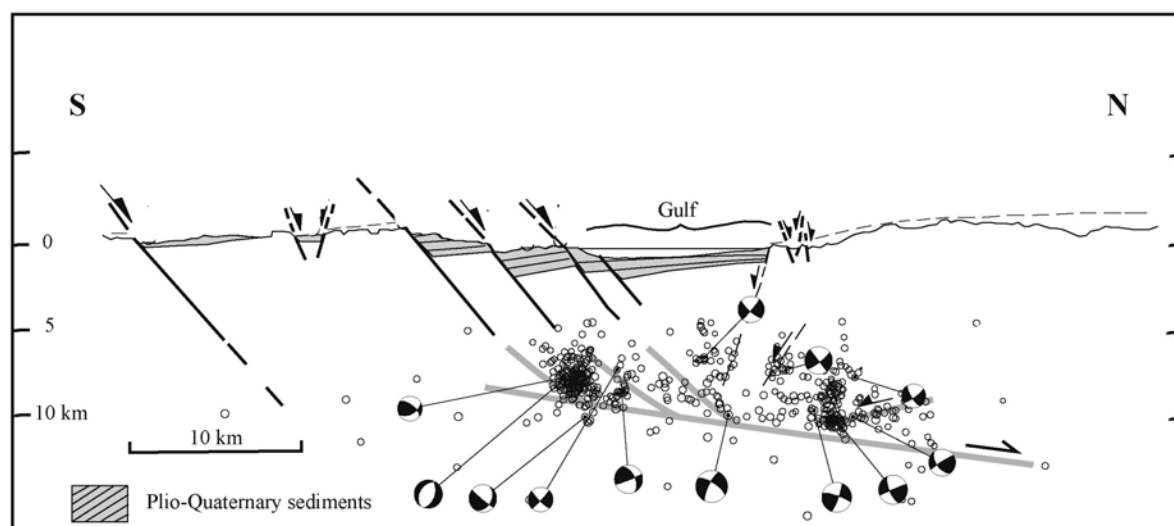


Fig 1.3: Cross section showing the hypothesis of a detachment zone at depth with the geometry a low angle normal fault, dipping approximately 15° to the north (cross section, hypocentres and focal mechanisms after RIGO et al. 1996).

Numerous major north-dipping faults outcrop on the southern coast of the Gulf of Corinth (Peloponnese) and seismic reflection surveys (e.g. STEFATOS et al. 2002) have also revealed numerous active offshore faults. The graben geometry appears to be rather complex and the major active faults observed at the surface are believed to root at depth on a detachment zone (fig 1.3) (RIGO et al. 1996, RIETBROCK et al. 1996, SOREL 2000). The geometry of the detachment zone has been proposed to be that of a low angle normal fault, dipping approximately 15° to the north (RIGO et al. 1996) and recent deep reflection seismic images (SACHPAZI et al 2003) have revealed such a low angle fault in the central Gulf of Corinth.

The Gulf of Corinth is characterized by a quite high level of historical and instrumental seismicity (AMBRASEYS & JACKSON 1990, RIGO et al. 1996, JACKSON et al. 1982, KING et al. 1985, BERNARD et al. 1997). Only in the last 40 years the seismicity of the Gulf of Corinth included six earthquakes of magnitude greater than 6 (BRIOLE et al. 2000). Furthermore, several geodetical surveys conducted in the area have shown that the Gulf of Corinth is at the present one of the most rapidly extending rifts in the world with an average extension rate between 4 and 14 mm/year (CLARKE et al. 1998, DAVIES et al. 1997, BRIOLE et al. 2000, AVALONE et al. 2004).

1.2 Aims of the present study

Up-to-date, extension rates in the Gulf of Corinth have been either indirectly calculated by geological and morphological observations (e.g. DOUTSOS & POULIMENOS 1992, ARMIJO et al. 1996) or measured as general trends by the use of GPS techniques (CLARKE et al. 1998, DAVIES et al. 1997, BRIOLE et al. 2000, AVALONE et al. 2004). Direct measurements of fault displacements had been restricted to occasional observations and geodetical surveys of large co-seismic and post-seismic movements related to distinct seismic events (JACKSON et al. 1982, KOUKOUVELAS & DOUTSOS 1996, KOUKOUVELAS 1998). Therefore, despite the detailed study of the Gulf of Corinth by several researchers in the previous years, it remained unknown to what degree the rapid extension across the Gulf of Corinth is accommodated as movements on the outcropping faults. The main objectives of the present study were to apply suitable instrumental methods in-situ on selected faults and monitor their kinematic behaviour for a period of some years (3.5 years). Through the realization of these objectives it was possible, for the first time in the Gulf of Corinth, to quantify the individual behaviour of some distinct active faults. Furthermore it was possible to investigate the kind of movements that the ongoing extension across the Gulf of Corinth is inducing on such faults in relation to the current stress field and the seismic activity.

Other principal aims of the present study were to investigate the tectonic fabric of the Gulf of Corinth region and to reach conclusions concerning the evolution of the stress field. For this purpose the entire southern coast of the Gulf of Corinth was examined by evaluating satellite images as well as fault kinematic data which were collected during fieldwork campaigns. The southern coast of Gulf of Corinth was selected due to the fact that it has been uplifted by the action of numerous major and minor normal faults and thus provides abundant information in terms of fault-kinematic indicators and syn-tectonic sedimentation. On the contrary the northern side of the Gulf of Corinth has been submerging. Therefore the important structures lay normally underwater and in comparison to the southern side only a few major faults outcrop in the area.

During the fieldwork campaigns, apart from the pure structural geological aspects, also the impact of the dense tectonic fabric on the slope stability aroused interest. Slope instability phenomena are very frequent on the southern coast of the Gulf of Corinth and this fact cannot be solely attributed to the steep morphology and the relatively poor geomechanical properties of the rocks. The presence of the dense tectonic fabric plays an additional role in this case and

the aim here was to investigate (within a selected area) the degree to which the location and orientation of the fault systems control the spatial and azimuthal distribution of the occurring landslides. ROZOS (1991) had already observed such a dependence of the landslide distribution on the distribution of faults in another area of the Gulf of Corinth. However the area studied by ROZOS (1991) consists of varying types of rocks and therefore the spatial distribution of the landslides within it might be more lithology-dependent. In the present study the landslides are studied in an area which is more homogeneous in terms of rock properties.

1.3 Structure of the present study

The present study is divided in 3 parts according to the aforementioned aims. In the first part (chapter 2), the neotectonic fabric throughout the southern coast of Gulf of Corinth is examined (area A in fig. 1.2). A first impression of the tectonic elements of the area was obtained at the beginning of the fieldwork campaigns by mapping a representative area south and southeast of Aegion (see appendix §1) as well as carrying out observations throughout the southern coast of Gulf of Corinth. In the beginning of chapter 2, Landsat TM5 satellite images are processed in order to reveal the tectonic lineaments of the area. Then, by classifying the azimuthal distribution of these lineaments, the prevailing fault systems are recognized. These results as well as the analysis of fault-kinematic data which were collected in the field are further used to evaluate the recent and previous stress fields.

The second part of the present study (chapter 3) is concerned with the frequent landslide phenomena and their relation to the local tectonic fabric. A representative area of approximately 90km² located southwest of Xylocastro (area B in fig. 1.2) was investigated. In this study area the location and geometry of the landslides is examined by analysing the collected field work data supplemented by data obtained from air-photographs. The azimuthal and spatial distributions of the landslides are then correlated to those of the local fault systems. Furthermore, the mechanisms and triggering factors of the landslide phenomena are evaluated. Finally, selected landslide examples and finite element models are presented which depict the dependence degree of the landslide occurrence on the presence of faults.

The third and final part of the present study (chapter 4) is focused on monitoring selected active faults at the Perachora peninsula which is located at the eastern termination of the Gulf of Corinth (area C in fig.1.2). These faults were activated by a series of earthquakes in 1981 and demonstrated indisputable co-seismic displacements and therefore it is certain that they are active. The displacement monitoring was carried out at three monitoring sites for periods of up to 3.5 years.

Two types of instruments, allowing displacement monitoring at sub-millimetre scale were used, a so-called TM71 extensometer which is based on the optical phenomenon of Moiré interference and a Bragg-Grating extensometer based on optic-fibre sensors. The respective monitoring methods are described at the beginning of chapter 4.

In the following parts of chapter 4, the geological setting of the Perachora peninsula is presented followed by the determination of the local stress field (analysis of fault kinematic data). The selected monitoring sites are then described in terms of geology, tectonics and instrument configuration.

Subsequently, the results from the displacement monitoring at the three fault monitoring sites are presented and commented. Not only the tectonic aspects are discussed but also a comparison between the performances of the two different monitoring instrument types is carried out. The overall displacement behaviour of each monitored fault is then interpreted in respect to the local fault kinematics and the current regional stress field. In addition, the fault displacement progress at the three monitoring sites is correlated with the contemporaneous local seismicity.

Finally the fault monitoring results are extrapolated to a regional scale across the Gulf of Alkyonides, the Perachora peninsula and the Gulf of Lecheo which comprise the eastern termination of the Gulf of Corinth. An estimation of the N-S directed extension rate at the eastern Gulf of Corinth is attempted by taking into consideration the number of major faults in the Perachora region as well as their potential degree of activity. The results are compared to the extension rates determined by GPS based studies of other researchers and a representative extension rate for the typical faults of the area is proposed.

Conclusively, the present study is an attempt to characterize the tectonic activity and some of its effects, on different scales, from regional proportions to sub-millimetre measurements at specific locations. The results from each part of the study are compared and combined in order to reach a comprehensive picture of the intense tectonic activity at the Gulf of Corinth.

2 Structural geology of the central part of the southern coast of Gulf of Corinth

2.1 Satellite Image Analysis

2.1.1 Introduction

Aiming at a more reliable structural and paleo-stress analysis, in addition to classic methods based on field data collection, satellite images were processed and analysed. The analysis was based on LANDSAT 5 TM images. These allowed the study of the neotectonic fabric of the broader area of the south coast of the Gulf of Corinth with a resolution of 30 by 30m per picture-element. Despite their relatively low resolution in comparison with air-photographs, they allow the application of several digital processing methods which result to an enhanced depiction of the tectonic lineaments. Furthermore, due to their larger coverage, satellite images offer an overview of the study area and therefore it is possible to recognize larger features of the tectonic fabric.

The orbit orientated LANDSAT 5 TM full scene (all bands), which was used, had path/row coordinates of 184/043 on the LANDSAT World Reference System and had been recorded on the 17/06/1987. On the acquisition day, the sun elevation and azimuth for this particular area was 61° and 110° respectively. The Full Scene had been already System Corrected i.e. distortions related to the acquiring sensor, the satellite and the Earth itself had been removed (EURIMAGE 2001).

The LANDSAT 5 TM full scene covers a very broad area including the central and western Peloponnesus and therefore only the area of interest was analysed. The area of interest is shown in fig. 2.1. It consists of a ca. 12km wide zone along the northern coast of Peloponnesus. The west boundary of the study area is approximately the NNE directed Selinoundas river immediately S of Aegion. From the vicinity of Aegion the study area extends ca. 12 km to the SSW to the latitude of the so-called Ponti fault (RETTENMAIER et al. 2002). This fault is considered to be the southernmost marginal fault of the Corinth basin at this area (MORETTI et al. 2003). With this width of ca. 12km the study area extends to the east the latitude of Xylokastro. Further to the east the presence of the Corinth terraces (ARMIJO et al. 1996) induces an arc-shaped non-tectonic lineament pattern which inhibits the recognition of fault traces. The area covered by the satellite image analysis overlaps the areas where fieldwork was carried out. This allows observations outside the areas studied in the field and

an overview of the tectonic fabric within a broader area, mostly covered by the typical Plio-Pleistocene sedimentary formations which characterize the evolution of the Gulf of Corinth as well as alpine basement rocks outcropping mostly as limestones of the Pindos Unit.

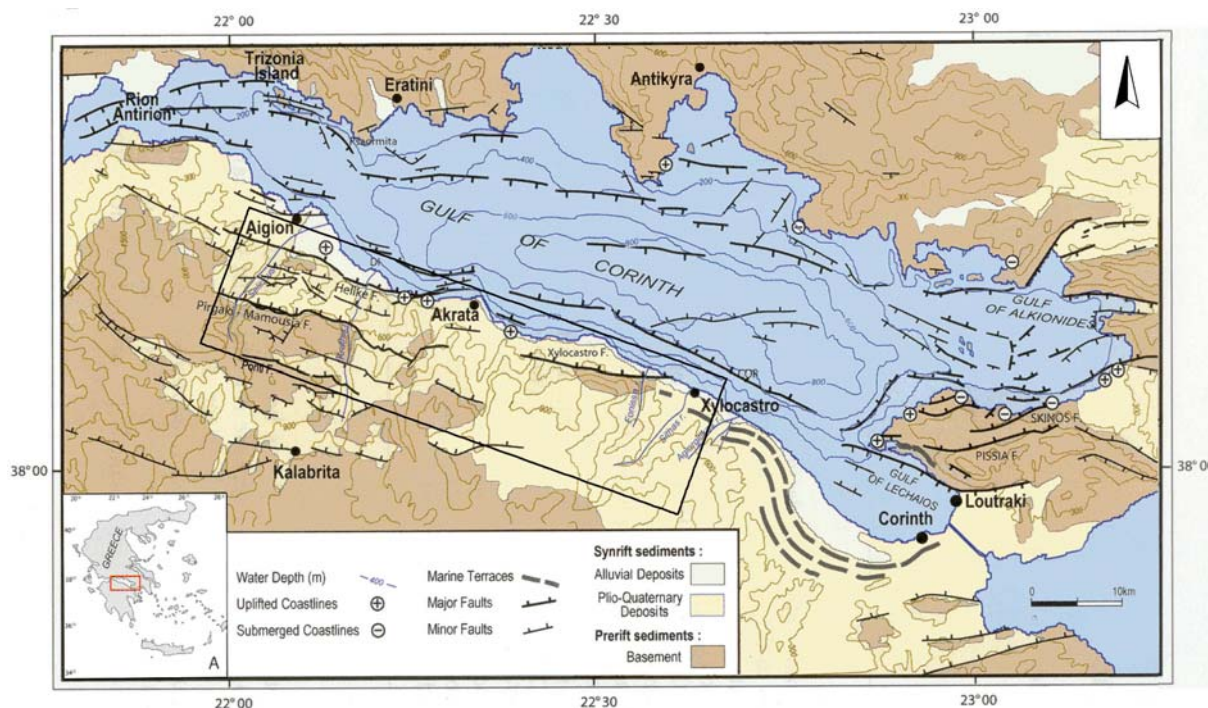


Fig. 2.1: Overview structural geological map, modified from MORETTI et. al. (2003), showing the studied area (bordered by the rectangle).

2.1.2 Applied image processing methods

The information content of satellite images can be substantially improved through the application of several image processing methods. As a consequence, the interpretation of treated images is easier and the outcome is more reliable. Taking into consideration that the main objective was to study the tectonic fabric of the southern coast of Gulf of Corinth, the efforts were concentrated on applying methods which would intensify the depiction of linear features. In this perspective, the following methods were applied:

2.1.2.1 Image Enhancement methods

-Contrast Enhancement

Virtually, each original TM band requires contrast enhancement to produce more interpretable images (SIEGAL & GILLESPIE 1980, SABINS 1996). Contrast enhancement procedures change the greyscale value (Digital Number or DN) of each picture element (pixel) in a systematic way so that a new image with more contrasted features is achieved. Here, the processing method of Linear Contrast Stretching was applied (SABINS 1996). In a simple linear contrast

stretch, the range of DN values of an image is systematically expanded to the full limits determined by byte size in the digital data. For LANDSAT 5 TM (8bit) the limits are the DN values 0 and 255.

-Add-back Highpass Filtering

This technique belongs to the so-called “edge enhancement” processes and emphasizes the signatures of edges on images (SABINS 1996). As a result, small structural features and lineaments not readily visible on the original satellite images are accentuated. The greyscale value of each picture element (pixel) is re-calculated by adding to it its difference to the average greyscale value of the surrounding picture elements. The extent of the area around each picture element which is taken into account for the calculations is defined by a rectangular matrix. A 5x5 matrix was used to apply the add-back highpass filtering on the satellite images during this study i.e. the average greyscale value of the 24 surrounding picture elements was taken into account for the calculation of the new greyscale value of each picture element.

-Directional edge enhancement

During the interpretation and depending on the degree of difficulty to distinguish certain lineament groups, directional filtering was additionally performed (SABINS 1996, KRONBERG 1985). This process is based on the same principle with the add-back highpass filtering but it preferentially enhances linear features that trend to a specific direction.

2.1.2.2 Information Extraction methods

-Principal component analysis

Principal Component Transformation is a de-correlation procedure which reorganizes by statistical means the DN values from as many of the spectral bands as we choose to include in the analysis (GILLESPIE 1980, BURGER 1981). It was carried out by means of the freeware program PIT (LOVE 1999). The Band 6 (Thermal IR spectral range 10.40-12.5 μm) was excluded from this procedure on account of its insufficient resolution (120x120m) for structural geological observations. The result the Principal component analysis based on bands 1 to 5 and 7 consists of 6 new uncorrelated Primary Component Images (PC1 to PC6). Such images may contain features which are more apparent than in individual bands. The first Primary component image (PC1) has the maximum amount of variation and provides the best differentiation of morphological and lithological features (SPRENGER 1996).

2.1.3 Lineament Interpretation

KRONBERG (1985) suggested that Band 5 (SWIR spectral range 1.55-1.75 μm) is particularly useful for the assessment of structural features, whereas SPRENGER (1996) noted that Band 5 may include disturbing information deriving from vegetation effects. As a basis for the evaluation of geological structures SPRENGER (1996) used Band 4 images (NIR spectral range 0.76-0.90 μm) instead.

At the present study Bands 4 and 5 as well as the first Primary Component image (PC1) were treated with the Image Enhancement methods described above and all of them proved to be advantageous for the structural geological lineament interpretation. It was therefore decided to evaluate the tectonic fabric of the south coast of the Gulf of Corinth by using all three types of images.

The Image Enhancement procedures as well as the lineament interpretation were carried out on a standard PC by using the Adobe PhotoshopCS software. The processed images were interpreted by viewing them on a standard PC monitor with high resolution. During the interpretation, different zoom factors were used from 50% to 400% in order to examine the extent and the continuation of the lineaments at different scales.

In order to avoid any potential distortion of image information due to image rotation, it was decided to process the satellite images at their original orientation (orbit orientated). The orbit orientation of the satellite image was 10.03° which means that a line with 0° azimuth in the image has 0+10.03° azimuth in reality. Therefore the strike directions of the recognized lineaments were afterwards mathematically rotated to their real orientation in reference to the North by adding 10.03°.

The lineaments of fig. 2.5 are the cumulative result of the interpretation of the processed bands 4 and 5 and of the First Primary Component (PC1) (seen in fig. 2.2, 2.3, 2.4 respectively). The advantage of this kind of lineament interpretation is that it reveals tectonic lineaments not readily visible in the field and therefore not contained in the available geological maps. Nevertheless, the existence and orientation mostly of largest faults in fig. 2.5 was confirmed by ground checks during fieldwork or by geological maps with a scale of 1:50000 (I.G.M.E. 1989 & 1993) in the case where these faults lay outside fieldwork areas. In addition, an area located southeast of Aegion, containing several lithologies and faults of

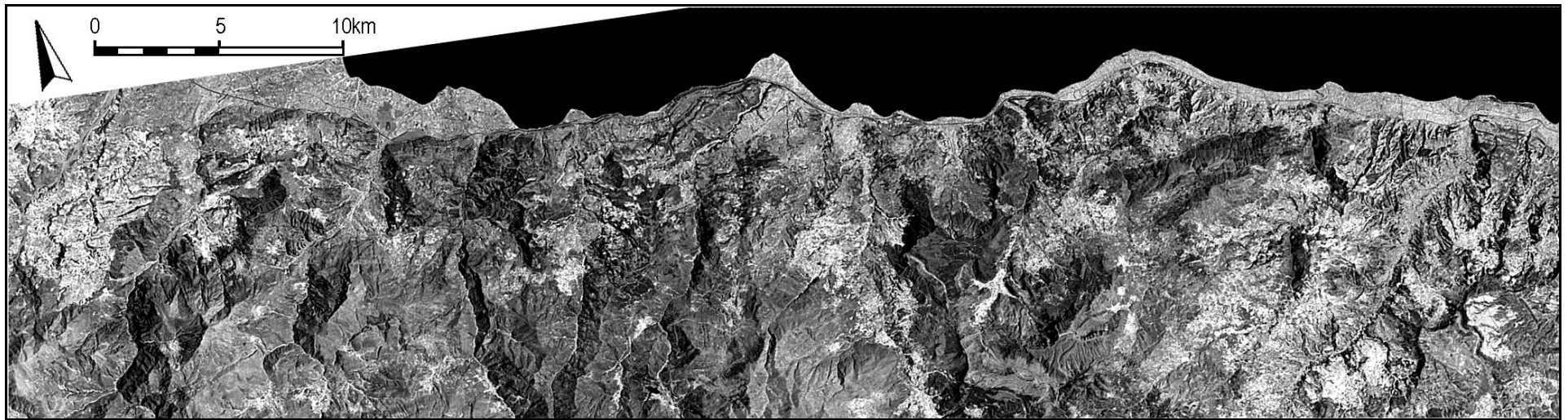


Fig. 2.2: Band 4 with Add-Back-Highpass and Contrast Stretching.

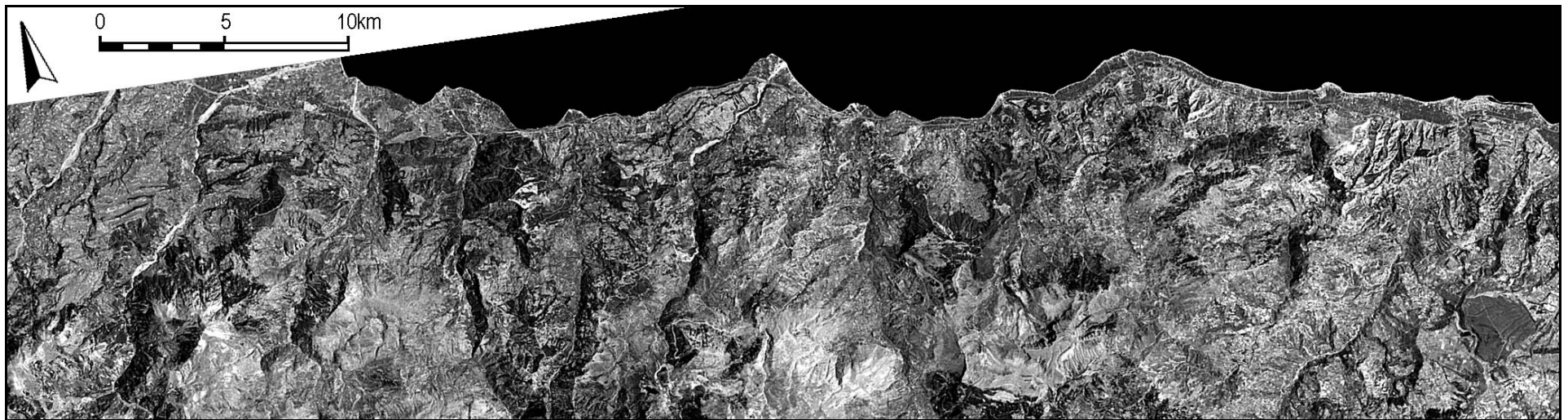


Fig. 2.3: Band 5 with Add-Back-Highpass and Contrast Stretching.

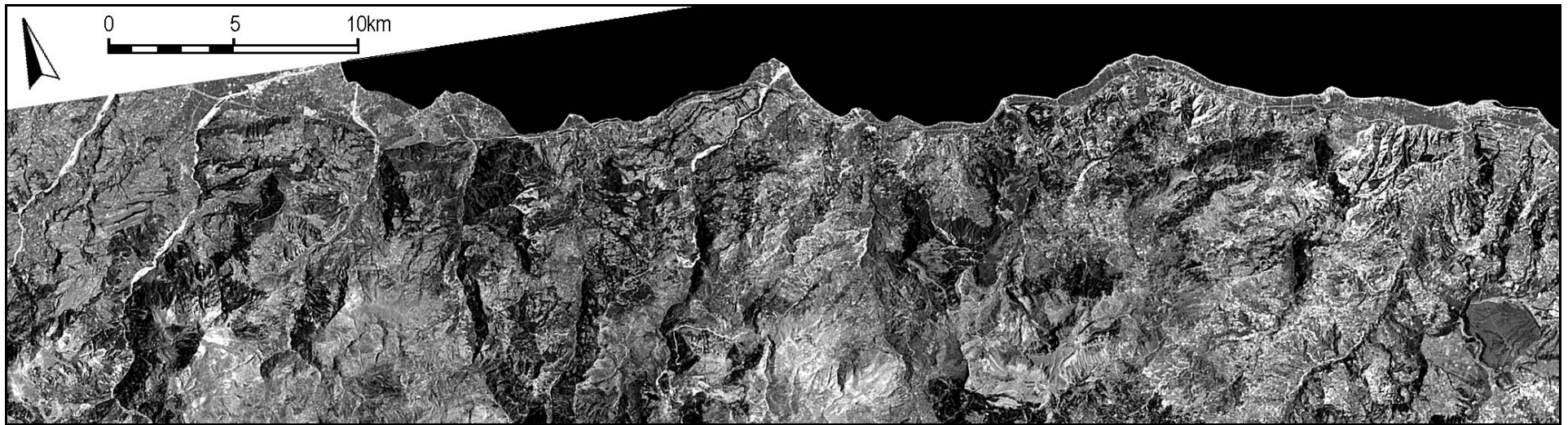


Fig. 2.4: Primary Component 1 (PC1) with Add-Back-Highpass and Contrast Stretching.

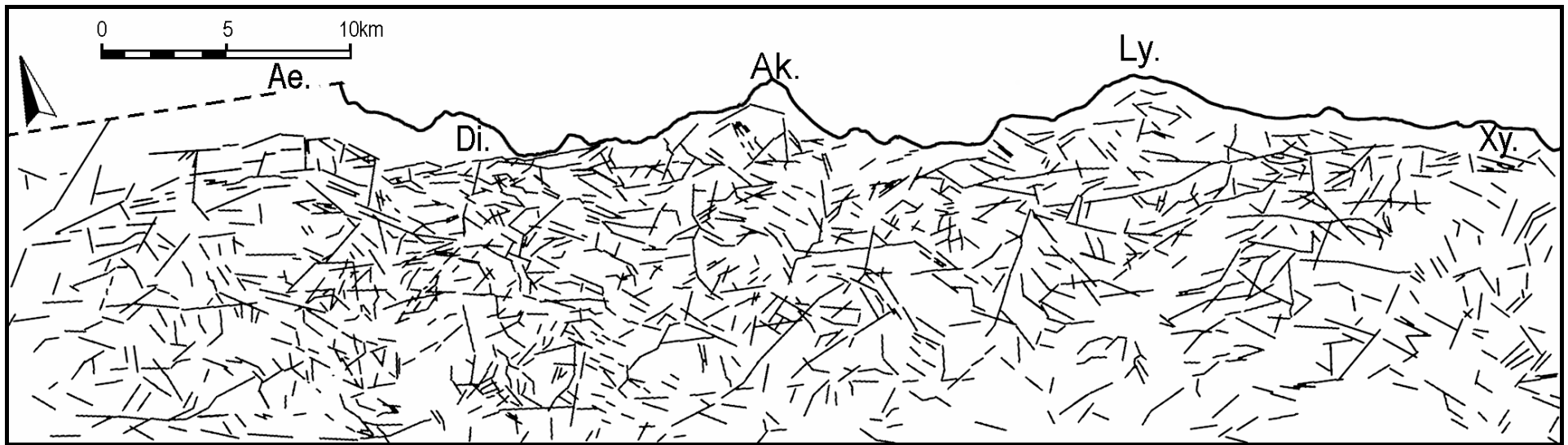


Fig. 2.5: Lineament interpretation of Band 4, Band 5 and PC1. Ae. Aegion, Di. Diakofto, Ak. Akrata, Ly. Lykoporia, Xy. Xylocastro.

different lengths and orientations, was mapped at a scale of 1:50000 (appendix §1). The mapping results were used as an additional verification of the satellite data interpretation. Not all lineaments in bands 4, 5 and PC1 are necessarily of tectonic origin and the classification of a linear feature as a tectonic lineament is a subjective matter depending on the impact of the satellite images on each viewer (SPRENGER 1996). The final data set comprised of the orientation (strike direction) and length of each recognized lineament and a total of 1454 lineaments was registered (fig. 2.5). These lineaments were classified as faults according to the following criteria.

2.1.3.1 Criteria applied to distinguish tectonic lineaments

It was attempted to recognize and exclude lineaments of anthropogenic origin by taking into consideration the position of roads and other features, such as cultivated areas, registered in topographical maps (H.M.G.S 1989a, 1989b, 1989c). Another common case of linear features which are not necessarily tectonic lineaments is that of tonal variations on either side of watersheds due to lightning and shadow effects. As opposed to the previous kind of tonal variations, the ones induced by lithological changes are of great importance. Linear or curvilinear expressions of such tonal contrasts were mostly considered as faults. In reality, there is always the possibility that a minority of such features represents simple stratigraphical transitions within inclined sediments. Or, when it comes to linear features within alpine basement, a minority of them may also be an expression of the older alpine tectonic fabric (i.e. thrusts, folds and fractures due to alpine internal deformation). Special attention was paid to the interpretation of the drainage pattern. The segments of torrent streams with a straight, linear character which usually form crooked linear successions were generally recognized as fault controlled (i.e. eroding along fault traces, fig. 2.6a). Successively aligned segments of valleys (fig. 2.6b) may also be geomorphic expressions of tectonic lineaments. In addition, branches differentiating from typical dendrite drainage patterns were also generally identified as being of tectonic origin (fig. 2.6c).

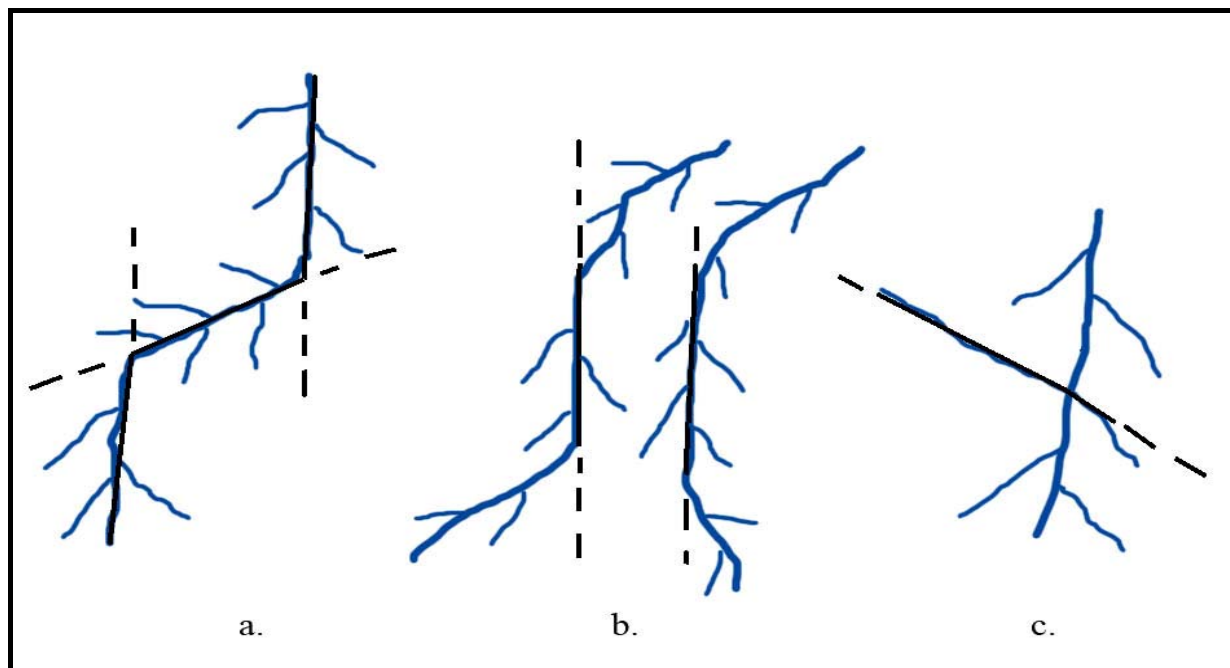


Fig. 2.6: Schematic drawing showing tectonic interpretations of drainage patterns. The fault traces are shown as black lines. a. Straight stream segments forming a crooked line pattern. b. Successively aligned segments (middle) of two streams c. Branch diverging from the typical dentritic drainage pattern.

2.2 Evaluation of the Tectonic Fabric

2.2.1 General observations

Two characteristics, regarding the azimuthal and spatial distribution of the lineaments, which can be readily observed in fig. 2.5, are a preferred orientation along four specific directions throughout the entire area and a variation of density. Most of the recognized lineaments have one of the following trends: WNW-ESE, NNE-SSW, NNW-SSE or ENE-WSW. Additionally a variation of density from east to west can be seen. In the area south and south-west of Xylocastro, the lineament density is relatively low and it increases gradually towards the area south of Diakofto to the west, where it reaches its maximum and then drops slightly further to the west.

2.2.2 Recognized fault systems

2.2.2.1 The WNW-ESE and NNE-SSW orthogonal fault system

The rose diagrams a and b in fig. 2.7 depict the lineament distribution throughout the entire studied area in terms of frequency and length azimuthal distribution. These diagrams show that the most frequent structural elements in the study area are WNW-ESE orientated faults. The faults belonging to this system strike obliquely to the shore in a right stepping arrangement. Although it is possible to distinguish fault traces with an extent of more than 20km (e.g. Pyrgaki fault in fig. 2.1 and 2.5), the faults are segmented. Fault segmentation is a common characteristic of all the faults in the Gulf of Corinth (DOUTSOS & POULIMENOS 1992, ROBERTS 1996a, KOUKOUVELAS & DOUTSOS 1996) and in the case of the WNW-ESE orientated fault system the segments, as observed in the processed satellite images, have lengths between 80m and 6km and an average length of 0,9km. The rose-diagram in fig. 2.7b also shows that the total length of the WNW-ESE faults is greater in comparison to the other fault systems. The above observations demonstrate that the WNW-ESE orientated faults comprise the dominating fault system of the south coast of the Gulf of Corinth. This fault system is responsible for the formation of the Gulf of Corinth to its present form (POULIMENOS et al. 1989, ARMIJO et al. 1996). The majority of the faults belonging to this system are seen in the field as N- to NNE-dipping normal faults accompanied by antithetic faults of the same strike direction. This setting accommodates the extension and it is possible to distinguish different orders of WNW-ESE faults according to their segment lengths: the longer ones delineate structural blocks whereas the shorter secondary ones accommodate lesser amounts of extension within these blocks.

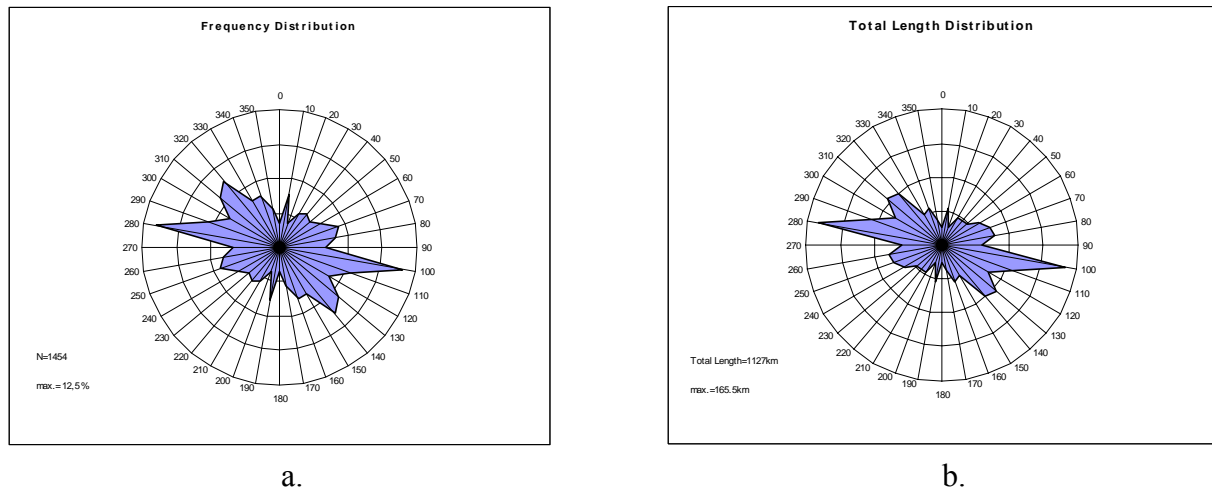


Fig. 2.7: Rose-diagrams showing the distribution of lineaments throughout the entire area of study. Rose diagram a. shows the distribution of lineaments in terms of frequency and rose diagram b. the distribution of total lineament length.

Numerous WNW-ESE faults and fault segments terminate on NNE-SSW trending faults. The latter are represented by a relatively small but clear concentration on the frequency and length distribution rose diagrams and their segments have lengths between 0,2m and 1,7km with an average of 0,6km. The NNE-SSW orientated faults are usually responsible for the development of the NNE trending valleys with successive linear segments which incise through the WNW-ESE orientated fault escarpments (figures 2.2, 2.3, 2.4, 2.5). In the field they usually demonstrate steep dips (75° - 90°) and normal or oblique slip. Previous works based on interpretation of air-photographs (for example DOUTSOS et al. 1985, POULIMENOS 1989, POULIMENOS 1993 and POULIMENOS 2000) demonstrate a more frequent presence of the NNE-SSW in comparison with the present study. Conversely, KRONBERG et al. (1981) based on a lineament interpretation of datasets of older LANDSAT missions for central and SW Greece also observed a relatively lower frequency of the NNW-SSW fault system in the Gulf of Corinth compared to the air-photograph based studies. In the present study there might be two reasons for the potentially underestimated frequency of the NNE-SSW lineaments. First, more NNE-SSW trending river segments could be fault related and therefore an additional number of lineaments should have been assigned to them. Second, the sun azimuth of 110° at the time of the satellite image acquisition is causing NNE-SSW orientated shadow areas in which some NNE-SSW lineaments may be hidden.

POULIMENOS (1993, 2000) described the NNE-SSW faults as transverse faults that are either inherited passive discontinuities that have been reactivated during extension, or as a transfer faults connecting the WNW-ESE orientated normal faults. In any case, their movement is

guided by the movements along the WNW-trending normal faults (MOREWOOD & ROBERTS 1997).

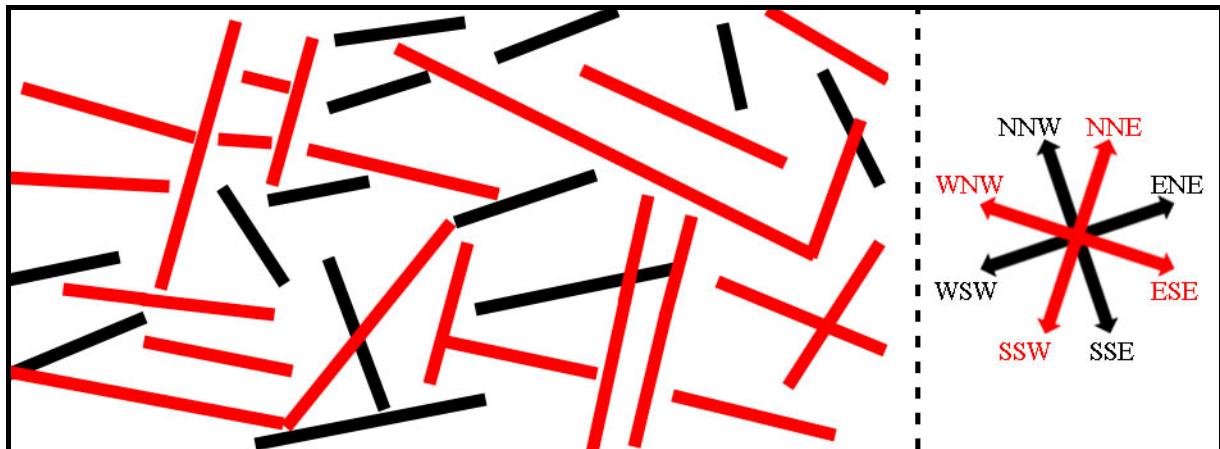


Fig. 2.8.: Sketch depicting the two prevailing orthogonal fault systems in the study area. The dominant and younger orthogonal fault system, depicted with red colour, has overprinted the older orthogonal fault system (depicted with black).

Nevertheless, the presence of the NNE-SSW fault system is very significant in combination with the most important system of the WNW-ESE trending faults because these two sets comprise an orthogonal system (see fig. 2.8) which controlled the Plio-Pleistocene sedimentation processes by forming WNW-ESE orientated grabens separated by NNE-SSW orientated barriers (POULIMENOS et al. 1989, POULIMENOS 1993). This pattern is the most characteristic one throughout the entire area of study despite density variations.

2.2.2.2 The NNW-SSE and WSW-ENE orthogonal fault system

Another discernible fault system in the rose diagrams of fig. 2.7 is trending NNW-SSE to NW-SE. It can be distinguished in fig. 2.5 that despite their relatively high frequency the faults of this system have in general a more discontinuous character as they usually terminate on the WNW-ESE faults described above. An equally important characteristic is that they frequently occur isolated in areas not crossed by WNW-ESE and NNE-SSW faults. Due to these facts their lengths are relatively short in comparison with the fault lengths of the previously described orthogonal system. Their mean length is 0,7km and the maximum length is 2,4km. The lineament interpretation in fig. 2.5 indicates that the frequency of these faults increases towards the west and that their density is relatively higher in a 5km wide zone extending to the south from Diakofto town. In this zone large WNW trending tilted blocks are absent (POULIMENOS et al. 1989) and the presence of long WNW-ESE trending fault segments withdraws.

Perpendicularly to the group of faults described above there is a system of mainly ENE-WSW trending faults. They also display a discontinuous character and have lengths of 130m to 3km and an average length of 0.8 km. This system is not completely separated from the WNW-ESE faults as its distribution exhibits a connection to the ESE direction in the rose diagrams a and b of fig. 2.7. Furthermore, in the rose diagrams it is obvious that its trend reaches a NE-SW orientation to a certain degree. The NNW-SSE and WSW-ENE directed faults create a second order orthogonal system (depicted with back colour in fig. 2.8).

2.2.3 Succession of fault systems and variation of lineament density

From its geometric relation to the first order WNW-ESE and NNE-SSW orthogonal system, as it is described in the previous paragraphs, it is concluded that the second order orthogonal fault system is older. DOUTSOS et al. 1987 recognized this chronological succession in the wider area of western Greece. The NNW-SSE and WSW-ENE faults have their origin to the general uplift following the thrusting and faulting of the external Hellenides after the middle Miocene (ZELILIDIS et al. 1988). The NNW-SSE faults are parallel to the fold axis and thrust structures of the orogene and the ENE-WSW faults strike perpendicularly to these structures. This orthogonal fault system has a dominating presence in the Gulf of Patras to the west of Gulf of Corinth (DOUTSOS et al. 1985), whereas in the Gulf of Corinth its presence is secondary (fig. 2.7) as it has been gradually superimposed by the younger system described in paragraph 2.2.1.1. This gradual superposition takes place since Pliocene as the Aegean extension propagates to the West causing the Gulf of Corinth to open (ZELILIDIS et al. 1988, POULIMENOS 1993, ARMIJO et al. 1996, CLARKE et al. 1998, DOUTSOS & KOKKALAS 2001). This gradual change may be a plausible explanation why the pre-existing WSW-ENE orientated fault group in rose-diagram a is not completely separated from the WNW-ESE fault group i.e the WSW-ENE orientated faults were superimposed by almost E-W striking ones and finally by the WNW-ESE as the new regime (Aegean extension) gradually replaced the older one and became the main stress influence in the area (POULIMENOS et al. 1989).

The second general characteristic of the lineament interpretation of fig. 2.5 is an increase of lineament density from E to W. Two explanations can be given for this feature. On the one hand there is the change of lithologies from west to east. The presence of soft, easily erodible formations increases from west to east and at the same time the presence of hard conglomerates and outcropping basement (limestone) decreases. In addition, the high degree of erosion which is usually manifested as the formation of badlands, especially in the area S

and SW of Xylocastro, may inhibit the recognition of tectonic lineaments in the satellite imagery thus resulting to a decreased lineament density. In such areas the processed Band 5 yielded better results in terms of lineament enhancement. On the other hand, there is a change of the tectonic fabric. Towards the west apart from the characteristic and most frequent ESE and NNE faults of the Gulf of Corinth the other orthogonal fault system (of NNW and SSE faults) is gradually increasing its frequency to become the dominating system further to the west, outside the study area, in the Gulf of Patras (DOUTSOS et al. 1985).

2.3 Stress field Evaluation

2.3.1 Evaluation of stress field by observing the tectonic fabric

The tectonic fabric as evaluated through the satellite image processing can be used to ascertain the stress field of the central part of the southern coast of Gulf of Corinth (study area in fig.2.1). The dominating north dipping WNW-ESE faults are the ones accommodating the extension responsible for the formation of the Gulf of Corinth rift to its present form (e.g. POULIMENOS et al. 1989, ARMIJO et al. 1996, ROBETS & JACKSON 1991) and such faults are present not only onshore as seen in the field and in the satellite images but also offshore as numerous geophysical (seismic imaging) studies have shown (e.g. BROOKS & FERENTINOS 1984, HIGGS 1988, LIMPERIS et al. 1998, STEFATOS et al. 2002, SACHPAZI et al. 2003 CLEMENT et al. 2004). From a kinematical point of view the WNW-ESE trending normal faults demonstrate in the field mostly dip-slip vectors of motion. In the Gulf of Corinth, as in any other areas under an extensional regime, the σ_1 stress axis (maximum compressive stress axis) is expected to be sub-vertical while σ_2 and σ_3 (intermediate and minimum compressive stress axes) are laying sub-horizontally. Hence, the σ_3 stress axis of the stress field responsible for the creation of the WNW-ESE orientated normal faults with dip-slip kinematics should be orientated perpendicularly to the strike direction of these faults. In addition, POULIMENOS et al. (1989) pointed out that the σ_3 stress axis is parallel to the NNE trending transfer faults in the Gulf of Corinth in a similar way as in the Basin and Range Province. In the rose-diagrams of fig. 2.7 it can be seen that the maximum distribution of WNW-ESE trending faults is N100°E orientated and is decreasing gradually toward the direction of N110°E. In the same rose diagrams the NNE-SSW directed faults have a maximum frequency at N10°E direction. From the above observations it can be concluded that the azimuth of the σ_3 should be approximately between N10°E and N20°E. Consequently, the σ_2 stress axis which should also lay sub-horizontally is expected to have an azimuth of approximately N100°E.

2.3.2 Evaluation of the stress field at two regions within the area of study by the use of the Right Dihedra method

The above mentioned considerations were verified by applying the Right Dihedra Method of Angelier (ANGELIER & MECHLER 1977) on two samples of fault-kinematic data collected in the field from two separate regions respectively. The datasets consisted of striation directions and the respective fault planes. According to the Angelier method and by using the TectonicsFP programme (REITER & ACS 2003), compressive and distensive dihedra were calculated for each fault plane. Each counting point in a 20-ring grid is assigned a value of 1 if

located inside of a compressive dihedron. All counting points are superimposed and contoured. The σ_1 stress axis (maximum compressive stress axis) is located in the area with the greatest density and the σ_3 (intermediate compressive stress axis) in the area with the lowest density.

The first region extends from the Aegion- Akrata coastline to the south as far as the Pyrgaki-Mamousia fault and the second one is located west of Xylocastro town on the footwall of the Xylocastro fault (fig. 2.1). In these areas several major faults and fault zones cut through limestone and hard conglomerate outcrops and therefore the kinematic indicators (mostly lineations and fault corrugations) are well preserved on the exposed fault planes.

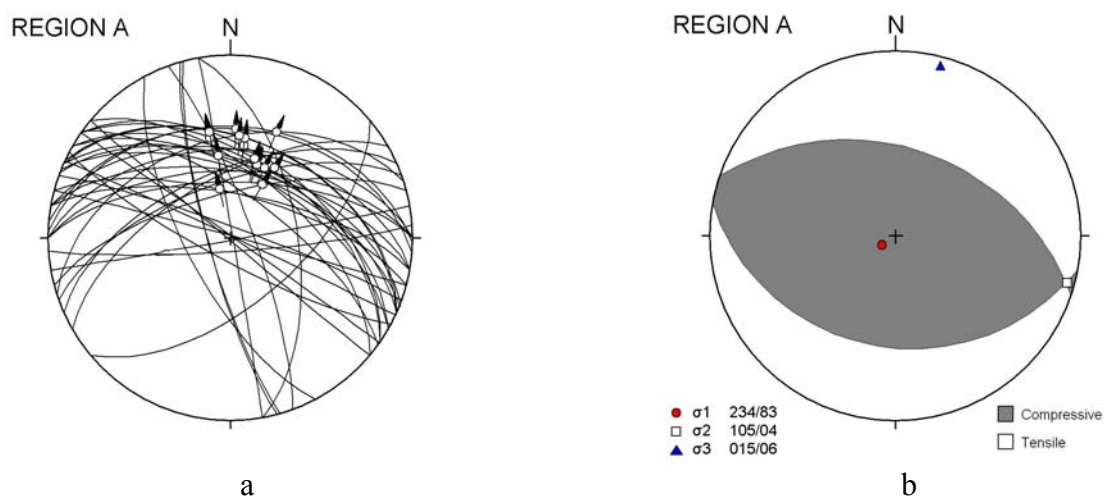


Fig. 2.9: a. Lower hemisphere fault plane projections and available slip vectors for the region extending from Aegion- Akrata coastline to the south as far as the Pyrgaki-Mamousia fault (Region A). b. Stress-field interpretation of slip vectors and the respective faults by the use of the Right Dihedra method.

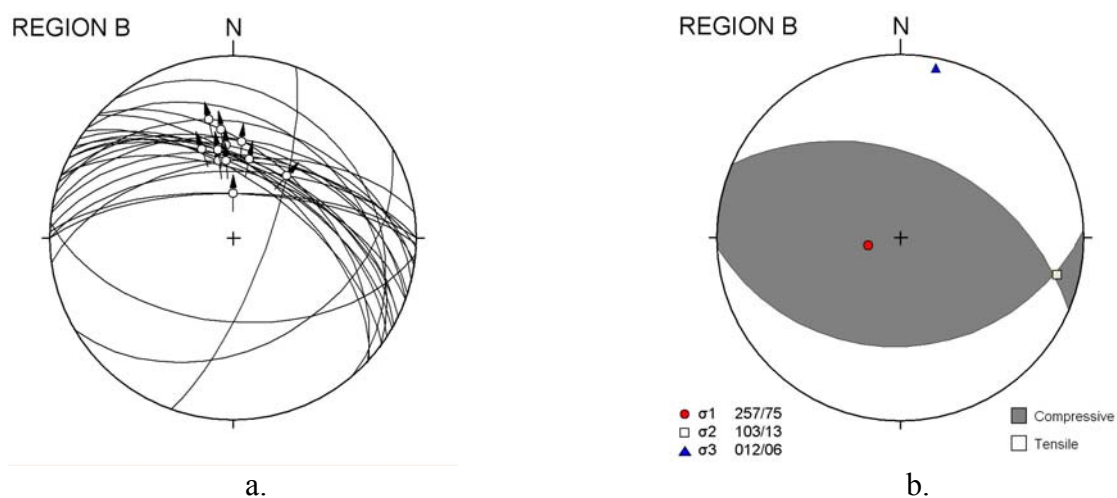


Fig. 2.10: a. Lower hemisphere fault plane projections and available slip vectors for the region located west of Xylocastro town on the footwall of the Xylocastro fault (Region B). b. Stress-field interpretation of slip vectors and the respective faults by the use of the Right Dihedra method.

The Right Dihedra Method yields for the region south of the coastline between Aegion and Akrata (see fig. 2.1 for locations) a σ_3 directed at 015/06 (fig. 2.9). This is in agreement with the inference from the evaluation of the tectonic fabric that the extension is NNE directed. Furthermore, the σ_2 principal stress axis according to the results is plunging towards ENE (plunging direction 105/04) and as expected the σ_1 is sub-vertical (plunging direction 234/83). The results from the faults located within the limestone outcrop west of Xylocastro town are presented in fig. 2.10. The direction of the σ_3 principal stress axis is 012/06 and also supports the deduction of a NNE directed extension. Similar to the Region A the σ_2 stress axis plunges toward 103/13 and the σ_1 stress axis towards 257/75.

Despite the fact that the results from the Right Dihedra analysis are representative only for the respective regions A and B, they can support the inferred NNE directed extension throughout the study area. The reasons for that are, on one hand, the relatively homogenous tectonic fabric and the relative small distance between the regions. On the other hand, the two regions lay at the eastern and western end of the area of study respectively and it can be assumed that the stress field between them cannot vary significantly.

Concerning the orientation of the σ_3 and σ_2 principal stress axes it should be noticed that both of them lay almost horizontally. It is therefore possible that in other regions within the studied part of the south coast of the Gulf of Corinth these axes may plunge to the opposite azimuthal direction i.e. the σ_3 may be directed towards SSW and the σ_2 towards WNW. However, this potential discrepancy is not in contradiction with the conclusion that the overall extension in Gulf of Corinth is NNE-SSW orientated.

2.3.3 Current stress field

The same stress field as inferred above on the basis of the satellite image interpretation, field observations and fault slip data was also ascertained by other writers who used similar methods of paleostress analysis. Most representative are the works of DOUTSOS et al. (1985) POULIMENOS et al. (1989), POULIMENOS (1993), POULIMENOS (2000) and DOUTSOS & KOKKALAS (2001). All these studies were based on conventional structural geological methods combining data from field observations, fault slip analysis and evaluation of air-photographs from parts of the Gulf of Corinth or of more regional scales including the Gulf of Corinth. For the area of study all of them propose an almost horizontal σ_3 orientated at N10°-20°E, a WNW-ENE orientated also sub-horizontal σ_2 and a sub-vertical σ_1 . This stress field

setting is the currently active one at the Gulf of Corinth. This is attested in the field by the fact that the WNW-ENE normal faults disrupt recent sediments and modern soil horizons and display co-seismic offsets of nearly dip-slip character (e.g. the Helike 1861 and Aegion 1995 earthquake ruptures).

Moreover, other geo-scientists have attempted to study the current regime of tectonic deformation of the Gulf of Corinth by analysing the local seismicity and microseismicity or by applying GPS-based geodetic methods.

For example PAPAACHOS (1975), PAPAACHOS et al. (1981) and TSELENTIS & MAKROPOULOS (1986) used focal mechanism solutions of earthquakes in the region of Gulf of Corinth to reveal the current, approximately, N-S extensional regime. AMBRASEYS & JACKSON (1990) reached the same conclusion by studying the seismicity with magnitudes $M_s \geq 5.8$ and the associated strain of central Greece between 1890 and 1988. More modern studies (BERNARD et al. 1997, RIGO et al. 1996; HATZFELD et al. 2000) were based on focal mechanism solutions of the microseismicity at the Gulf of Corinth. These studies were not only consistent with a N-S extensional strain but also showed that part of the recent microseismicity can be directly associated with several WNW-ESE faults within the study area of the present study.

The GPS-geodetical approach to the task of determining the present-day deformation at the Gulf of Corinth problem yields also an orientation of extension between N and N20°E (CLARKE et al. 1997, DAVIES et al. 1997, CLARKE et al. 1998, BRIOLE et al. 2000). Fig. 2.11 summarizes the results of 11 GPS campaigns between 1990 and 2001 after AVALLONE et al. (2004) where it is clearly shown that the extension at the Gulf of Corinth is approximately NNE-SSW orientated.

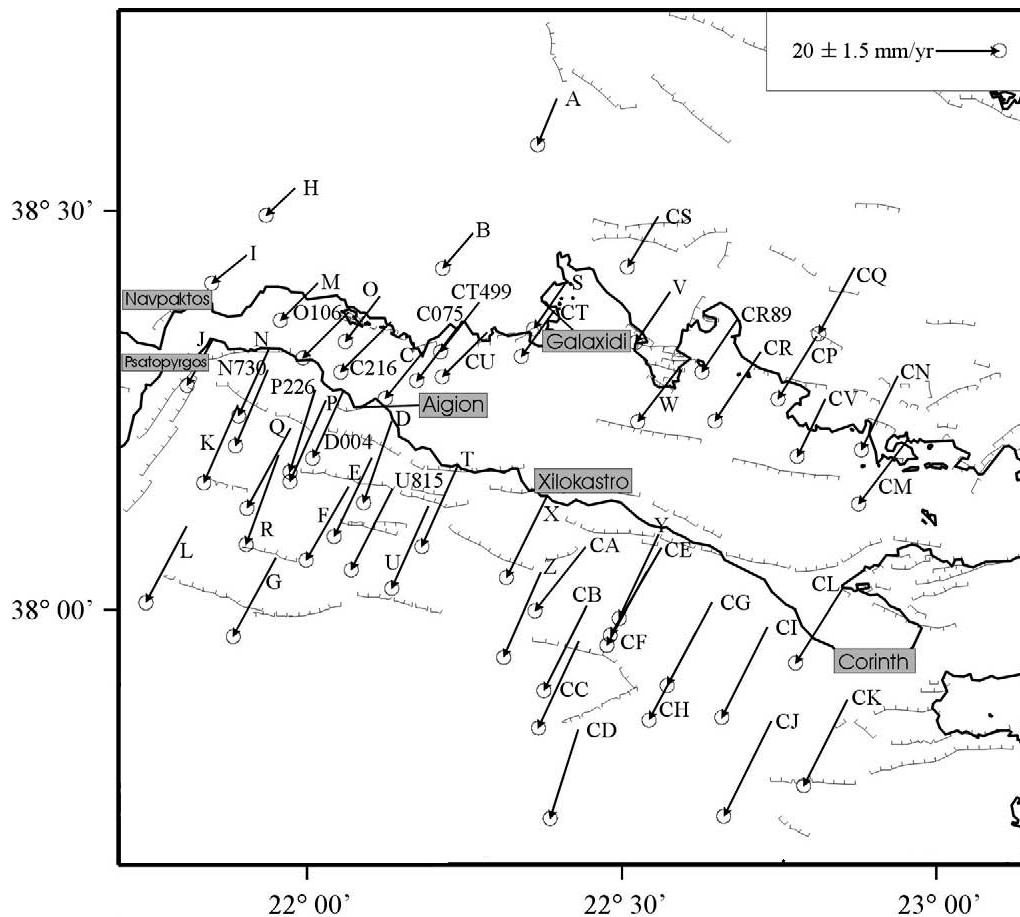


Fig. 2.11: Velocities deduced from the 11 GPS surveys carried out between 1990 and 2001 plotted in a 'fixed-Europe' reference frame AVALLONE et al. (2004). All velocity vectors are approximately SSW directed and the ones on Peloponnesus (Southern coast) are greater than the ones on the Northern coast which indicates the opening of the Gulf of Corinth.

2.3.4 Previous stress field

The satellite image interpretation also revealed the second order fault system consisting of NNW-SSE and WSW-ENE directed faults (see fig. 2.7 and fig. 2.8). This orthogonal fault system is characteristic for western Greece (DOUTSOS et al. 1987) and is associated with the post-orogenic uplift which followed the thrusting and folding of the external Hellenides after the middle Miocene (POULIMENOS et al. 1989). Taking into consideration the NNW and WSW strike direction of these normal faults another, older, stress field can be assumed with a NNW orientated σ_3 , an ENE orientated σ_2 and a vertical σ_1 . POULIMENOS et al. (1989) suggested that the σ_3 and σ_2 principal stresses which formed this system were of equal magnitude and represent extension parallel and perpendicular to the fold axes of the orogene. Furthermore the same author as well as others (ZELILIDIS et al 1988, POULIMENOS 1993, ARMIJO et al. 1996, CLARKE et al. 1998, DOUTSOS & KOKKALAS 2001) suggests that this stress regime was gradually replaced during Pliocene by the current stress regime of NNE-

SSW orientated extension as the influence of the back arc extension of the Aegean area migrated to the west (see fig 2.12).

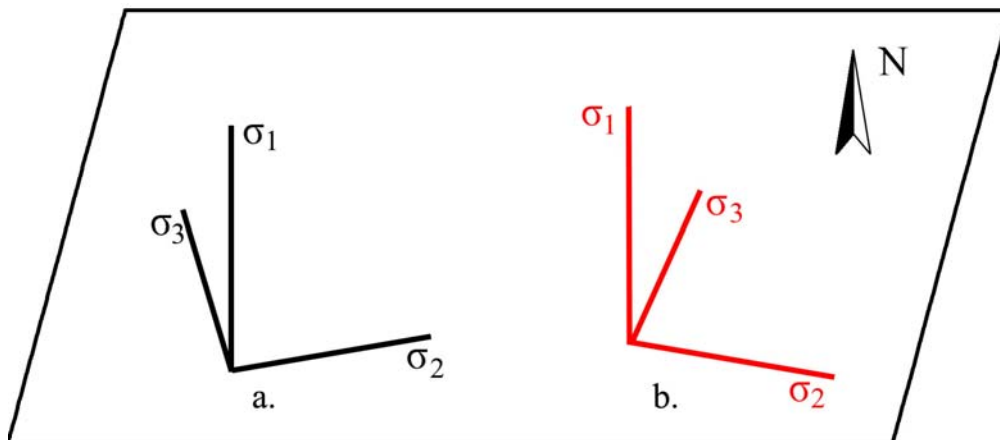


Fig. 2.12: The stress field a. is associated with the post-orogenic uplift which followed the thrusting and folding of the external Hellenides after the middle Miocene (POULIMENOS et al. 1989) and was gradually replaced during Pliocene by the current stress regime b. of NNE-SSW orientated extension as the influence of the back arc extension of the Aegean area migrated to the west causing the Gulf of Corinth to open.

The NNW-SSE and WSW-ENE directed faults of the older system continue to be active under the current NNE extension. Two facts provide evidence for that in the field: first, the faults of this system often displace recent marine terraces and second, older dip-slip lineations on the fault planes of these faults are overprinted by younger oblique ones caused by the current NNE extension (POULIMENOS et al. 1989)

3 Landslide Phenomena in the Xylokaastro area

3.1 Area of study and collected data

Along the southern coast of the Gulf of Corinth slope instabilities are very common. They consist of typical landslides, rock falls or creeping mostly within plio-pleistocenic sediments but they can also appear within outcrops of the basement rocks (cretaceous thin platy limestone of Pindos unit).

The high frequency of occurrence, the spatial distribution and the azimuthal orientation of these phenomena cannot be solely explained by the local steep morphology, the dipping direction of bedding and the relatively poor geomechanical properties of the different sedimentary formations. Very frequently, almost vertical slopes are observed which, despite the soft character of the sediments, show no evidence of instability and are only susceptible to superficial erosion (see example IV in paragraph 3.4.4). In such cases, it was observed that fault and joints were relatively absent. The question that arises is in which way and to what extent the relatively dense tectonic fabric of the area participates in controlling the occurrence of the mass movements in conjunction with other factors.

In order to study the potential relation of the landslide phenomena to the tectonic regime, an area of approximately 90Km² located SW of Xylocaastro was selected. (see fig. 1.2 and fig 3.1). In terms of relief, lithology and geomechanical properties of intact rocks, this particular area is relatively homogenous i.e. each of these factors contributes to a similar degree to the induction of landslides throughout the area. Therefore in this particular area it is possible to investigate whether the presence of faults, which are not homogeneously distributed features, plays an additionally important role in controlling the occurrence of landslides. The lithologies of the area consist mostly of plio-pleistocenic formations of lacustrine to shallow marine facies and the preneogene basement outcrops to a restricted extent as typical thin-platy cretaceous limestone of the Pindos unit. The dominating postalpine sediments can be further divided in terms of grain size into intercalating sands, silty sands and marls as well as conglomeratic layers of varying thickness. Lateral transitions between the above mentioned facies are also common. The detailed lithology is depicted in fig. 3.1. The local relief is generally characterized by deep canyons with steep slopes and typical rilly and gully forms of erosion along the NE directed drainage pattern.

The regime of the slope instability phenomena in this area was studied during a fieldwork campaign in June 2003 and previous reconnaissance fieldworks. Within the area of interest 28 cases of slope failure were discovered in the field and another 33 were located in inaccessible locations by the use of air-photographs (H.M.G.S. 1998). The landslides discovered in the field are a representing sample collected from different parts of the study area. Therefore, the total number of landslides located by fieldwork and by the use of photographs does not necessarily include all the landslides that actually exist in the study area. The width and the down-slope length of the sliding masses vary between some meters to some tenths of meters. For each landslide the strike direction of the failure plane and the direction of movement were recorded and the local geotechnical setting was evaluated. In addition, the presence of any faults in the vicinity of the in-situ observed mass movements was also recorded. The results are summarized in Table 3.1.

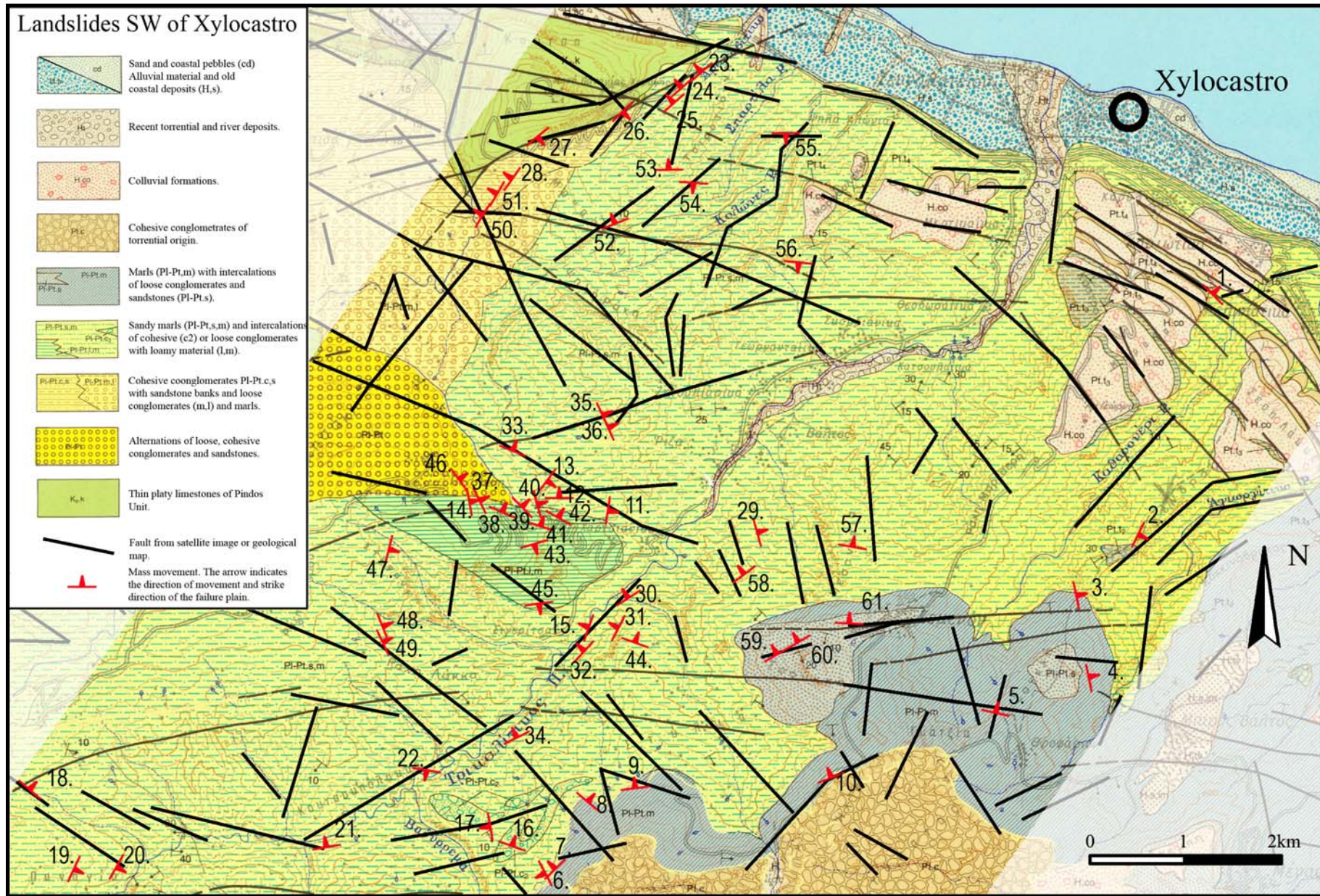


Fig. 3.1: Map showing the distribution of the landslides and the tectonic lineaments. Geology and morphology are based on I.G.M.E. (1989)

| Lanslide data collected in the field | | | | Landslide data acquired from air-photographs | | | |
|--|--|----------------------------|-------------------------------------|--|--|----------------------------|-------------------------------------|
| n | Mean strike direction of failure plane | Direction of mass movement | Relation to present fault in map L1 | n | Mean strike direction of failure plane | Direction of mass movement | Relation to present fault in map L1 |
| 1 | 135 | NE | A | 29 | 164 | ENE | NF |
| 2 | 26 | ESE | B | 30 | 57 | NNW | A |
| 3 | 168 | ENE | NF | 31 | 28 | WNW | NF |
| 4 | 168 | ENE | NF | 32 | 43 | NW | A |
| 5 | 102 | NNE | A | 33 | 112 | NNE | A |
| 6 | 152 | WSW | NF | 34 | 64 | NNW | NF |
| 7 | 45 | NW | NF | 35 | 156 | ENE | B |
| 8 | 130 | NE | NF | 36 | 156 | ENE | B |
| 9 | 84 | N | B | 37 | 154 | ENE | NF |
| 10 | 68 | NNW | A | 38 | 114 | NNE | NF |
| 11 | 10 | E | A | 39 | 135 | NE | NF |
| 12 | 90 | N | A | 40 | 164 | ENE | NF |
| 13 | 36 | SE | NF | 41 | 108 | NNE | NF |
| 14 | 170 | E | NF | 42 | 120 | NNE | NF |
| 15 | 20 | WNW | B | 43 | 73 | SSE | NF |
| 16 | 110 | NNE | NF | 44 | 110 | NNE | NF |
| 17 | 170 | W | B | 45 | 82 | S | B |
| 18 | 132 | NE | A | 46 | 144 | NE | NF |
| 19 | 25 | ESE | NF | 47 | 14 | ESE | NF |
| 20 | 30 | ESE | B | 48 | 158 | ENE | NF |
| 21 | 80 | N | B | 49 | 154 | ENE | B |
| 22 | 100 | S | B | 50 | 32 | WNW | B |
| 23 | 38 | NW | A | 51 | 30 | WNW | NF |
| 24 | 38 | NW | A | 52 | 68 | NNW | A |
| 25 | 38 | NW | A | 53 | 88 | N | B |
| 26 | 45 | SE | A | 54 | 95 | S | B |
| 27 | 51 | SE | B | 55 | 89 | S | A |
| 28 | 35 | NW | NF | 56 | 95 | S | B |
| A= the landslide has similar strike direction to that of the present fault B= the landslide has irrelevant strike direction to that of the present fault NF= No fault is present | | | | 57 | 100 | N | NF |
| | | | | 58 | 53 | NW | B |
| | | | | 59 | 60 | NNW | A |
| | | | | 60 | 60 | NNW | A |
| | | | | 61 | 92 | N | A |

Table 3.1.: Strike direction and direction of movement of the observed landslides (field investigation and air-photographs) and the type of their relation to the faults of fig.3.1.

3.2 The orientation and location of landslides in comparison with the local tectonic fabric

3.2.1 Correlation of azimuthal distributions

The azimuthal distribution of strike directions of the failure planes is depicted in the rose-diagram of fig. 3.2a. The dataset comprises the data collected in the field and from the evaluation of air-photographs.

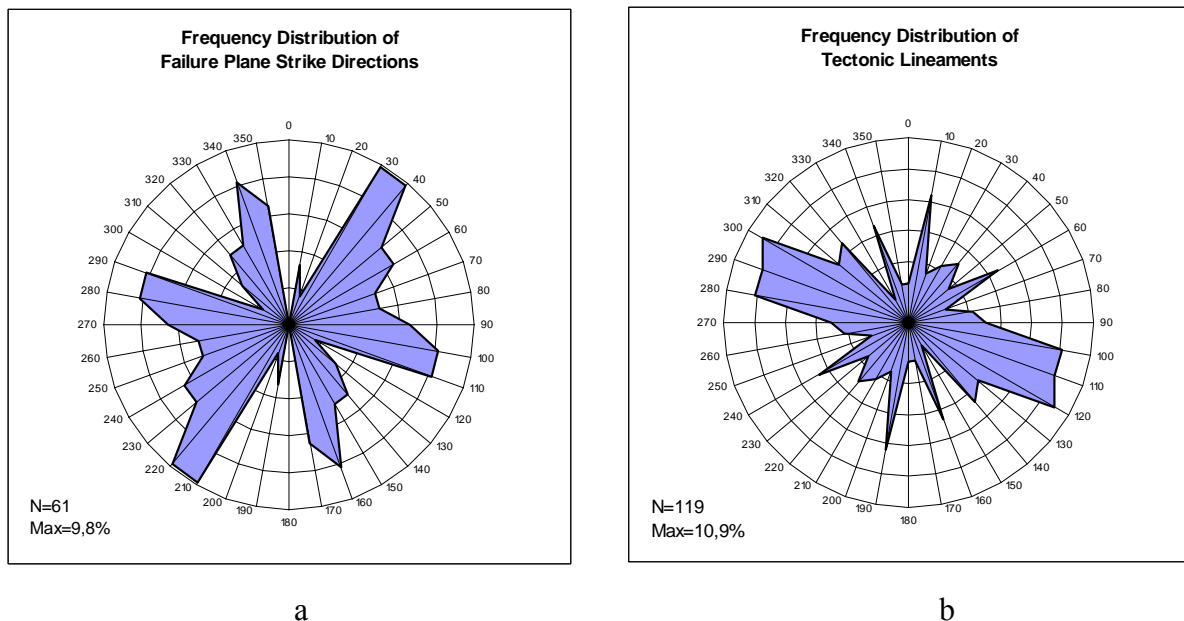


Fig. 3.2: Rose-diagrams of the azimuthal distribution of failure plane strike directions (a) and tectonic lineaments (b) in the study area.

The local tectonic fabric is presented in rose diagram b of fig. 3.2, the data derive from the lineament analysis of the corresponding LANDSAT TM5 bands 4, 5 and PC1 (First Primary Component) satellite images after the application of image enhancement processes (see chapter 2). By comparing the two rose diagrams of fig. 3.2 it is obvious that the frequency maxima of the failure plane strike directions coincide to a great degree with the frequency maxima of the tectonic lineaments. More precisely, three azimuthal maxima of failure planes can be distinguished:

a. A landslide system with $N90^{\circ}$ - 110° failure plane strike directions (in rose-diagram a of fig. 3.2) coinciding with the WNW-ESE orientated and most dominant fault system in the area of investigation and overall in the Gulf of Corinth area (rosediagram b of fig. 3.2).

b. A system of N310°-350° striking failure planes (in rose-diagram a of fig. 3.2). This can be correlated with the NNW-SSE orientated fault system in rose-diagram b of fig. 3.2 which has, however, a comparatively restricted presence.

c. A group of N30°-60° striking failure planes (in rose-diagram a of fig 3.2). This is the most prominent one and corresponds with the relatively subordinate and dispersed fault distribution with strike directions between NNE and ENE in rose-diagram b of fig 3.2).

3.2.2 Correlation of spatial distributions

Apart from the azimuthal conformity between the population of sliding planes and the local tectonic fabric there is evidence that also the locations of the mass movements are substantially related to the location of the faults. During the fieldwork campaigns it was observed that many of the visited landslides were in the vicinity of tectonic faults. Some of them were not only located on faults but also had failure planes with a geometry similar to the geometry of these faults. In general, the present faults or fault zones provide weak areas in the rocks which can consequently function as slope failure planes. Such an influence can also be observed in map scale by plotting the positions of the landslides and the tectonic faults. The result is shown in fig. 3.1 where the fault lineaments in derive from the lineament interpretation of LANDSAT TM5 images (see chapter 2) and the landslide locations comprise the in-situ observed cases and the ones detected by the use of air-photographs. In fig. 3.1, 29.5% of the mass movements have failure planes with a strike direction similar to that of their immediately neighbouring faults ($\pm 15^\circ$ difference in strike direction and distance less than 100m from the fault) and more than 50% are practically located near or on fault zones irrespectively of strike direction (distance less than 100m distance from fault).

3.2.3 Interpretation of the azimuthal and spatial conformity between mass movements and faults

In the study area, the existence of weak zones provided by faults induces in general a significant spatial coincidence of the mass movements with these faults. Here, it is possible to distinguish between the landslides that spatially coincide with faults and have failure planes of the similar strike and direction with these faults and landslides that spatially coincide with faults and have failure planes with a strike direction irrelevant to that of the faults. In the first case, the slope and the fault plane geometry are similar and the slope failure takes place within a part of a fault plane (see example I in paragraph 3.4.1). In the second case, the rock is

also weakened by the fault activity and is therefore prone to landslides. The slope geometry, however, might not allow sliding within the fault plane or planes and the failure plane is formed within secondary joints or fissures or disaggregated zones (see example III in paragraph 3.4.3). Alternatively, at the flanks of the sliding mass, the movement might take place within fault planes which strike sub-parallel to the slide direction. These mechanisms explain the occurrence of several landslides, with a strike direction of failure planes which is irrelevant or perpendicular to the local fault planes (e.g. landslides num. 17,20,35,45 in fig.3.1).

It is evident from the above correlations, that the azimuthal conformity between the strike directions of the failure planes and the fault groups is directly induced in the cases where a part of a fault plane functions as a failure plane within a slope.

In addition, the tectonic fabric in the study area controls the geometry of the drainage network resulting into streams parallel to the fault directions (POULIMENOS et al. 1989, SEGER & ALEXANDER 1993, COLLIER et al. 1995). Hence, the slopes have a similar orientation to that of the faults and, as a result, the failure planes of the landslides taking place on these slopes have a strike direction indirectly imposed by the faults. Consequently, the azimuthal conformity between the tectonic fabric and the majority of the landslides is also indirectly induced, irrespectively of the number of faults (rose-diagram b of fig. 3.2). This may be an explanation why all three groups of failure planes in rose-diagram a of fig. 3.2 have populations of the same order whereas the corresponding fault systems do not. Furthermore, since the main axis of the drainage system is NE directed, the counterpart group of landslides (with approx. NE-SW strike direction) is the one with the greatest population (in rose-diagram a of fig. 3.2).

The azimuthal and spatial conformity between landslides and fault systems is a not an exclusive feature of the study area. On the contrary, it is characteristic for the southern coast of the Gulf of Corinth. ROZOS (1991) has observed the same dependence of the landslide distribution on the distribution of faults in the coastal region extending to the west of the present study area. Nevertheless, the area examined by ROZOS (1991) consists of rocks with varying geomechanical behaviour such a massif and weathered limestone, hard conglomerates as well as soft fine grained sediments and therefore the spatial distribution of the landslides in his area might be more lithology-dependend.

3.3 Mass movement mechanisms and triggering factors

3.3.1 Differentiation of factors favouring landslides

As explained above, the spatial distribution of landslides is controlled by tectonics in a direct way in cases where a fault provides weak zones which can function as failure planes. This applies for at least 30% of the mass movements in the area. The landslides that occur away from faults and fault zones imply that there are other factors, independent from fault presence, that also control the occurrence of mass movements.

A mass movement takes place when several factors act simultaneously. Here, it is possible to differentiate between the factors that generally create unstable geotechnical conditions and those that are responsible for initiating the slope movement phenomena (triggering). Taking this differentiation into consideration and by investigating the mechanisms that lead to slope movements in the area of study it was possible to identify the following landslide inducing factors:

3.3.2 Factors that create unstable conditions prone to accommodate mass movements

The following factors have a protogenic i.e permanent or intrinsic character and can be observed throughout the study area. They were characterized as protogenic because they don't function as triggering factors but they define the areas with deficient slope stability.

-Lithologies

The geological formations in the area consist mostly of fine grained sediments (sand, silt) and conglomerates of varying cementation degree. In general, it can be stated that in the study area the geomechanical properties of these plio-pleistocenic sediment formations are frequently deficient. Also, the interaction between soft and hard, more and less permeable layers consisting these sediments plays a particular role in inducing stability problems. The thin platy limestone of the Pindos unit is outcropping only at the NE corner of the study area. These rocks have principally better geomechanical properties than the plio-pleistocenic formations. However, the intense folding of the Pindos unit during the orogenesis in combination with the thin platy character can also provide conditions of severe slope instability.

-Faults and fault zones

As already described, faults and fault zones degrade the geomechanical properties within the rocks in the study area and thus provide zones where mass movements are favoured. Tectonic discontinuities also provide zones within the rock where an increased water infiltration is possible with further consequences on the saturation degree of the sediment pores. Here, the role of the faults can be described as passive as they only delineate areas of aggravated conditions. The potential dynamic behaviour of faults is considered a triggering factor and will be examined further below.

-Slope inclination

The study area is as under constant tectonic uplift, which results to deep incised valleys with steep slopes. The slope morphology is, therefore, under constant development and not in static equilibrium.

3.3.3 Factors that initiate the mass movement phenomena (triggering factors)

-Presence of water

According to the field observations the most frequent factor that triggers mass movement phenomena in the study area is rainfall. The same conclusion was reached by KOUKIS et al. (1996a) who correlated landslide and precipitation data of 40 years from the Achaia County which is located immediately to the west of the present study area and has a similar geological setting. Furthermore, the same author (KOUKIS et al. 1996b) recognised that rainfall is in general a predominant landslide triggering factor in Greece. In general, surface water induces erosion which acts in favour of landslides especially in cases where erosion of torrential character undercuts steep slopes STOURNARAS (1998). Of greater importance is the increase of water content and pore pressure fluctuations which reduce the shear strength of the pleistocene formations. This effect is decisive especially within the weaker zones of potential sliding planes such as fault planes, fractures or joints. Moreover, these discontinuities have usually a higher permeability than the surrounding intact rock which results to an additional aggravation. Besides, the water conducted through such discontinuities can accumulate in bedding or discordance surfaces especially between conglomeratic caps and underlying, relatively impervious, finer grained sediments. It has to be underlined that the course of annual precipitation in the study area is opposite to that of the temperature and therefore when the winter rain comes the water can percolate rapidly through desiccation cracks and the loose dry soil. The annual precipitation is about 600-900mm/year and it is concentrated in winter

(approximately 100-150mm/month) whereas during summer the rainfall is very low (KARAPIPERIS 1974, ROZOS 1991). This implies a substantial fluctuation of water content within the plio-pleistocenic formations from summer to winter and vice versa.

-Geodynamic factors

Earthquakes are considered as one of the most frequent landslide triggering factors in Greece (KOUKIS & ZIOURKAS 1991). The Gulf of Corinth region is characterized by a profound seismicity with 10 earthquakes of $M_s \geq 6.0$ within the last 30 years and numerous weaker earthquakes (e.g. TSELENTIS & MAKROPOULOS 1986, HATZFELD et al. 2000, SACHPAZI et al. 2003). Hence, the intense seismicity of the Gulf of Corinth is a substantial landslide triggering factor in the area of study and in the Gulf of Corinth region in general.

Apparently there are threshold magnitudes below which seismic events rarely cause landslides. Above these thresholds other parameters such as the distance from the epicentre or the fault rupture and the local ground motion characteristics determine whether a critical slope will slide (KEEFER 1984).

According to HARP & JIBSON (1995), the behaviour of potential failure planes or zones can be affected during earthquakes by the following mechanisms:

- Alteration of the shear strength depending on the acting forces during the earthquake.
- Dynamic response of pore pressure with further consequences on the shear strength
- Acceleration and especially vertical acceleration acting in addition to gravity.

Apart from the earthquakes, which have a regional influence, displacements and deformation along faults on the surface can also activate unstable slopes directly. Beside earthquake related fault displacement, aseismic fault slip can also act to a certain degree as a triggering factor. More specifically, it has been observed that a fault might continue to slip post-seismically for a long period and this displacement may be equal to the co-seismic displacement (KOUKOUVELAS & DOUTSOS 1996). Furthermore, the monitoring of active faults in the area, which is presented later in this study, has shown that faults can demonstrate aseismic creeping during interseismic periods. These types of fault behaviour can be considered as dynamic factors with landslide triggering effects in contrast to the aforementioned passive effects (paragraph 3.3.2).

-Artificial (anthropogenic) factors

Apart from the natural processes outlined above, human intervention can also contribute in triggering landslides. The most common ways in which human activity can trigger landslides in the area of study are:

-Steepening or increasing the height of the slope for the needs of roads, agriculture, constructions etc.

This human activity is the most frequent landslide inducing factor in the study area. It is usually combined with decreasing the load and support at the base of the slope and/or overloading of the top side. The road network of the area is of a low significance and therefore the planning and construction are usually mediocre.

-Deforestation and reduction of low vegetation.

The number of occurring landslides in the study area increased locally after a fire at the end of the 90s. The destruction of trees and low vegetation in this way increases the rate of erosion and disturbs the water infiltration rates with consequences on the stability of the slopes (see example II in paragraph 3.4.2).

-Cultivation and irrigation.

In the study area, several cultivated areas are on terraces delimited by steep slopes. An intense irrigation of these cultivated areas can influence the slope stability by locally increasing the water content in the rocks. However this is a relatively occasional case with minor significance in the study area.

-Artificially induced vibration and load due to heavy traffic.

This factor is the least expected in the study area because the road network is secondary and therefore not normally used by heavy traffic. Nevertheless, considering the critical condition of many slopes along the roads in the study area, it is apparent that occasional heavy traffic on these roads can potentially increase the risk of a landslide.

3.4 Slope examples

3.4.1 Example I

A typical example of the influence of faults on slope stability is shown in fig.3.3. The slope dips to the North and consists of light grey to yellow sandy marls and overlying conglomeratic blocks. On the site, it was observed that the road disrupted by the landslide was deformed and fractured which means that the instability also extended below it. The bedding of the sandy marls has a dip direction of 164/30 i.e. in the opposite direction to the dip direction of the slope.

Obviously the bedding planes cannot function as sliding surfaces. The slope failure took place within tectonic fractures with a dip direction of 354/66 and displacements of ca. 10 cm (fig 3.4). The landslide was triggered by rainfall probably in combination with the instability induced by the road cut. However, the protogenic factor which determined the location and the geometry of the failure plane was the fault zone.



Fig. 3.3: A slope failure within sandy marls disrupting a road and triggered by rainfall. Deformation on the road surface implies that the instability extends also below the road i.e. the entire slope is moving.



Fig. 3.4: The landslide has revealed a group of parallel minor faults, dipping in the same direction as the slope, which comprised the failure plane.

3.4.2 Example II

The second example (fig. 3.5) concerns the extensive mass movements taking place on a slope where no faults seemed to be present. As a result of the slope movements, the road in fig. 3.5 had to be abandoned. The slope consists of loose conglomerates with a loamy matrix i.e. a material with poor geomechanical properties. However, the instability initiated after deforestation (due to a fire) which allowed the precipitating water to aggravate the conditions. Before the deforestation the slope supporting measures seen in fig. 3.5 were sufficient and the road was usable for about 30 years and, which implies that any slope movements during this period were of a restricted extent. The area affected by the fire exhibits an increased number of landslides which appear as cluster immediately west of the centre of the study area (see fig. 3.1).



Fig. 3.5: Extensive mass movements in sandy marls and intercalating loose conglomerates with loamy matrix after deforestation (fire) which allowed slope instability to initiate in areas where slope supporting measures were formerly not necessary.

3.4.3 Example III

As previously described there are cases of landslides occurring on slopes disturbed by faults where the failure plane of the landslide is not coinciding with any of the fault planes. In such cases the slope is unstable because the rocks are in general disaggregated by the local tectonic activity and therefore have a reduced shear strength in comparison to the intact rocks. Such an example is the artificial slope of fig. 3.6. The occurred mass movement has a failure plane striking at approximately $N170^\circ$ whereas the present fault planes within the slope strike at $N70^\circ$ and dip with 78° towards NNW i.e. the strike direction of the failure plane and the fault planes are almost perpendicular to each other. The mass movement was probably triggered by rainfall during winter. Away from the outcropping fault planes the slope is stable despite the relatively steep inclination.



Fig. 3.6: Slope failure within marly sands at a location where the slope is cut and disturbed by fault planes (the revealed fault traces are shown by dashed lines). The geometry of the fault planes and the failure plane are irrelevant to each other.

3.4.4 Example IV

In the study area, apart from instable slopes, within the same sediment formations there were also ones that demonstrated remarkable stability despite extreme inclinations (80-90°). Irrespectively of bedding geometry such slopes (e.g. in fig. 3.7) were susceptible only to surface weathering and erosion. After investigating such cases it was ascertained that these slopes were not disturbed by any significant faults or fault zones. This emphasizes once again the primary role that faults can play concerning the manifestation of the mass movements in the area.



Fig. 3.7: Approximately vertical, 40m high slope with no signs of instability. The sediments are sandy marls.

3.5 Finite-Element modelling of the influence of faults on the slope stability

As seen in the previous examples the presence of a fault plane can be a decisive factor concerning the stability of a slope. The case of example IV is particular interesting because it shows that, despite the relatively poor geomechanical properties of the plio-pleistocenic sediments, very steep slopes can also remain stable if they are not disturbed by faults. By means of finite element modelling it was attempted to investigate the stability of the slope in example IV and to depict how faults act in favour of the formation of slope failure planes in the study area.

An FE-model of the slope in example IV was constructed and analysed by the use of the GTE, GTF and GTG programs (STROMEYER 2001) (figures 3.8 to 3.11). The FE-model of the slope in fig. 3.8 has a height of 35m, an inclination of 80° at its upper part and 50° at its lower part.

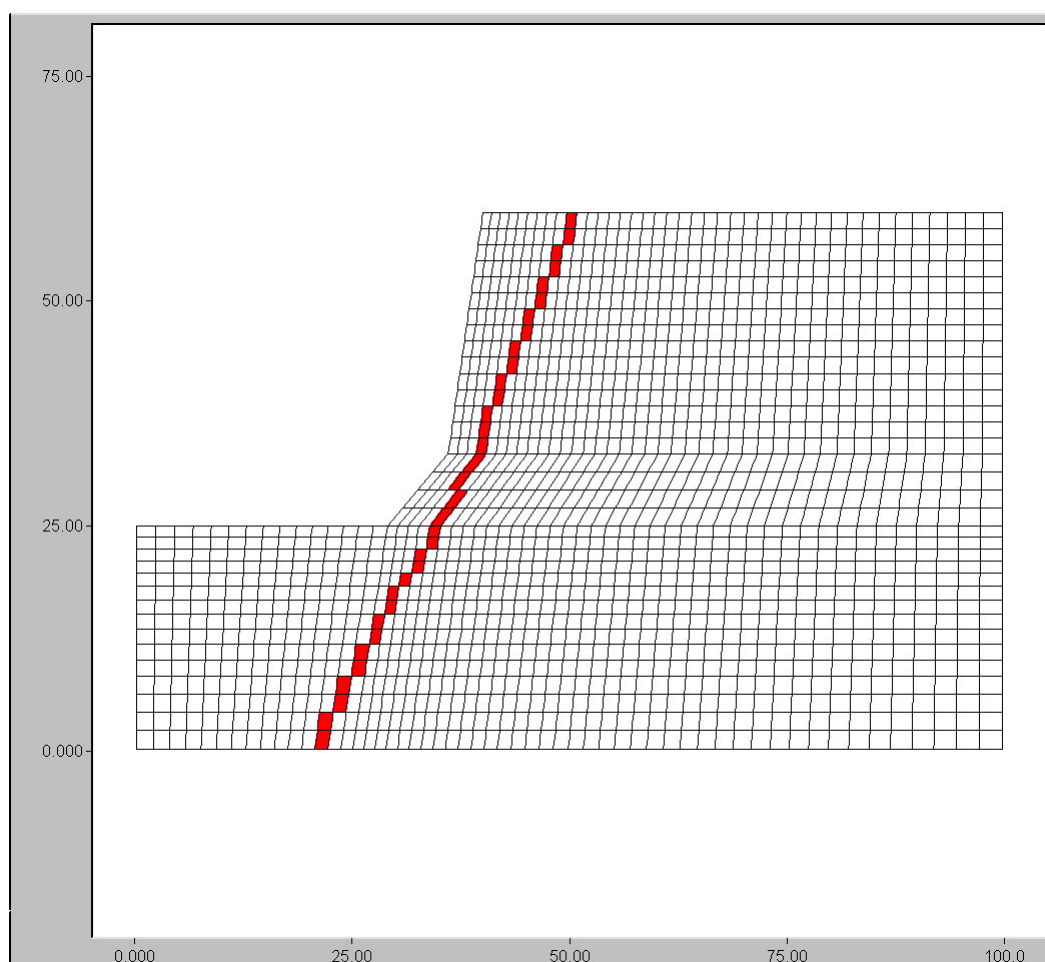


Fig. 3.8: The Finite Element model used for the simulation of the slope of example IV. The slope has a height of 35m, an inclination of 80° at its upper part and 50° at its lower part similar to the dimensions of the real slope. The red cells represent the area where the fault zone is located (dip-angle 65°). The geomechanical properties of the model are described in Table 3.2.

Three different cases were modelled, through which the mechanical properties of the intact rock remained the same:

- a. The slope is in an intact condition i.e. no fault is present.
- b. A fault zone is added to the model with a dip angle of 65° and a width of approximately 2m (see fig. 3.8).
- c. The cohesion of the same fault zone is lower while all other geomechanical properties and the geometry of the fault zone and surrounding rock remains the same.

The geomechanical properties which were assigned to the model-cases are given in Table 3.2

Table 3.2

| Geomechanical properties assigned to the FE-models | | | | | |
|--|---------------------------|------------------------------|---|--------------------------|------------------------------|
| | E modulus (E) (MPa) | Poisson's ratio (ν) | Density (γ) (kg/m ³) | Cohesion (c) (MPa) | Friction angle (ϕ) |
| Intact rock (cases a,b,c) | 1000 | 0.25 | 2300 | 0.180 | 35° |
| Fault zone (case b) | 900 | 0.35 | 2300 | 0.090 | 35° |
| Fault zone (case c) | 900 | 0.35 | 2300 | 0.040 | 35° |

The FE-model of fig. 3.9 depicts a slope which is not disturbed by a fault. The areas in this slope with high stress levels have a relatively insignificant extent and are located at the surface of the slope. In the rest of the slope no zones of plastic deformation are present i.e. no critical failure planes are formed.

In figures 3.10 and 3.11 the same slope geometry is modelled but now a fault plane is present within the slope. Fig. 3.10 describes the calculated stress levels within the model case b where the fault zone is present with a cohesion of 0.090MPa. Here, there are areas along the fault

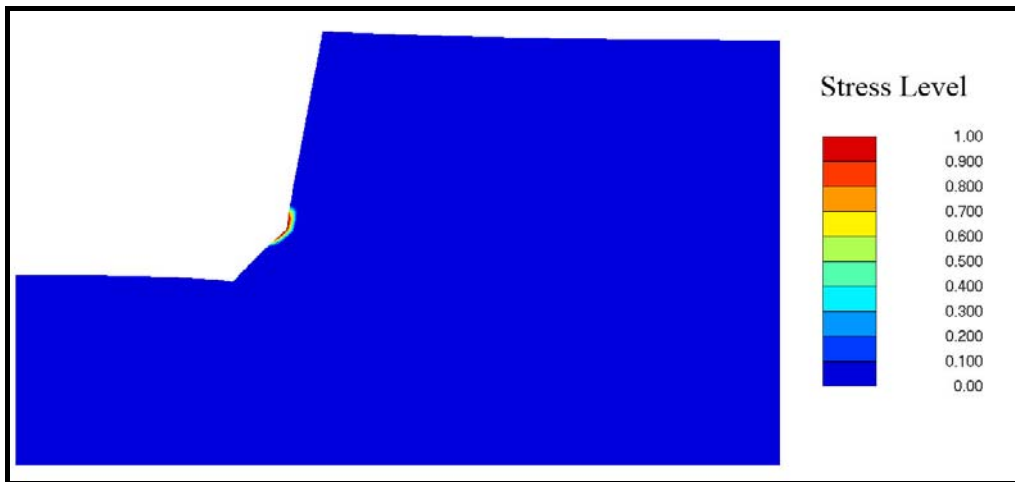


Fig. 3.9: Model case a. No fault is present. The disturbed zone is superficial and has a restricted extent. The entire model has the following geomechanical properties: $E=1000\text{MPa}$, $\nu=0.25$, $\gamma=2300\text{Kg/m}^3$, $c=0.180\text{MPa}$ and $\phi=35^\circ$.

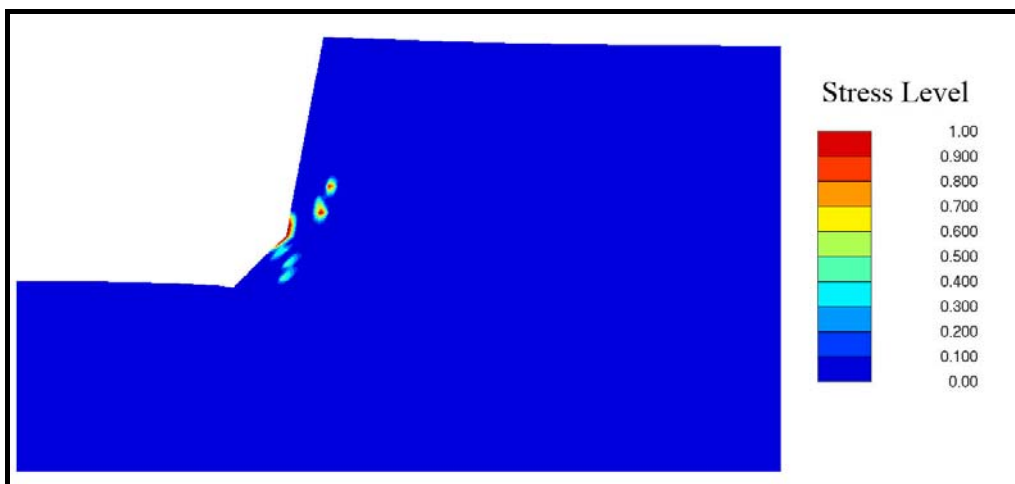


Fig. 3.10: Model case b. The presence of the fault is inducing areas of shear failure within the slope. The geomechanical properties within the fault zone are: $E=900\text{MPa}$, $\nu=0.35$, $\gamma=2300\text{Kg/m}^3$, $c=0.090\text{MPa}$ and $\phi=35^\circ$.

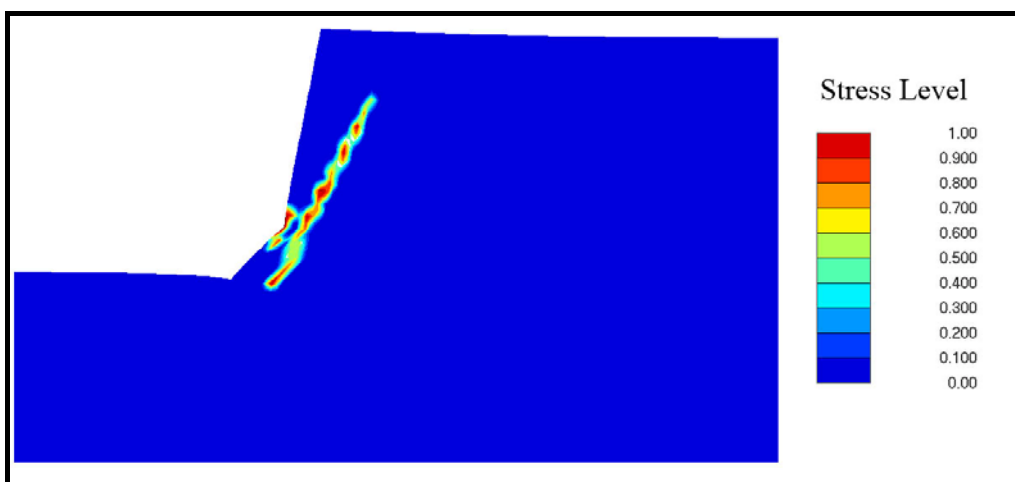


Fig. 3.11: Model case c. Now the fault zone is assigned a cohesion of 0.040MPa while all are properties remain the same. The zone of plastic strain is greater; it deviates from the trace of the fault and reaches the surface of the slope i.e. a potential failure plane is formed.

zone characterised by high stress levels. This implies that shear failure is possible. If the fault zone is assigned a lower cohesion of 0.040MPa like in model-case c (fig. 3.11) then the zone of plastic strain is longer. Most important is the fact that a part of the zone of potential shear failure deviates from the trace of the fault and reaches the surface of the slope. In other words a failure plane is formed along which sliding can take place.

Apparently, in addition to the mechanical reduction of the cohesion of the rocks due to faulting, the reduction of the friction angle e.g. by the presence of water pore-pressure will have the same effect. Moreover the inclination of the fault zone and its distance from the slope has also an effect on the geometry of the favoured failure planes.

3.6 Summary and Conclusions

An area of approximately 90km² was investigated SSW of Xylocastro (fig 3.1) on the southern coast of Gulf of Corinth where slope instability phenomena are very frequent. A total of 61 landslides were located by means of fieldwork and air-photograph evaluation. The distribution of the landslides is imposed to a great degree by the distribution of the tectonic fabric. The occurrence of ca. 50% of these landslides was found to be related with the presence of faults and 30% had failure planes with strike directions similar to that of the present faults. The increased frequency of mass movements within the area is owing to a combination of steep morphology, poor physical properties of the prevailing fine grained sediments and the dense and active tectonic elements of the area. These are, however, primary factors inducing slope stability deficiencies and most of the times the mechanism of mass movements are initiated by additional processes such as water (precipitation) and anthropogenic influence. The intense seismicity of the region is undoubtedly a significant landslide triggering factor. Nevertheless, it is difficult to ascertain the extent to which earthquakes induce slope movements because only long-term observations would allow a representative correlation between the earthquake parameters (e.g. magnitude, epicentral distance and local ground motion characteristics) and their impact on slope stability. Concerning the effect of potential co-seismic or aseismic fault displacements, which are certainly anticipated in the area, a similar long-term approach is necessary. Here, a parallel displacement monitoring of the faults and the corresponding instable slopes could reveal in a quantitative way the dependence of landslides on fault movements. The aforementioned type of survey could verify whether the clustering of landslides along specific fault zones is a direct indication that these are tectonically active.

4 Active fault monitoring at the Perachora peninsula (eastern termination of Gulf of Corinth)

4.1 Instrumentation

4.1.1 Introduction

Monitoring fault displacements on the earth's surface is a very demanding task. Reliable results can be obtained only after long terms of monitoring. Exogenous factors such as temperature and precipitation can affect the measurements to a certain degree. Typically, the prerequisites for a fault monitoring device are high sensitivity, simplicity, long-term stability and reliability in an out-door environment. Simultaneously the influence of error-inducing factors, such as temperature fluctuations on the monitoring devices, should be as minimal as possible and well defined.

Taking into consideration the above mentioned factors, two types of instruments were selected to be installed on active faults of the Perachora peninsula. One type of instrument is the so called Crack Gauge TM71 which is up to date one of the most competent devices for this purpose. The second type of instrument is an extensometer based on optic fibre sensors called Bragg Grating Extensometer.

Both instrument types, despite the different measuring principles, have the form of an elongated bridge in the middle of which the recording sensor is situated. The aim was to measure the relative displacements between the hanging wall and footwall of faults by installing these instruments perpendicularly between them.

4.1.2 The Crack Gauge TM 71 device

4.1.2.1 Description and principle of function

The TM71 Crack Gauge is a simple and robust instrument based on the mechanical-optical interference known as the Moiré effect and has been designed by the Institute of Geology and Geotechnics of the Czech Academy of Sciences in Prague (KOSTAK 1969 and KOSTAK 1991). This device is designed to monitor displacements over a long time in all three spatial components at sub-millimetre scale. Such instruments have already been used for fault monitoring in Bulgaria (KOSTAK & AVRAMOVA-TACEVA 1988), Germany (FECKER et al. 1999, RYBAR et. al. 2001), Peru and Italy (STEMBERK et al., 2003) as well as crack gauges on constructions such as bridges (KOSTAK 1991), for slope-stability investigations and for crack and joint monitoring (KOSTAK & CRUDEN 1990, KOSTAK et al. 1998).

The TM71 is capable of recording displacements by producing interference patterns on optical grids (KOSTAK 1991). It mainly consists of two identical indicators (fig 4.1). Each indicator consists of two superimposed glass plates. On each glass plate and with high density an identical circular grid of equidistant circles and an identical linear grid consisting of equidistant parallel lines have been etched. (fig. 4.1).

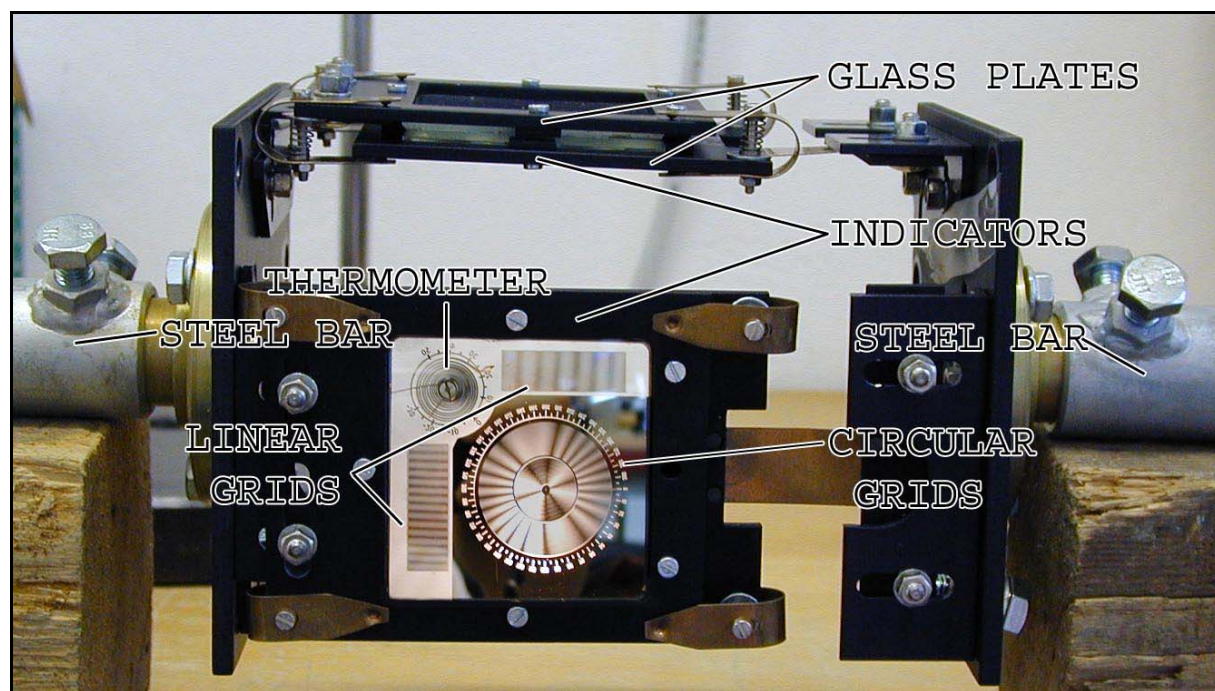


Fig. 4.1: Overview of the main parts of a TM71 device same as the ones used in the present study.

The superposition of the glass plates of each indicator forces light to produce Moiré interference patterns through the superimposed circular and linear grids in the form of black and white fringes. These patterns are very sensitive to relevant displacements and are unequivocal for each vector of eccentricity of the grids. Each of the two glass plates comprising one indicator is fixed on either side of the instrument. By means of cemented steel bars (see fig.4.1), each side of the instrument can be firmly connected to the rock on one side of the fault. Hence, any relative movement of the opposite sides of the fault will result in a relative displacement of the glass plates and therefore a respective Moiré pattern will be formed as described above. The pattern characteristics can be obtained visually or recorded photographically or by any other video technique.

The Moiré phenomena in the circular grid of each indicator provide with 2-dimensional displacement measurements. The indicators are perpendicular to each other; hence 3-dimensional results can be recorded. The linear grids can be used to measure the rotation

about the axis which is perpendicular the plane of each indicator. The measurement of rotations was not useful for the purposes of the present study and was not utilised. A description of the methodology for rotation measurements can be found in appendix §2.

It is obvious that, being a purely mechanical/optical device, the TM71 eliminates any sources of error that are potentially induced when using electronic instruments, for example errors induced through the conversion of mechanical signals to electronic.

4.1.2.2 Methodology of use

-Interpretation of the Moiré patterns

The interference patterns produced by the circular grids consist of a number of symmetrically arranged fringes stretching radially from the centre (fig. 4.2). The number N of the fringes on one side of the symmetry axis provides the length of the displacement vector while the orientation of the symmetry axis (angle a) provides its direction (fig. 4.2). The proper value of the angle a in gons is read on the side of scale where the scale marks can be seen connected.

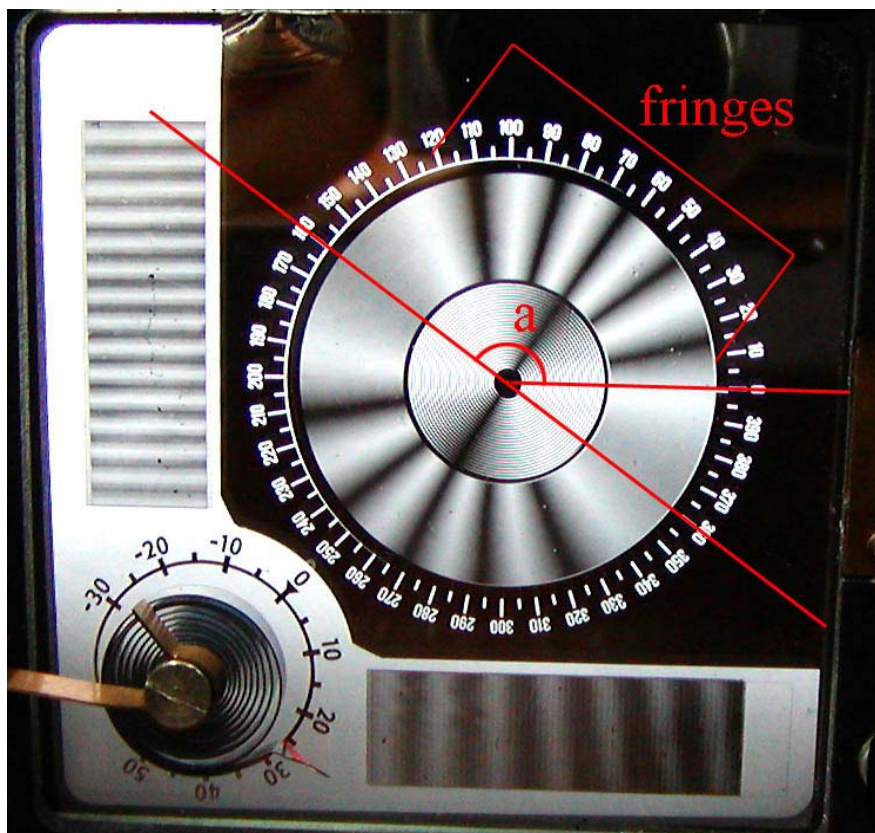


Fig. 4.2: Detailed view of the Moiré patterns formed on the circular grid of a TM71 Moiré indicator and their features.

The displacements along the x and y co-ordinate axes (measured by one indicator) can be calculated by the following formulas (KOSTAK 2001):

$$x_{xy} = 1/2 c N_{xy} \cos a_{xy} \quad (1)$$

$$y_{xy} = 1/2 c N_{xy} \sin a_{xy} \quad (2)$$

where x_{xy} is the component of displacement along the x axis.

y_{xy} is the component of displacement along the y axis.

c is a constant of 0.05mm related to the grid density

N_{xy} is the number of the fringes on one side of the symmetry axis of the pattern

a_{xy} is the angle of orientation of the symmetry axis of the pattern.

Accordingly, the second indicator provides measurements along the x co-ordinate axis again and along the z co-ordinate axis:

$$x_{xz} = 1/2 c N_{xz} \cos a_{xz} \quad (3)$$

$$z_{xz} = 1/2 c N_{xz} \sin a_{xz} \quad (4)$$

where x_{xz} is the component of displacement along the x axis.

z_{xz} is the component of displacement along the y axis.

c is a constant of 0.05mm related to the grid density

N_{xz} is the number of the fringes on one side of the symmetry axis of the pattern

a_{xz} is the angle of orientation of the symmetry axis of the pattern

Obviously the displacement along the x axis is measured by both indicators and therefore the average of the two values (x_{xy} and x_{xz}) is the value that is taken into account.

The sensitivity of the instrument is 0.05-0.0125mm in all three space co-ordinates (STEMBERK 2003) and the accuracy of field measurements is generally 0.03 mm (STEMBERK 2003).

-Temperature compensation

In case of temperature fluctuations a correction should be considered. The correction concerns dilatation of the instrument bridge whereas the temperature effects in rock are considered intrinsic (KOSTAK 2002). Therefore the temperature to be measured concerns the bridge itself and is provided by a bimetal spiral thermometer attached on one of the indicators (fig.4.1). The temperature compensation is calculated as:

$$\Delta A_t = \varepsilon \Delta t l_A \quad (5)$$

where: ΔA_t is the displacement correction

ε is the dilatation coefficient of the instrument bridge, including the instrument itself, and is equal to $12 \cdot 10^{-6}$

Δt is the difference of temperature of the bridge from the previous reset of the instrument to zero

l_A is the length of the bridge including the instrument itself.

The correction ΔA_t will compensate the temperature influence on the displacement value as follows:

$$A_n = A_{nt} - \Delta A_t \quad (6)$$

where: A_n is the corrected displacement value

A_{nt} is the displacement value at a temperature t

ΔA_t is the displacement correction

A temperature compensation is to be calculated individually for each coordinate x, y, z by using the respective distance l_A in the formula (3). This is the distance between the points where the instrument bridge is attached to the rock, measured parallel with the respective axis. Despite the well defined temperature compensation it is advisable to reduce the temperature effects as much as possible. If, the instrument bridge between the fault walls is of a linear form, which is mostly the case, then obviously for the axes y and x the distance l_A is equal to zero and therefore only the correction of the z component is necessary (KOSTAK 2002). The temperature effects on the instrument can be further reduced by selecting installation locations which require the shortest possible fixation bars.

-Important Conventions

For the evaluation of the calculated values, the following conventions concerning the movable object and the direction of movement are important. As unmovable, is considered the object (i.e. fault side) which is on the same side with the 0 gons indication on the circular grids (fig. 4.2). This convention is useful only for the evaluation of the results. In reality the TM71 device can measure only relative displacements and not absolute ones, i.e. it cannot discriminate which side of the fault has actually moved (KOSTAK 2001). Equally essential is that the positive sense of displacement on the x axis is in the direction from the centre of the circular grid to the sign of 0^g on the angle scale and on the y and z axes from the centre of the respective circular grid to the sign of 100^g on the angle scale (fig. 4.2).

-Resetting the instrument to zero

Depending on the displacement rates of each fault it may be necessary to set the instrument back to zero after each reading. This procedure should be carried out if the displacement between the reading intervals is large enough to produce Moiré patterns with a large number of fringes. In this case if the instrument is not set back to zero a further displacement in the same direction will produce a Moiré pattern with an even higher number of fringes and thus difficult to be visually evaluated and interpreted. For the circular grids the zero position can correspond to a Moiré pattern with no fringes at all or with very few fringes which will then be taken into account as an initial value to be subtracted from the actual displacements. Additionally, it is important to do any necessary temperature corrections taking into account the instrument temperature of the zero position. For the linear grids the zero position corresponds to the lowest possible number of fringes on both linear grids of the same indicator (usually about 10) and the corresponding value should be taken into account for the interpretation of the actual values.

4.1.3 The Bragg-Grating Extensometer

4.1.3.1 Description and principle of function

Optic-Fibre Bragg-Grating sensors have a wide range of applications in the areas of telecommunications, lasers and sensing techniques. In the field of sensing techniques such sensors provide temperature, pressure, displacement or strain monitoring. Geotechnical applications include strain monitoring in tunnels (SCHMIDT-HATTENBERGER & BORM 1998), boreholes (MORETTI et. al. 2002) and landslides (INAUDI et. al. 1995) as rock mechanical testing (SCHMIDT-HATTENBERGER et. al. 2003) and dynamic recording of seismic signals (LIU

et. al. 2002). The extensometers based on optic fibres containing this type of sensors are commonly known as Bragg Grating Extensometers (shortly BGX). Their main components are an optic fibre with a Bragg-Grating Sensor, embedded in a fibreglass reinforced polymer rockbolt (fig. 4.3).

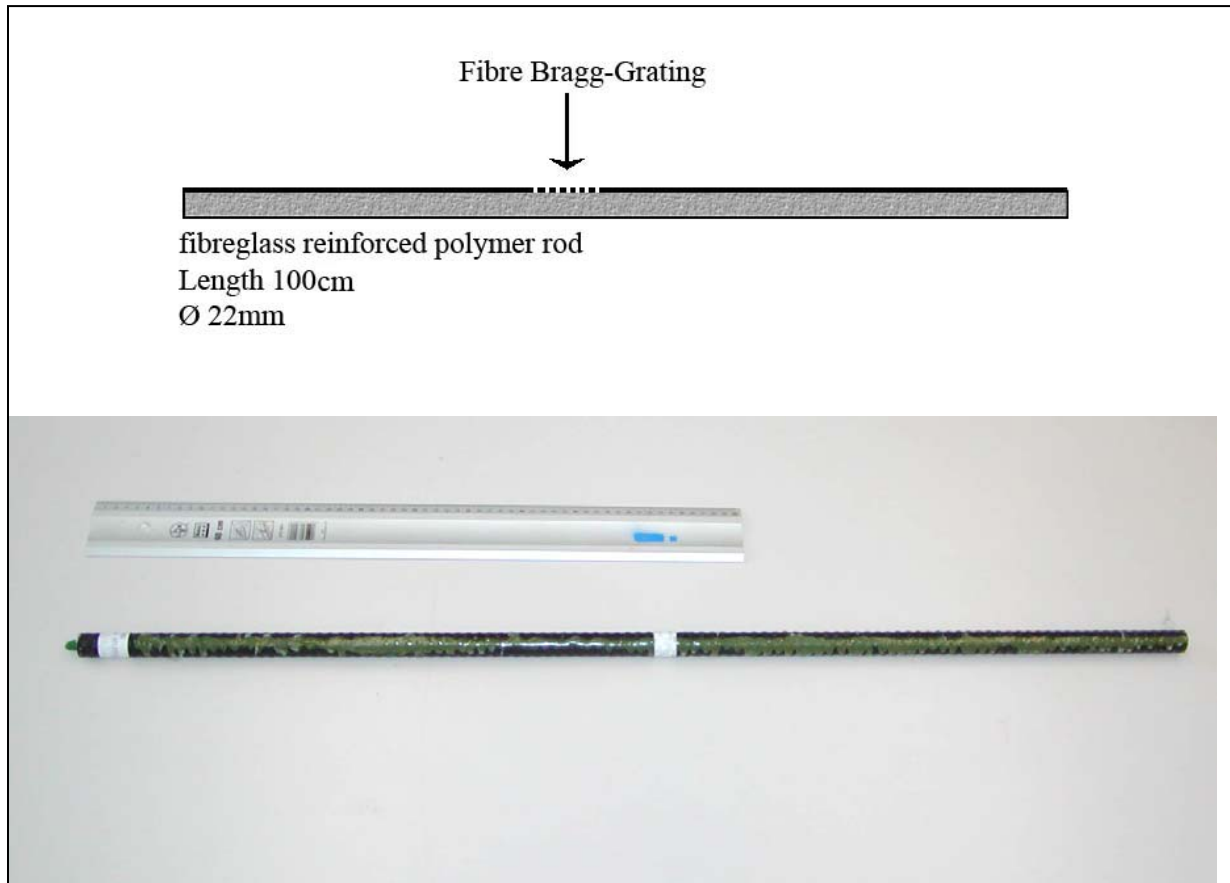


Fig. 4.3: Schematic representation (above) and an example of a Bragg Grating Extensometers rod used in the present study (below).

The most important advantages of such BGX rods in comparison to conventional sensors are: long life span, resistance in harsh and corrosive environments, high accuracy and reliability, immunity to electromagnetic interferences, array capability and compact size (SCHMIDT-HATTENBERGER et. al. 2003).

A Bragg Grating sensor is created within a segment of an optic fibre by applying a certain laser-inscription technique (ADVANCED OPTIC SOLUTIONS, 2002). This procedure produces a series of surfaces in the core of the optic fibre that are characterized by a refraction index different from the one of the regular fibre core (see schematic of fig. 4.4). The Bragg Grating, consisting of these surfaces, has a special behaviour concerning the transmission and reflection of light through the optic fibre. More specifically, for a certain wavelength, called

the Bragg wavelength (λ_{Bragg}), the light reflected by the periodically varying index of refraction is in equal phase and added constructively. As a result the Bragg Grating is reflecting the part of the spectrum with the Bragg wavelength λ_{Bragg} while letting the rest of the spectrum to be further transmitted (fig. 4.4). The diagrams in fig. 4.4 show qualitatively the working principle of the Bragg Grating with the characteristic pit in transmission spectrum, and the respective peak in the reflection spectrum of the light propagating through the fibre.

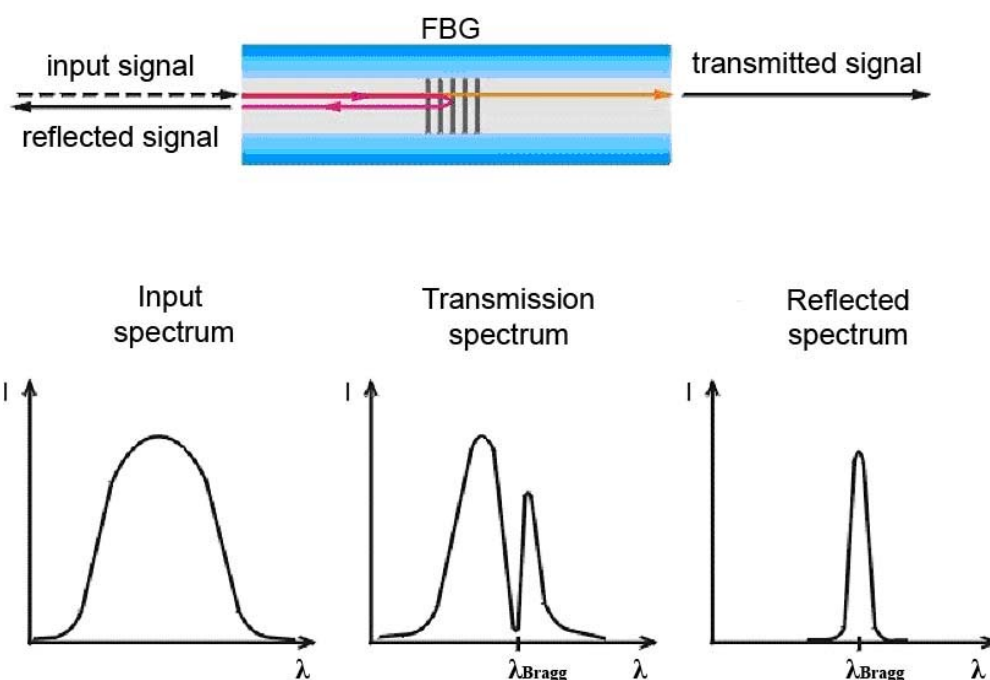


Fig. 4.4: The working principle of Fibre-Bragg-Gratings. The diagrams describe the spectral behaviour of FBG-sensors with the characteristic pit in the transmission spectrum, and the respective peak in the reflection spectrum at the Bragg wavelength value (SCHMIDT-HATTENBERGER et. al. 2003).

The Bragg wavelength is given by the equation:

$$\lambda_{\text{Bragg}} = 2 \cdot n_{\text{effective}} \cdot \Lambda \quad (1)$$

where: λ_{Bragg} is the Bragg wavelength

$n_{\text{effective}}$ is the mean refraction index of the Bragg Grating

Λ is the distance between the Bragg Grating surfaces (spatial period of the Bragg Grating)

(ADVANCED OPTIC SOLUTIONS, 2002).

The $n_{\text{effective}}$ is accordingly modulated through photoelastic and thermo-optic effects (i.e. it is sensitive to pressure and temperature changes) and Λ is modulated if the FBG is strained along the fibre axis. Therefore, after taking into consideration potential temperature effects, any shifts of the Bragg wavelength can be interpreted as strain changes (SCHMIDT-HATTENBERGER et. al. 2003).

In the case of the Bragg Grating Extensometers used in the present study, the optic fibre is firmly embedded along its entire length in an eccentric groove at the surface of a rod made of fibreglass reinforced polymer (fig. 4.3). In this way, the sensor is influenced by the local strain along the fibre axis at the point where it is fixed on the rod. The BGX rods used for this study had the sensor positioned in the middle of the rod length. The measurements of the reflected wavelength from the sensor are obtained by connecting a read out unit to the rod via a fibre optic cable and the measured values are directly transferred from the unit to a portable computer. The available read out software (ADVANCED OPTIC SOLUTIONS, 2002) offers the possibility to read up to 1000 times the λ_{Bragg} and record the average as a single value of λ_{Bragg} . If, for example, 50 single values of the λ_{Bragg} are recorded, then these actually correspond to 50000 readings. Therefore, by calculating the average of these 50 single λ_{Bragg} values any noise during the read out procedure can be practically eliminated.

4.1.3.2 Measurement of strain and deformation of the BGX rod

The response of the sensor, as a part of the fibreglass rod, to strain changes is described by the following formula (ADVANCED OPTIC SOLUTIONS, 2002):

$$\varepsilon = \frac{1}{GF} \left(\frac{\Delta\lambda}{\lambda_{\text{ref}}} - TK * \Delta T \right) \quad (2)$$

where: ε is the strain exerted on the sensor

λ_{ref} is the initial λ_{Bragg}

$\Delta\lambda$ is the shift of the reflected wavelength

ΔT is the change of temperature

TK is a Temperature Coefficient

GF is the Gauge Factor

The factors TK and GF are specific for each rod/sensor combination and compensate for the thermo-optic and the photo-elastic effect respectively

It is self-evident that the sensor undergoes strain along the fibre axis when the rod is axially elongated or shortened. The amount of elongation or shortening can be calculated if the strain measured by the sensor is extrapolated for the entire free length of the rod between the two points of fixation.

Additionally, as already mentioned, the optic fibre is embedded near the surface. This allows the Bragg Grating sensor to be axially strained also when the rod is bent because it then belongs to a convexity or concavity. Unfortunately, after simulating displacements in the laboratory it was ascertained that the sensitivity of the available BGX rod type to axial deformation is substantially higher than its sensitivity to bending. As a result, in case of simultaneous axial strain and bending of the rod the response to the axial strain overprints the response to bending. In addition the sensor response to bending cannot be interpreted unequivocally (appendix §3). Apparently, BGX rods equipped with only one optic fibre should not be considered as pure 3-dimensional instruments.

Taking these characteristics of the BGX into consideration, it can be installed on active faults perpendicularly to the fault plane i.e. as a bridge between the footwall and the hanging wall and monitor the opening or contraction movements of the fault gap.

4.2 The Perachora region (eastern termination of Gulf of Corinth)

4.2.1 Geology, Tectonics and Seismicity

At the eastern end of the Gulf of Corinth the tectonic setting changes. The large active faults are located on the Perachora peninsula (see fig. 4.5) and not on the northern coast of Peloponnesus. The Perachora peninsula is a ridge between two modern basins; the Gulf of Alkyonides to the north (with water depths of less than 400m) and the Gulf of Lecheo to the south (with water depths less than 200m) (ROBERTS & GAWTHORPE 1995) (fig. 4.5).

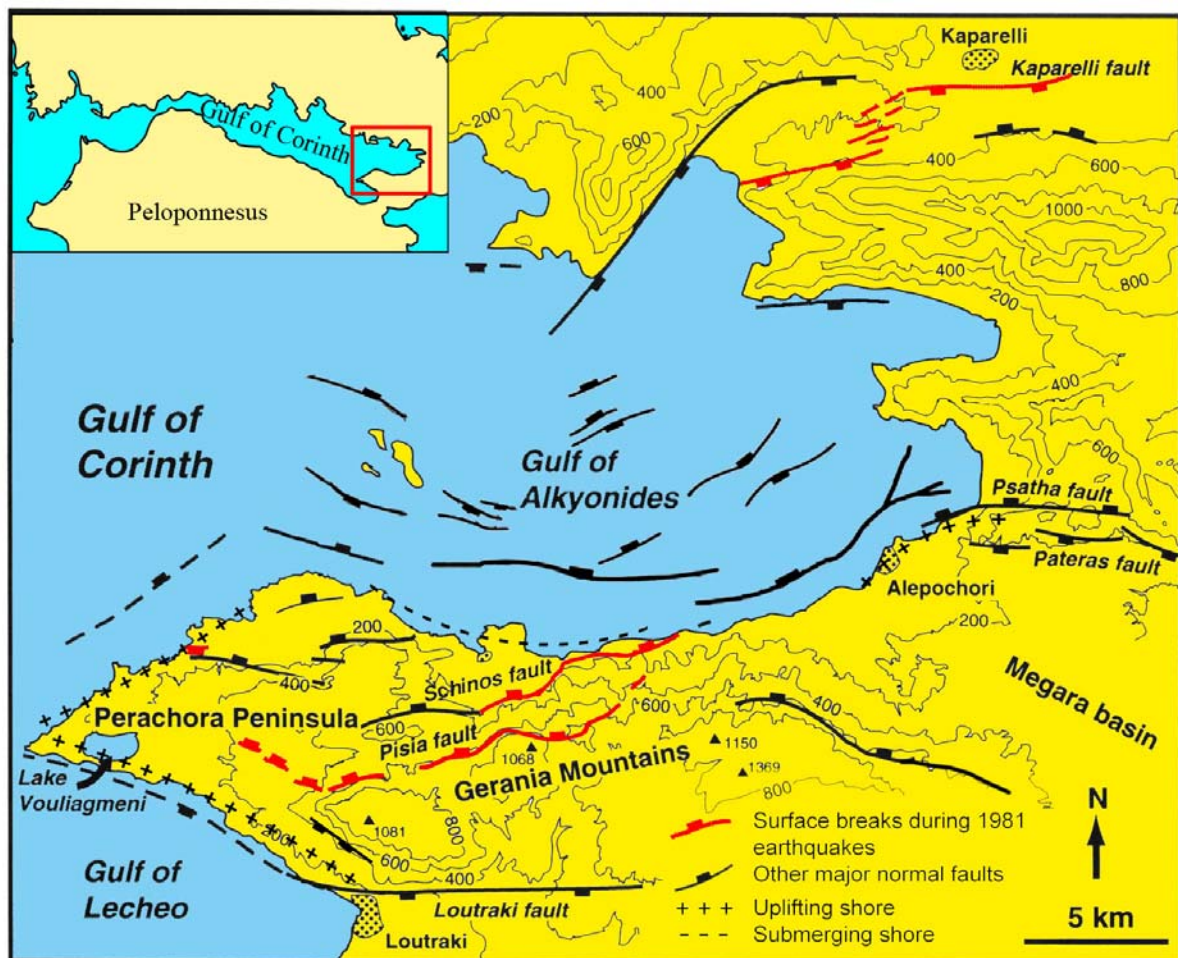


Fig. 4.5: Overview map of the tectonic setting at eastern end of the Gulf of Corinth (based on ROBERTS & GAWTHORPE 1995, LEEDER et al. 2002, JACKSON et al. 1982)

In terms of basement geology, at the Perachora region predominant are Mesozoic limestone (mostly Triassic-Jurassic) and a schist-chert series, upon which large masses of ophiolites have been thrust. All these formations belong to the so-called Unit of Eastern Greece. The Neogene-recent stratigraphy of the Perachora peninsula consists of Holocene fluvial, coastal and alluvial deposits as well as beach and shore-face deposits of Pleistocene age overlying Pliocenic marls (I.G.M.E. 1984).

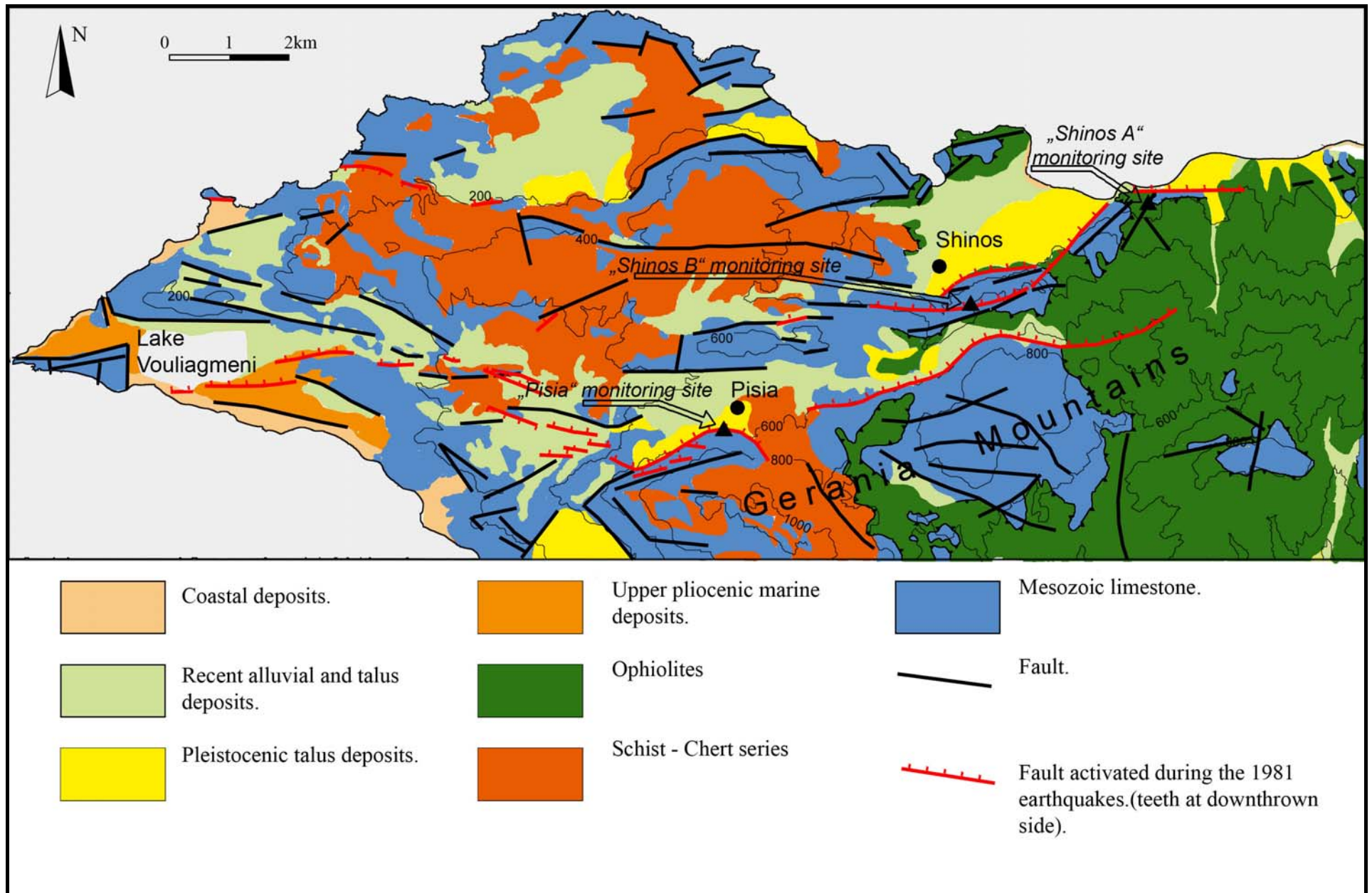


Fig.4.6: Geological map of the Perachora peninsula (based on I.G.M.E. 1984) containing the locations of the fault monitoring sites.

The morphology is controlled by active normal faults. Most prominent morphological feature on the Perachora peninsula is an E-W orientated, north facing, double escarpment induced by the Pisias-Shinos fault zone named after two abutting villages (fig. 4.6). This fault zone comprises the southern structural margin of the Gulf of Alkyonides which is an active graben structure (STEFATOS et al. 2002). The Pisias-Shinos fault zone consists of two en-echelon E-W striking faults the so called Pisias fault to the south and the Shinos fault to the north. Both of them are north dipping normal faults with dip angles of 40-65° and they strike mostly through Mesozoic limestone. The cumulative uplift on the footwall of the Pisias-Shinos fault zone has formed a morphological throw of 1100m. Another significant fault on the Perachora peninsula is the south-dipping Loutraki fault which borders the peninsula to the south and together with the Pisias-Shinos fault zone forms the horst of the Gerania mountains (fig 4.5).

As mentioned above, the fault activity has migrated northwards at the East Gulf of Corinth i.e. from the coast of Peloponnesus to the Perachora peninsula but the orientation of the active faults has also changed (ARMIJO et al.1996, COLLIER et al.1992). The Pisias-Shinos and Psatha faults as well as the offshore ones along the northern coast of the Perachora peninsula (LEEDER et al. 2002) are E-W to WSW-ENE orientated and have obliquely cut the older NW-SE orientated faults that bound the Megara basin (fig 4.5). Due to uplift on the footwalls of the younger E-W trending, north-dipping faults, the plio-pleistocenic sediment fill of the Megara basin has been tilted towards SE (COLLIER et al. 1992). The same authors as well LEEDER & JACKSON (1993) determined that the younger fault activity comprising the E-W trending faults initiated 1mio years ago.

The Pisias-Shinos fault zone is seismically active. Most characteristic seismic events were the ones during the earthquake sequence of 1981. A series of three strong earthquakes (February 24, 1981, 6,7Ms; February 25, 1981, 6,4Ms; March 04, 1981 6,4Ms) struck the region and several surface ruptures were observed (JACKSON et al. 1982, KING et al. 1985). The first two events ruptured the Pisias and Shinos faults whereas the third event ruptured the antithetic Kaparelli fault on the northern coast of the Gulf of Alkyonides (see fig 4.5). The amount of seismic displacement on of the Pisias and Shinos faults was in average 0,5-0,7m and had a maximum of 1,4m (COLLIER et al. 1998). Other ground deformation phenomena due to these earthquakes included displacements on minor faults in the hanging wall (hanging wall internal deformation), ground cracking and liquefaction phenomena.

The intense tectonic activity of the Perachora peninsula is imprinted by significant coastal uplift and subsidence along its shorelines (fig 4.5). More precisely, the shorelines which belong to the footwalls of the major faults (Pisia-Shinos and Loutraki faults) are uplifted. MOREWOOD & ROBERTS (1999) report uplifted marine terraces along the southern coast of Perachora peninsula (between Loutraki and Vouliagmeni lake). Further to the west, raised solution notches containing *Lithophaga* shells are visible along the coast. The coastal uplift is the result of episodic and long-term tectonic movements (ROBERTS & GAWTHORPE 1995, PIRAZZOLI et al 1994). The northern coast of the peninsula is located on the hanging wall of the Pisias-Shinos Fault zone and therefore it is submerging. Here, the long term submergence during the quaternary is expressed by drowned alluvial fans, talus cones, swamps and small lagoons (LEEDER et al. 1991 and 2002). Additionally, episodic submergence along the coastal area of Shinos was ascribed to the 1981 earthquake sequence (JACKSON et al. 1982, HUBERT et al. 1996). Significant coastal uplift occurs again further to the east near Alepochori on the footwall of Psatha fault (COLLIER et al 1992).

4.2.2 The Pisias fault zone

The outcrops of the Pisias and Shinos faults offer a unique opportunity to study an active tectonic zone where extension and uplift is accommodated. The Pisias fault zone has a total length of 16km and has formed an escarpment of 400m meter height south of Pisias. The escarpment continues towards the west with a lower topographical expression as it leaves the limestone flanks of the Gerania mountains and continues through lower relief towards the lake of Vouliagmeni. The strike direction of the Pisias fault changes from WSW-ENE at the eastern parts to a more WNW trend towards the west (see fig. 4.6). To the east the Pisias fault extends ca.7km from Pisias and terminates after a major change of the basement geology from Mesozoic limestone to ophiolites.

During the 1981 earthquake sequence, the Pisias fault zone demonstrated co-seismic displacement on fault segments along its entire length (fig. 4.6) (JACKSON et al. 1982). The displacements had a dip-slip sense of motion and the hanging wall was downthrown. The co-seismic displacement increased gradually from a few centimetres near Vouliagmeni lake to 1m at the segment south of Pisias and reached a maximum of 1,5m further to the east at the longitude of Shinos before attenuating to 20cm at the eastern termination of the fault within the ophiolites (JACKSON et al. 1982). In the central part of the fault zone the co-seismic ruptures took place at the base of the fault escarpment between the Mesozoic limestone of the

footwall and the alluvial or talus deposits of the hanging wall. In some other cases, the rupture reached the surface by displacing the softer hanging wall lithologies immediately in front of the main fault plane.

4.2.3 The Shinos fault zone

The Shinos fault is sub-parallel to the Pisia fault zone in an en-echelon setting and has a length of 10km. It is also north dipping and mostly juxtaposes Mesozoic limestone to plio-pleistocenic and recent talus cones (I.G.M.E. 1984). The western tip of the Shinos fault zone is located at the longitude of Pisia. South of Shinos village, the fault zone is characterized by 3-4 parallel faults at the base and at higher parts of the fault escarpment which has a morphological throw of 400m (fig. 4.6). Towards the east, the fault zone continues parallel to the shoreline and then offshore.

The 1981 earthquake sequence ruptured the central and eastern segments of the Shinos fault in a dip slip sense. In the central segments, the co-seismic displacements were 30-60cm whereas at the east displacements of up to 1m were observed within alluvial fans (JACKSON et al. 1982, COLLIER et al. 1998, PANTOSTI et al. 1996). Compared to the co-seismic ruptures of the Pisia fault, the ruptures on the Shinos fault had a more discontinuous character (JACKSON et al. 1982). Paleoseismological evidence on the Shinos fault (COLLIER et al. 1998, PANTOSTI et al. 1996) has revealed that the average recurrence interval of earthquakes similar to those of 1981 is 330 years. However this interval is representative only for the eastern part of the Shinos fault zone and may not be valid for the entire Pisia-Shinos fault zone.

4.2.4 Fault kinematics and stress field evaluation along the Pisia-Shinos fault zone

The footwall of the Pisia-Shinos fault zone, especially in the central parts of the zone, consists of Mesozoic limestone. Compared to the ophiolites and the alluvial and talus deposits, the limestone is more resistant to erosion and therefore kinematic evidence is better preserved on the limestone surfaces at the base of the fault escarpments.

The kinematic evidence consists of striations and corrugations which were created at depth during previous fault displacements and now are exposed at the surface due to footwall uplift. By studying this type of kinematic evidence, it is therefore possible to determine the stress field which caused the corresponding movements in the past and compare it with the current

stress/strain regime which is evaluated by GPS based geodesy, analysis of focal mechanisms, in-situ monitoring of fault displacements, etc.

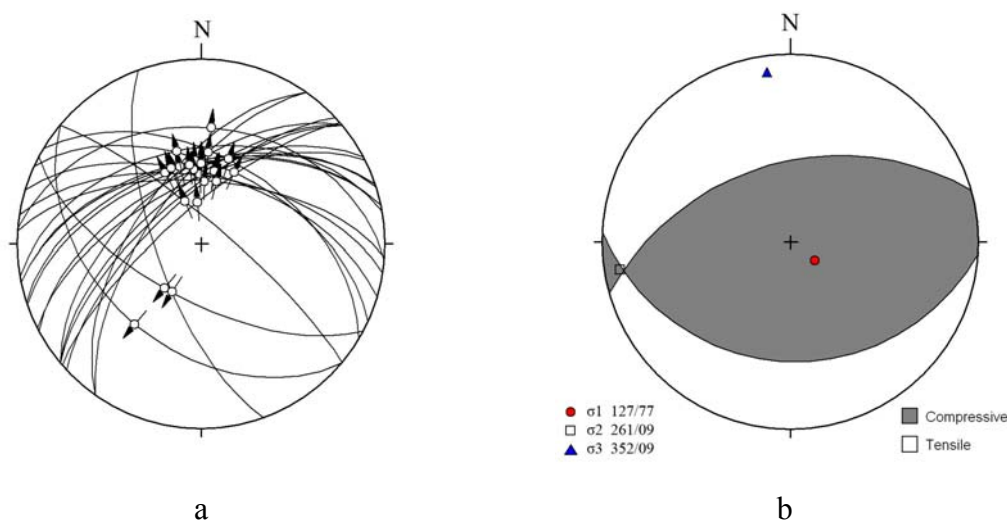


Fig. 4.7: a. Lower hemisphere projections of fault planes and the respective slip vectors (striations and corrugations) along the main segments of the Pisia-Shinos fault zone. b. Stress-field interpretation of the slip vectors and the respective faults by the use of the Right Dihedra method.

Fig. 4.7a shows the lower hemisphere projections of fault planes along the Pisia-Shinos fault zone and the respective slip vectors. Most of these features (striations and corrugations) were observed on limestone fault planes and some of them on ophiolites. These data were interpreted by using the Right Dihedral method (ANGELIER & MECHLER 1977) in the same way as in chapter 2 and the result is summarized in fig. 4.7b. The right dihedral method yields a σ_3 (minimum compressive stress axis) directed at 352/09, a σ_2 (intermediate compressive stress axis) directed at 261/09 and a σ_1 (maximum compressive stress axis) directed at 127/77.

The sub-vertical σ_1 axis and the approximately north-directed σ_3 , which were ascertained above for the Perachora peninsula, are in good agreement with the general stress regime of N-S orientated extension of the Gulf of Corinth. However, there is a discrepancy in relation to the stress field determined for the central part of the southern coast of the Gulf of Corinth in chapter 2. More precisely, the σ_3 direction along the Pisia-Shinos fault zone is NNW (352/09) whereas at the central part of the southern coast of the Gulf of Corinth, the σ_3 is NNE directed (between 012/06 and 015/06) (fig. 4.8).

It is known that the approximately E-W trending faults at the Perachora peninsula (i.e. the Pisia-Shinos and Psatha faults as well as the offshore ones between them) are younger structures initiated approximately 1 Mio years ago (COLLIER et al. 1992, LEEDER & JACKSON

1993). The aforementioned faults truncated the pre-existing, WNW-ESE trending, boundary faults of the Megara basin (fig. 4.5) which were formed under the stress field that is still active in the central part of the southern coast of the Gulf of Corinth. Therefore, it can be stated that approximately 1Mio years ago the direction of the σ_3 , i.e. the direction of extension, changed at the Perachora peninsula from NNE to NNW (fig. 4.8). The new stress field created E-W directed faults at the Perachora peninsula such as the Pisias and Shinos faults and rendered older WNW-ESE faults inactive.

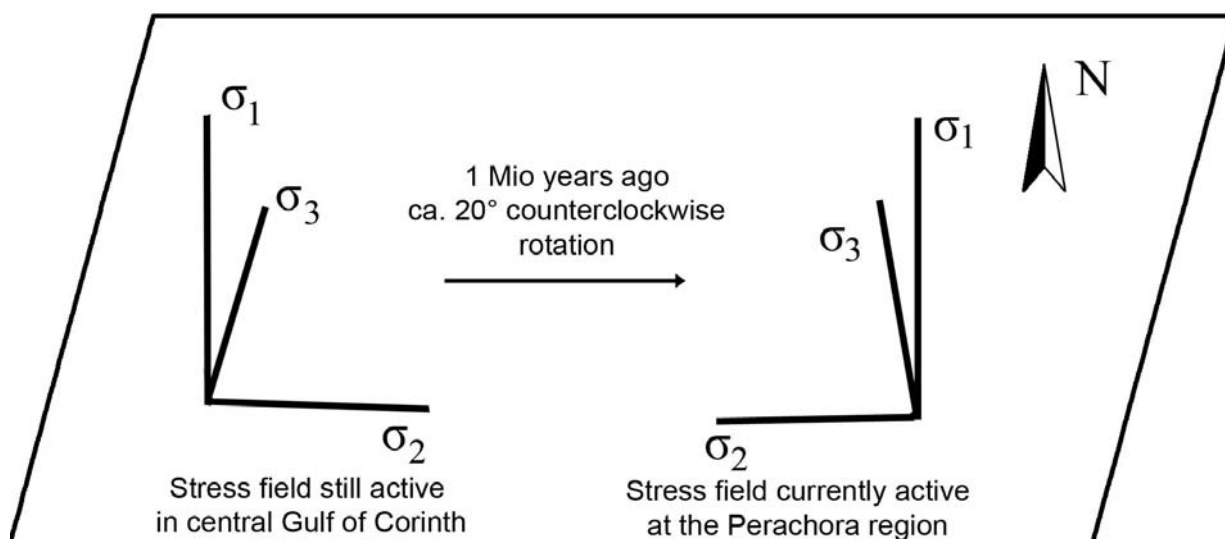


Fig. 4.8: Schematic showing the change of the stress field at the Perachora peninsula 1Mio years ago. Practically the previous stress field which is still active at the central Gulf of Corinth was rotated 20° counterclockwise about a nearly vertical axis.

Furthermore, the extension direction of 352° resulting from the application of the right dihedral method at the Perachora peninsula is in agreement with the mean slip direction of 350° of the 1981 earthquake surface ruptures (JACKSON et al. 1982, MOREWOOD & ROBERTS 2001) and is similar to that of the focal mechanism solutions of the same earthquakes (JACKSON et al. 1982, HUBERT ET AL. 1996). In addition, GPS based studies such as the one of CLARKE et al. (1998) also concluded that the direction of current, local extensional strain at the Perachora peninsula is similarly NNW-SSW orientated. Also based on GPS geodesy, BRIOLE et al. (2000), determined that the direction of extension at the eastern Gulf of Corinth is orientated towards 341°. The aforementioned data imply that the stress field of the last 1 Mio years at the Perachora peninsula remains the same until today.

4.3 Selection, location and description of the fault monitoring sites

4.3.1 Selection of monitoring sites

In order to install monitoring instruments along the active faults on the Perachora peninsula a careful fieldwork in combination with literature study was carried out. During this process several factors were taken into consideration. First of all the monitoring sites had to be at locations where the potential tectonic activity is expected to be high. This selection was done by combining information such as reports on the local earthquake activity, the historically recorded fault displacements as well as field observations on the exposed fault planes themselves in order to locate evidence of recent displacements and morphological features which prove the existence of recent activation. Second, the technical issues had to be taken in consideration. The potential monitoring sites had to provide the appropriate lithological and morphological conditions so that the installation and the function of the instruments would be successful. It was essential, at the places of installation, that the rocks demonstrated good mechanical properties which would ensure a stable fixation of the instruments. Another important prerequisite was that the necessary mounting points for the instrument on the footwall and hanging wall had to be available within a reasonable distance from each other. This would allow a relatively easy installation without the application of large metal parts and excessive cement quantities. Simultaneously, a short instrument bridge between footwall and hanging wall would minimise the potential measuring error induced by dilatation of large metal parts due to temperature fluctuations. It was particularly taken care that all instrument bridges at the monitoring sites would be of a linear form and perpendicular to the respective fault planes. This meant that the temperature fluctuations would have an effect only on the measurements concerning the contraction or extension of the fault opening (i.e. perpendicularly to the fault plane) whereas the measurements along the dip-slip and strike slip direction would not be influenced. Finally, the accessibility of the different locations was an important factor as relatively easily accessible monitoring sites would allow an easier transport of the equipment necessary for the installation. According to these prerequisites three monitoring sites were selected on the Perachora peninsula.

4.3.2 The “Pisia” fault monitoring site

The first site that was selected for the installation of fault monitoring instrument is located at the southern segment of the Pisias – Shinos fault at the Perachora peninsula immediately south of the village of Pisias (see fig. 4.6). Locally the footwall consists of crystalline triassic limestone and the hanging wall consists of relatively loose pleistocenic material containing

embedded limestone blocks of different sizes. According to JACKSON et al. (1982) and I.G.M.E. (1984), this fault segment was reactivated during the earthquake sequences of February and March of 1981 in the area of the Alkyonides gulf. The co-seismic displacement was approximately 1m (JACKSON et. al. 1982) and had a normal, almost dip-slip character. At the location of the monitoring site the fault plane has a general dip direction and dip of 340/43. The local morphology is characterized by a gully ascending to the East which is formed by the limestone escarpment to the south (footwall) and a hill of pleistocenic material to the north (hanging wall) (fig. 4.9).



Fig.4.9: The selected location along the Pisia fault escarpment for the first installation of the TM71 and the Bragg Grating Extensometer. In the background, the gully where the instrument were installed is visible. On the right (south) the fault plane on Triassic limestone (footwall) is visible whereas on the left (north) the hanging wall consists of pleistocenic material.

At the exact location of the monitoring instruments the fault plane dips at 355/40. This location was selected due to the presence of a large limestone block embedded in the pleistocenic debris of the hanging wall. A direct and simultaneously stable instrument fixation into the loose material of the hanging wall wouldn't have been possible. This limestone block was used as a very reliable mounting point for the instruments into the hanging wall due to its stability and its large dimensions (approx.0.5 x 0.7 x >1.20m). The above mentioned characteristics ensured that this limestone block was firmly embedded within the pleistocenic

loose material and would move together with the hanging wall in the case of fault displacements. Another characteristic of the Pleistocene deposits, which provides the stability of the limestone block within them, is their grain size distribution. A sample was analysed in the laboratory and it was found that the grain size distribution of the Pleistocene deposits corresponds to that of a Fuller curve (appendix §4). Hence the density index of the deposits is high and the deposits provide a stable support for the limestone block.

4.3.2.1 The TM71 device at the “Pisia” monitoring site

At the location described above, a TM 71 instrument was installed at the end of February 2002. Due to its proximity to the fault plane (less than 40 cm) the aforementioned limestone block allowed a simple installation technique and a very short instrument bridge between the footwall and the hanging wall. The latter minimised the potential measuring error induced by dilatation due to temperature fluctuations.

In order to prepare the necessary space for the instrument, a part of the block was cut and a short borehole was drilled perpendicularly to the fault plane through the limestone block and further into the footwall (fig. 4.10 and 4.11). The prepared hole had a diameter of 7cm and lengths of 22cm and 18cm in the hanging wall block and in the footwall respectively. The TM 71 was installed by using the standard steel bars provided with the instrument. The steel bars were cemented into these holes by a mixture of cement, sand and cement accelerator which was left for 24h to harden. Afterwards, the TM 71 instrument was installed between the 2 bars as well as a protective steel case (fig. 4.11). The monitoring of the fault displacements began on the 23rd of February 2002 after setting the instrument to zero. As mentioned above, the instrument bridge (fig. 4.10 and 4.11), is perpendicular to the fault plane, this allowed the x, y and z components of the Moiré indicators of the device to coincide with the direction perpendicular to the fault plane, the strike slip direction and the dip slip direction respectively (fig 4.10). Hence, these components of motion could be measured directly. The total length of the steel bridge i.e. the length of the instrument and the length of the steel bars protruding between the footwall and hanging wall is 40cm. This, in addition with the fact that the bridge is of a linear form minimize the effects of temperature dilatation on the device. Besides, the gully, where the monitoring site is located, is narrow with an E-W orientation and in combination with the fault escarpment rising to the south it provides a good protection against direct sunlight to the monitoring device and therefore reduces the amplitude of daily temperature fluctuations of the bridge.

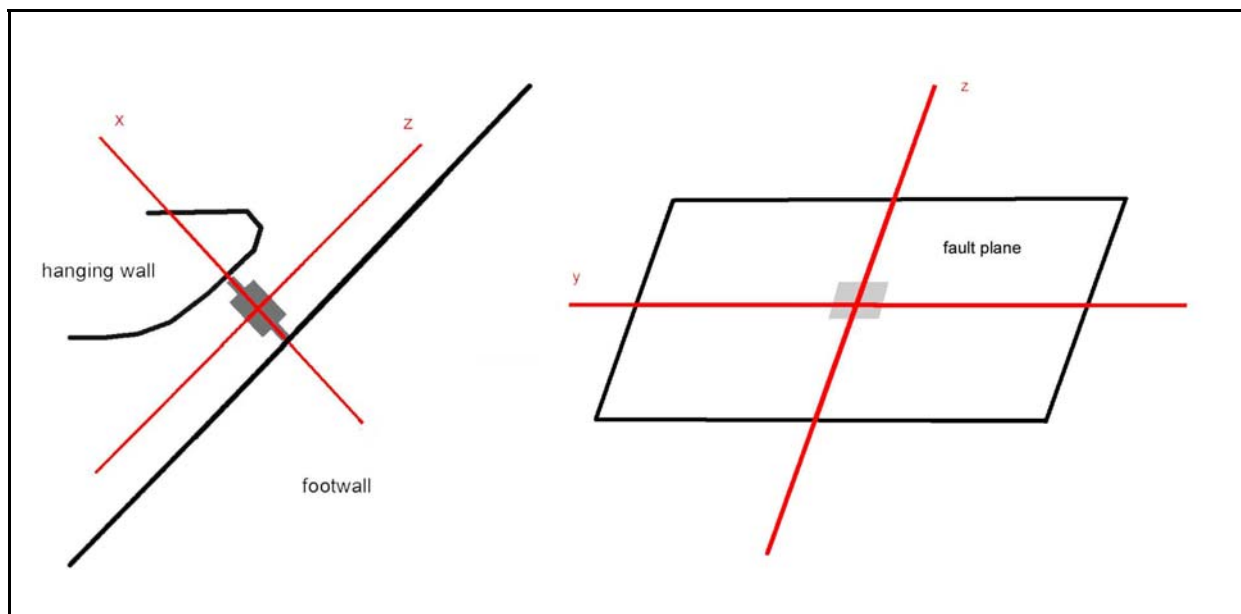


Fig. 4.10: Schematic representation of the spatial orientation of the TM71 at the Pisia monitoring site. The TM71 measures the displacement along three directions. At the Pisia monitoring site the TM71 measures displacements along the dip-slip direction (z component), the strike slip direction (y component) and the direction which is perpendicular to the fault plane (x component).

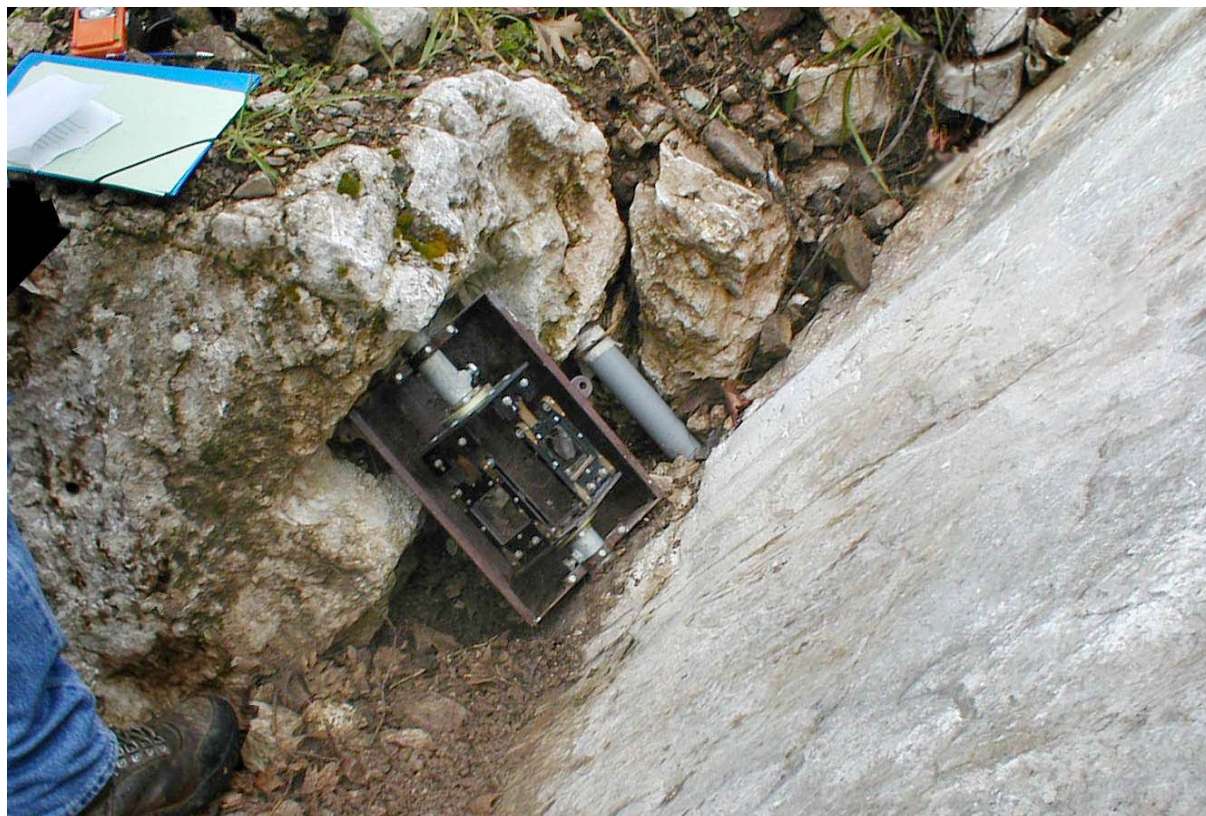


Fig. 4.11: The TM71 and the BGX rod installed at the Pisia monitoring site between the footwall and the hanging wall of the fault. In the hanging wall (left hand side on the photograph), the instruments are fixed within a limestone block which is firmly embedded in the pleistocenian deposits. Behind the TM71, the PVC tube which protects the BGX rod is visible.

4.3.2.2 The Bragg-Grating Extensometer (BGX) at the “Pisia” monitoring site

In order to implement the BGX rods for monitoring fault displacements, an installation similar to that of the TM71 instruments was adapted. It was decided to cement the two ends of the rod into the hanging wall and the footwall respectively and use a PVC tube to protect the free length of the rod in the middle (fig. 4.11 and 4.12). Moreover the BGX rod was chosen to be parallel to the TM71 instrument bridges i.e. perpendicular to the fault plane (fig. 4.12). The ends of the BGX rod were fixed into drilled holes of 7cm diameter and lengths of 16.5cm and 34cm within the footwall and the hanging wall respectively. The free length of the rod between the walls of the fault was 39.5cm long. The sensor area was located on the free length of the rod between the fault walls at a distance of 8cm from the hanging wall. This kind of installation allows any relative displacement of the walls of the fault to induce a deformation on the rod and therefore to the sensor itself.

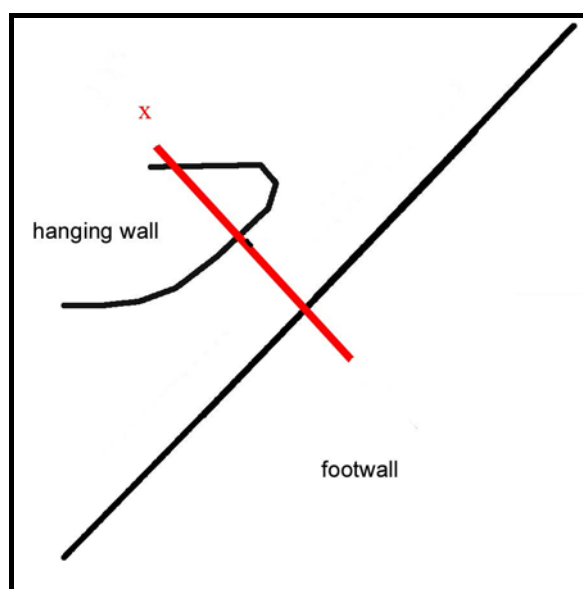


Fig. 4.12: Schematic drawing of the Bragg-Grating-Extensometer rod (BGX) at the Pisia monitoring site. The rod axis is perpendicular to the fault plane which allows the monitoring of the displacements along this direction.

However, as shown in appendix §3, for this type of installation, the sensitivity of the BGX rod to axial strain overprints its response to bending. Therefore the BGX rod at the Pisia monitoring site functions as a 1D monitoring instrument measuring the displacement component which is perpendicular to the fault plane (opening or contraction of the fault gap, same as the x component of the TM 71). The monitoring of the fault by using This BGX rod began on the 10th of May 2002 by taking the initial reading of the BGX rod which was used as the reference value.

4.3.3 The “Shinos A” monitoring site

The second monitoring site is located east of Shinos village at the most eastern onshore segment of the Shinos fault. At that particular location (see fig. 4.6) an E-W trending 2km long fault segment was activated during the earthquakes of February and March of 1981 and displayed co-seismic displacements of ca. 60 cm (JACKSON et. al 1982). Towards the west, the fault segment splays into 2 faults, one following the E-W trend and one striking SW. The instruments were installed approximately 100m SW from the point of splay and on the SW trending segment is the monitoring site (fig. 4.6).



Fig. 4.13: Overview of the location on the eastern segment of the Shinos fault which was selected for the installation of the second monitoring site. In the background, the hanging wall (right hand side in the photograph) as well as the footwall (on the left) consist of Triassic limestone.

Although the fault separates generally limestone from ophiolites, on the particular point of the monitoring site the fault plane is within limestone (fig. 4.13). The general dip direction and dip of the fault are 330/72, whereas at the particular point of installation the fault dips at 310/75. The installation was carried out in a similar way to that in Pisia.

4.3.3.1 The TM71 device at the “Shinos A” monitoring site

As seen in fig.4.14 there was no space between the hanging wall and footwall at the point of installation and therefore a cavity had to be prepared. Despite the difficulty of this preparation the advantage was that the instrument bridge would be as short as possible. The necessary borehole of 7cm diameter was drilled perpendicularly to the fault plane through the hanging wall part into the footwall with lengths of 35cm and 28cm respectively. The fixation of the TM71 Moiré gauge was achieved by cementing the standard steel bars into the boreholes with a simple cement and sand mixture. This kind of installation allowed the shortest possible instrument bridge with a total length of 42cm between the footwall and the hanging wall blocks. One day later (11th October 2002) the TM71 was fixed on the steel bars and was set to zero.



Fig. 4.14: At the monitoring site on the eastern segment of the Shinos fault, the TM71 was installed within an artificial cavity between the footwall and the hanging wall of the fault. The BGX rod was installed behind and above the TM71, also perpendicularly to the fault plane. (Only the protruding end of the BGX rod is visible in the photograph).

The orientation of the instrument in relation to the fault plane provided a direct measurement of the displacements along the direction perpendicular to the fault plane, the strike slip direction and the dip slip direction in the same way as the TM71 at Pisia (fig. 4.15)

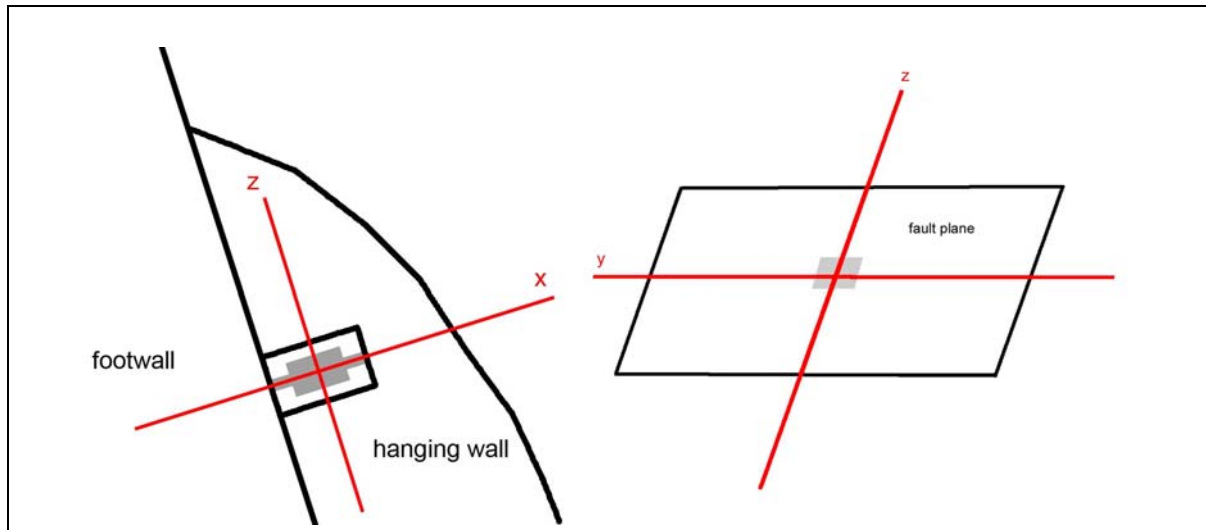


Fig. 4.15: Schematic drawing of the TM71 configuration at the monitoring site on the eastern segment of the Shinos fault. The TM71 measures directly the displacements along the dip-slip direction (z component), the strike slip direction (y component) and the direction which is perpendicular to the fault plane (x component).

4.3.3.2 The Bragg-Grating Extensometer (BGX) at the “Shinos A” monitoring site

Next to the TM 71 at the Shinos monitoring site, a BGX rod was also installed on the 10th of October 2002 (see fig 4.14). The BGX rod was installed perpendicularly to the fault plane (i.e. parallel to the x component of the TM 71) and consequently could measure the displacement along this direction (fig. 4.16). Between the footwall and the hanging wall of the fault, where the sensor was located, the free length of the rod was 15cm while cemented parts of the rod in the footwall and hanging wall had lengths of approximately 40cm and 35cm respectively (fig. 4.16). The application of the BGX rod began on the 3rd of January 2003 by taking the first measurement, which served as the reference value (zero value).

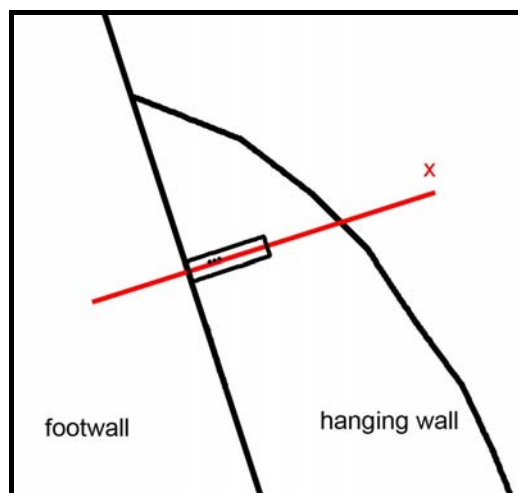


Fig. 4.16: Schematic drawing of the Bragg-Grating-Extensometer rod (BGX) at the monitoring site on the eastern segment of the Shinos fault. The rod axis is perpendicular to the fault plane which allows the monitoring of the displacements along this direction. The sensor area of the rod is situated in an artificial cavity within the hanging wall block.

4.3.4 The “Shinos B” monitoring site

The third and last monitoring site is situated at the top of the Shinos fault escarpment, SE of the Shinos village (fig. 4.6). According to I.G.M.E. (1984) at this location a segment of the Shinos fault was activated by the earthquakes of 1981. The location is characterised by several small step-like, E-W orientated scarps formed within moderately karstified limestone of Triassic age. The height of these scarps varies between some decimetres and 2m and their length between ca. 10 and 50m.

4.3.4.1 The TM71 device at the “Shinos B” monitoring site

It was decided to install the TM 71 instrument at the base of the southernmost and most prominent scarp (fig. 4.17).



Fig. 4.17: Overview of the scarp which was selected for the installation of the third monitoring site.

Locally, the scarp is 2m high and almost vertical with a strike direction of approximately 110° . The layout of the installation (fig. 4.18) was similar to that of the Pisia monitoring site, where the instrument was installed between the footwall and a large block of limestone belonging to the hanging wall. The x component of the TM71 was perpendicular to the scarp wall while the other two components (y and z) were along the strike and dip slip direction

respectively (fig. 4.19). The mounting of the instrument was achieved by cementing the two steel bars into two inline boreholes, one in the scarp wall (footwall, 30cm long) and the other one in a limestone block of the opposite side (hanging wall, 20cm long) (fig. 4.18). The large size of the block (1m x 50cm x 40cm) provided with the necessary stability on the hanging wall side. In the case of this fault monitoring site, the free length of the instrument bridge between the hanging wall and the footwall was significantly longer (105,5cm). On the 5th of February 2003 the fault monitoring commenced by setting the instrument to zero.

Unfortunately, a parallel installation of a BGX rod was not possible because the distance between the selected limestone block and the footwall was longer than the length of the BGX rod. Moreover, there was no other location along the scarp suitable for an installation of a BGX rod.



Fig. 4.18: The TM71 was installed between the footwall to the left and a limestone block laying on the hanging wall to the right.

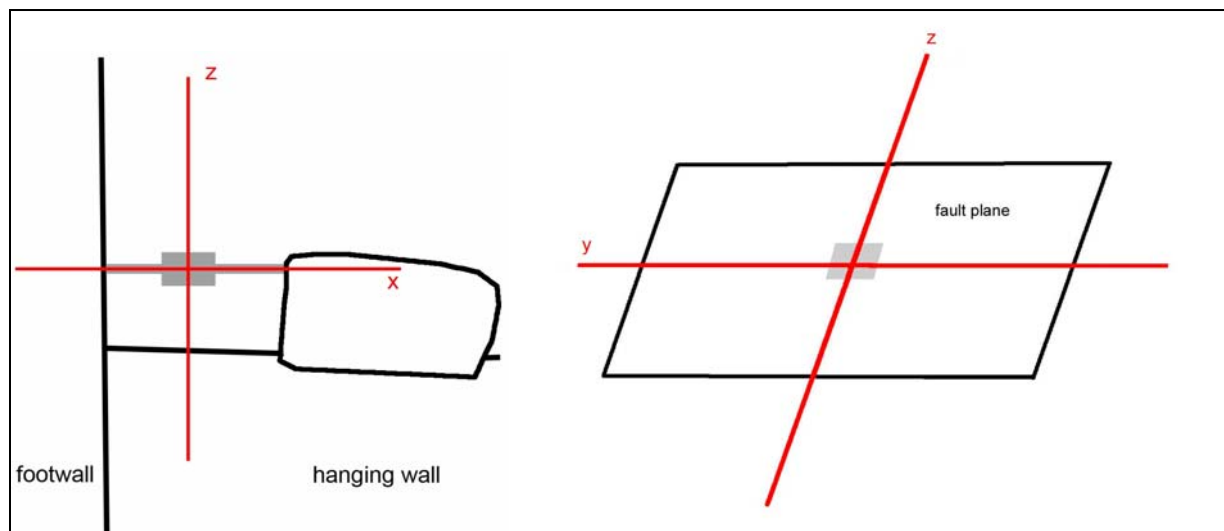


Fig 4.19: Also at this monitoring site, the orientation of the TM71 allowed a direct measurement of the along the dip-slip direction (z component), the strike slip direction (y component) and the direction which is perpendicular to the fault plane (x component).

4.4 Evaluation of the monitoring results

4.4.1 Results from the Moiré extensometer (TM71) at the “Pisia” fault monitoring site

The diagrams of fig. 4.20 depict the monitored displacement behaviour of the Pisía fault at the “Pisia” monitoring site. As already mentioned the TM71 at this monitoring site could measure directly the displacement perpendicularly to the fault plane, the displacement along the dip slip direction as well as along the strike slip direction (see also appendix §5).

The displacement monitoring by means of TM71 commenced on the 23rd of February 2002 and the last reading was obtained on the 1st of August 2005. During the monitoring period, 11 measurements were obtained at this monitoring site. The time intervals between the measurements had durations of 3-6 months, apart from the last one which was significantly longer (10 months). After each reading, the instrument was set back to zero. This procedure was necessary because the displacements were relatively large and they induced dense Moiré patterns on the Moiré indicators of the TM71. Without resetting the instrument back to zero after each reading, the Moiré pattern would become denser with time and it would have been very difficult to read and evaluate the Moiré patterns (KOSTAK & CRUDEN 1990).

All three diagrams describing the displacement at the Pisía monitoring site, demonstrate an oscillating character. However, clear trends were established during the monitoring period along all three components of motion. The factors and the mechanisms behind the climatic depended oscillations of the displacement values will be commented later in this chapter.

Along the dip slip component (fig. 4.20a) of motion the cumulative displacement had reached a total of 1,39mm of normal-slip at the end of the monitoring period. The average rate of normal-slip was 0,44mm/year. A similar behaviour was observed along the strike slip component of motion (fig. 4.20b). Here, the cumulative displacement at the end of the monitoring period was 1,5mm of sinistral movement whereas the average rate was 0,40mm/year. Finally, at the time of the last measurement, the displacement perpendicularly to the fault plane (fig. 4.20c) had reached the amount of 0,62mm in the direction of extension i.e. the fault gap was opening and its average rate through the monitoring period was 0,18mm/year.

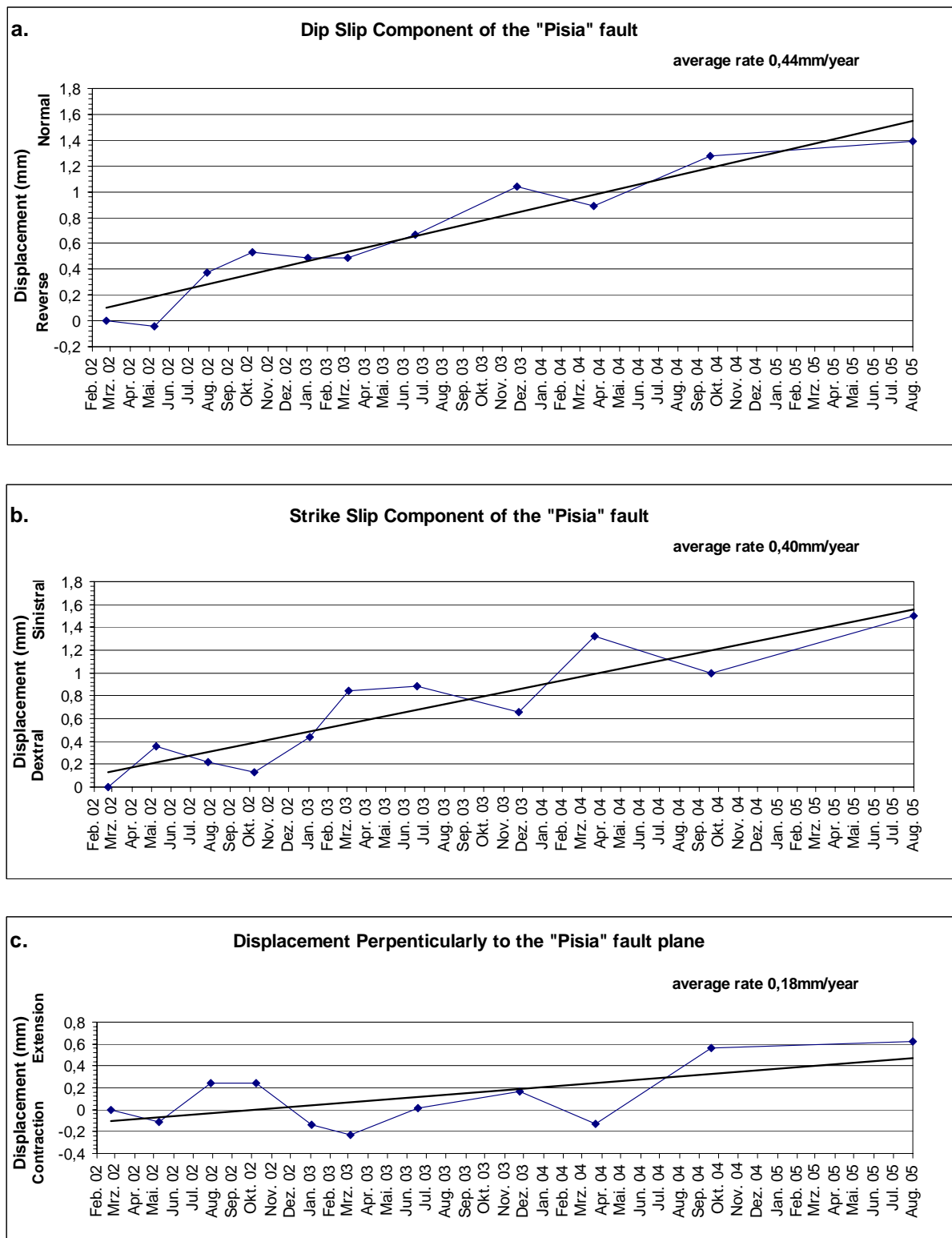


Fig. 4.20: Displacement progress at the "Pisia" monitoring site as measured by means of Moiré extensometer (TM71 device).

As far as the oscillations are concerned it is obvious that they have a clearly seasonal character. More precisely, in fig. 4.20a is apparent that during the warm months displacements in the normal sense of motion were being recorded whereas during winter weaker displacements toward the opposite direction (reverse slip) were taking place. Nevertheless, there was a prevailing displacement direction of normal sense. The displacement progress along the strike slip component of measurement has a similar characteristic (fig. 4.20b). The fault demonstrates an overall sinistral movement. However, due to seasonal effects, the sinistral movements were accentuated during winter whereas in summer weaker dextral trends were being displayed. Perpendicularly to the fault plane (fig. 4.20c), a similar effect was observed. The fault gap was contracting during winter and was conversely opening during summer. Nonetheless, the displacement trend along this direction is weak and practically the fault gap remained stable.

4.4.2 Results from the Bragg-Grating extensometer (BGX) at the “Pisia” fault monitoring site

Parallel to the TM71, as already mentioned, a Bragg-Grating Extensometer (BGX rod) was installed at the Pisia monitoring site. The fault monitoring by using the BGX device started on the 10th of May 2002 and the last measurement was obtained on the 1st of August 2005. It was not possible to take a reading from the BGX rod on every readout campaign as a readout unit was not regularly available. Nonetheless, since December 2003 a readout unit had always been available and a total of 6 readings (including the initial reference reading) were carried out (fig. 4.21) (see also appendix §6). Each reading by means of the BGX rod was carried out simultaneously with the reading of the TM71 device. This allowed a direct comparison of the data from the two different instruments which is carried out later in this chapter.

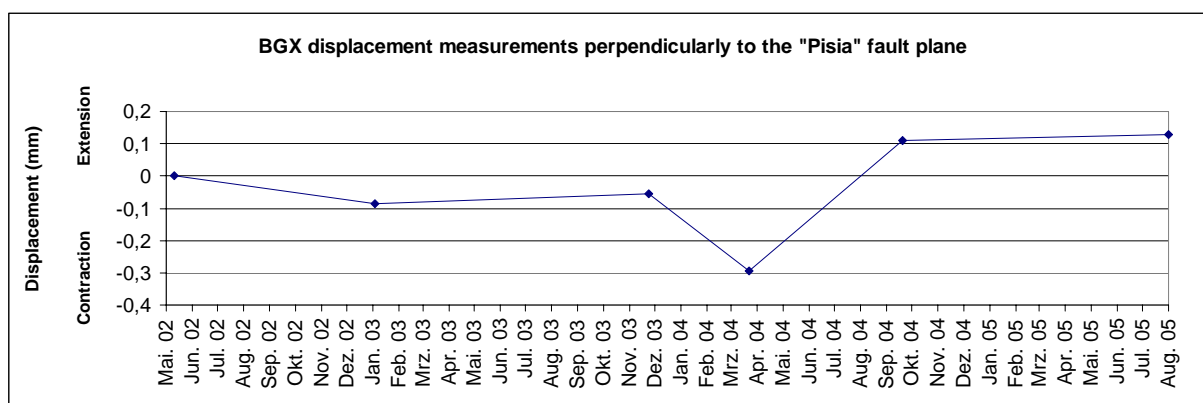


Fig. 4.21: Displacement progress at the “Pisia” monitoring site as measured by means of Bragg-Grating Extensometer (BGX).

4.4.3 Results from the Moiré extensometer (TM71) at the “Shinos A” fault monitoring site

The fault monitoring at the eastern segment of the Shinos fault zone began on the 11th of October 2002, i.e. almost 8 months later than the fault monitoring at the Pisia site. Eight readings (including the reference measurement at the beginning) were obtained at the “Shinos A” monitoring site by means of TM71 and the last reading was taken on the 1st of August 2005 (see appendix §5). The time intervals between the measurements had the same duration as the ones of the other monitoring sites because all monitoring sites were visited on the same day each time a measurement had to be taken. In view of the fact that the relative displacements recorded at the Shinos “A” monitoring site were relatively small as opposed to the displacements at the “Pisia” and “Shinos B” monitoring sites (fig. 4.25), the Moiré patterns on the TM71 indicators at the “Shinos A” monitoring site never reached a high density. Therefore, the Moiré patterns at the “Shinos A” monitoring site were always easy to read and it was not necessary to set the instrument back to zero after each reading.

After two years of monitoring, along the dip slip direction, the fault displayed, a cumulative displacement of only 0.06mm in a reverse sense of motion fig. 4.22a. In the same diagram a slight oscillation can be recognized, which cannot be clearly correlated to seasonal factors. On the contrary, the displacement along the strike slip direction fluctuates in a seasonal way (fig. 4.22b). These fluctuations have distinct turning points in March/April as well as in October-December of each year. In addition a weak but clear dextral trend was established with a rate of 0.04mm/year and the cumulative dextral displacement until the 1st of August 2005 was 0.1mm. The measurements perpendicularly to the fault plane also display a characteristic fluctuation which has distinct turning points in March/April of each year (fig. 4.22c). However there was no prevailing trend towards extension (opening) or contraction (closing) of the fault gap and practically the fault gap remained unchanged.

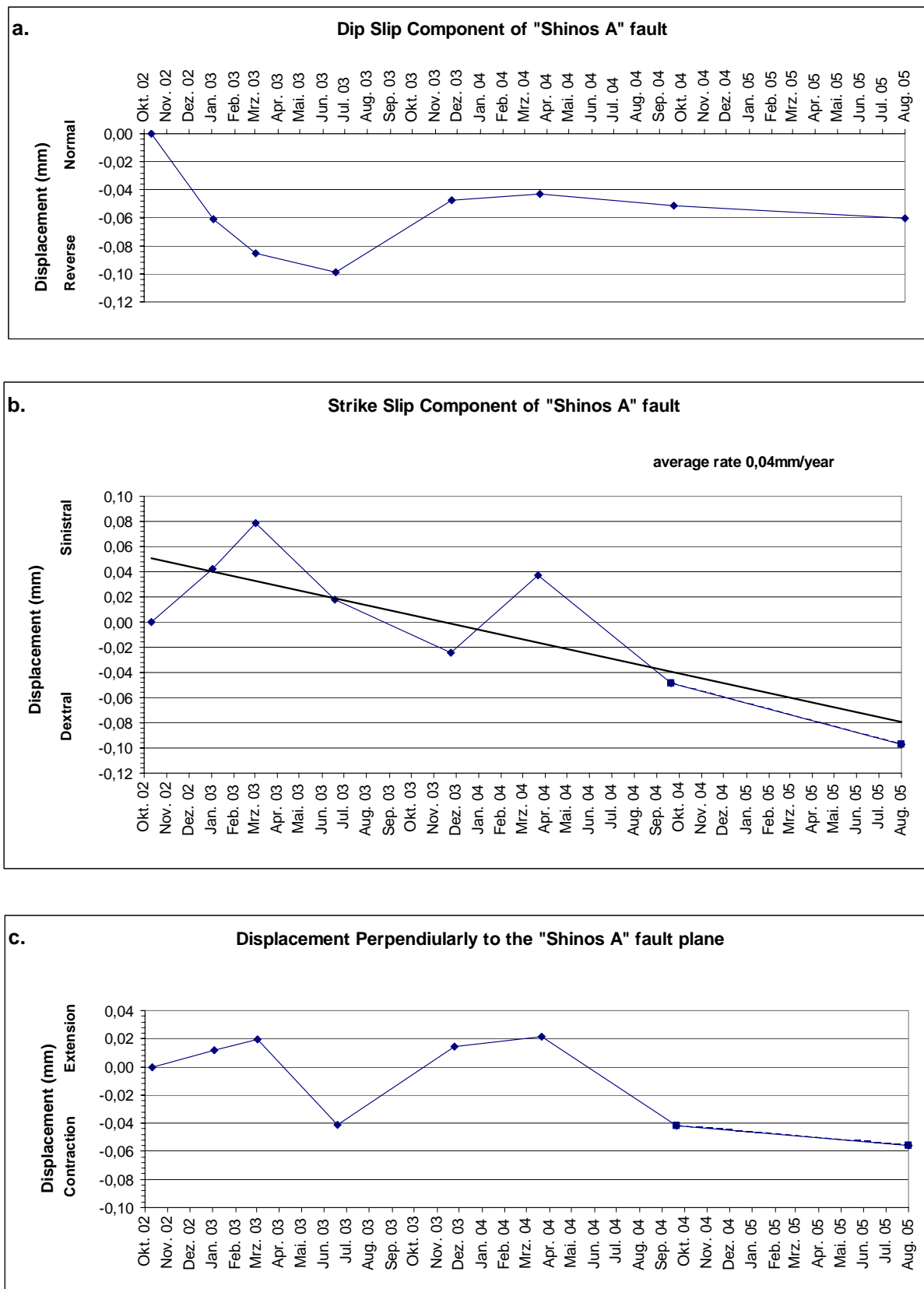


Fig. 4.22: Displacement progress at the "Shinos A" monitoring site as measured by means of Moiré extensometer (TM71 device)

4.4.4 Results from the Bragg-Grating extensometer (BGX) at the “Shinos A” fault monitoring site

At the “Shinos A” monitoring site the Bragg-Grating Extensometer was mounted perpendicularly to the fault plane in the same manner as at the “Pisia” monitoring site. The results are shown in fig. 4.23 (see also appendix §6). The fault monitoring by means of the BGX rod began on the same day as with the TM71 (11/10/02) and a total of 5 measurements were obtained. Due to the practically negligible displacements perpendicularly to the fault plane, the BGX method could not deliver any significant displacement values. The latter is also obvious when comparing the results of the BGX and the TM71 devices in paragraph 4.4.7.

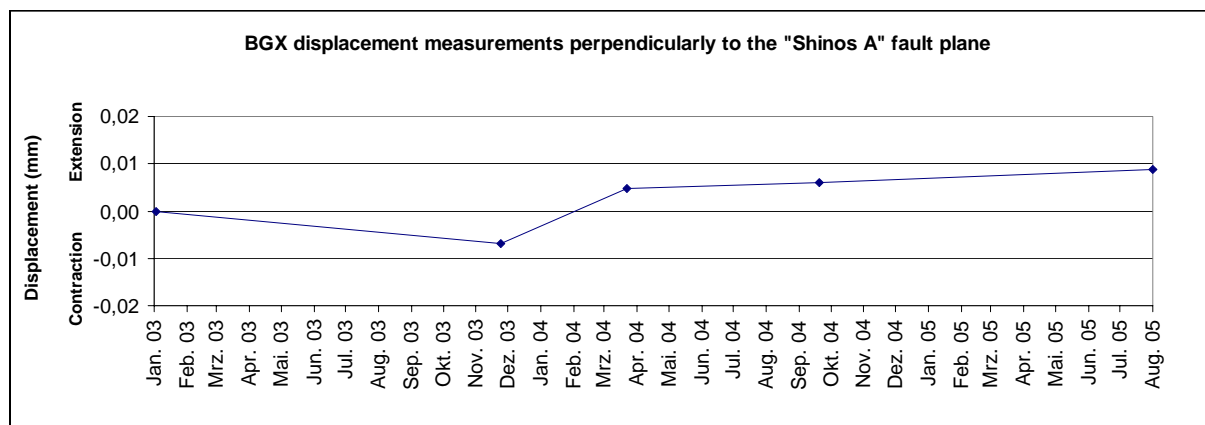


Fig. 4.23: Displacement progress at the “Shinos A” monitoring site as measured by means of Bragg-Grating Extensometer (BGX).

4.4.5 Results from the Moiré extensometer (TM71) at the “Shinos B” fault monitoring site

The fault monitoring at the “Shinos B” monitoring site began on the 5th of March 2003. Unfortunately, on the 20th of September 2004 the TM71 instrument was found damaged and a reliable reading on that date was not possible. Moreover, a further use of the TM71 device was not possible. Consequently, only a total of four measurements were obtained during a monitoring period of one year (see appendix §5). Due to the large displacements at the “Shinos B” monitoring site it was necessary to set the TM71 device back to zero after each reading in order to avoid dense and thus difficult to read Moiré patterns.

Along the dip-slip direction (fig. 4.24a) the TM71 recorded in summer of 2003 a rather large displacement of 3,84mm with a normal sense of motion. However, this displacement attenuated later on and on the 22nd of March 2004 only 0,26mm of normal displacement was

left. This implies that the large displacement in summer 2003 is probably the peak of a seasonal fluctuation and the points corresponding to March 2003 and March 2004 are the opposite peaks of this fluctuation. The strike slip component of motion displayed a very symmetric oscillation with peaks in the middle of summer and winter (fig. 4.24b). The remaining displacement after one year of monitoring is only 0.03mm in dextral direction, so practically no significant movement was observed. In the winter of 2003-2004, along the TM71 component which is perpendicular to the fault plane (fig. 4.24c), a significant extension of at least 2,6mm took place. This displacement was reduced to only 0,13mm of extension according to the measurement of the 22nd of March 2004. Here again, a seasonal fluctuation with turning points in November and in March can be postulated.

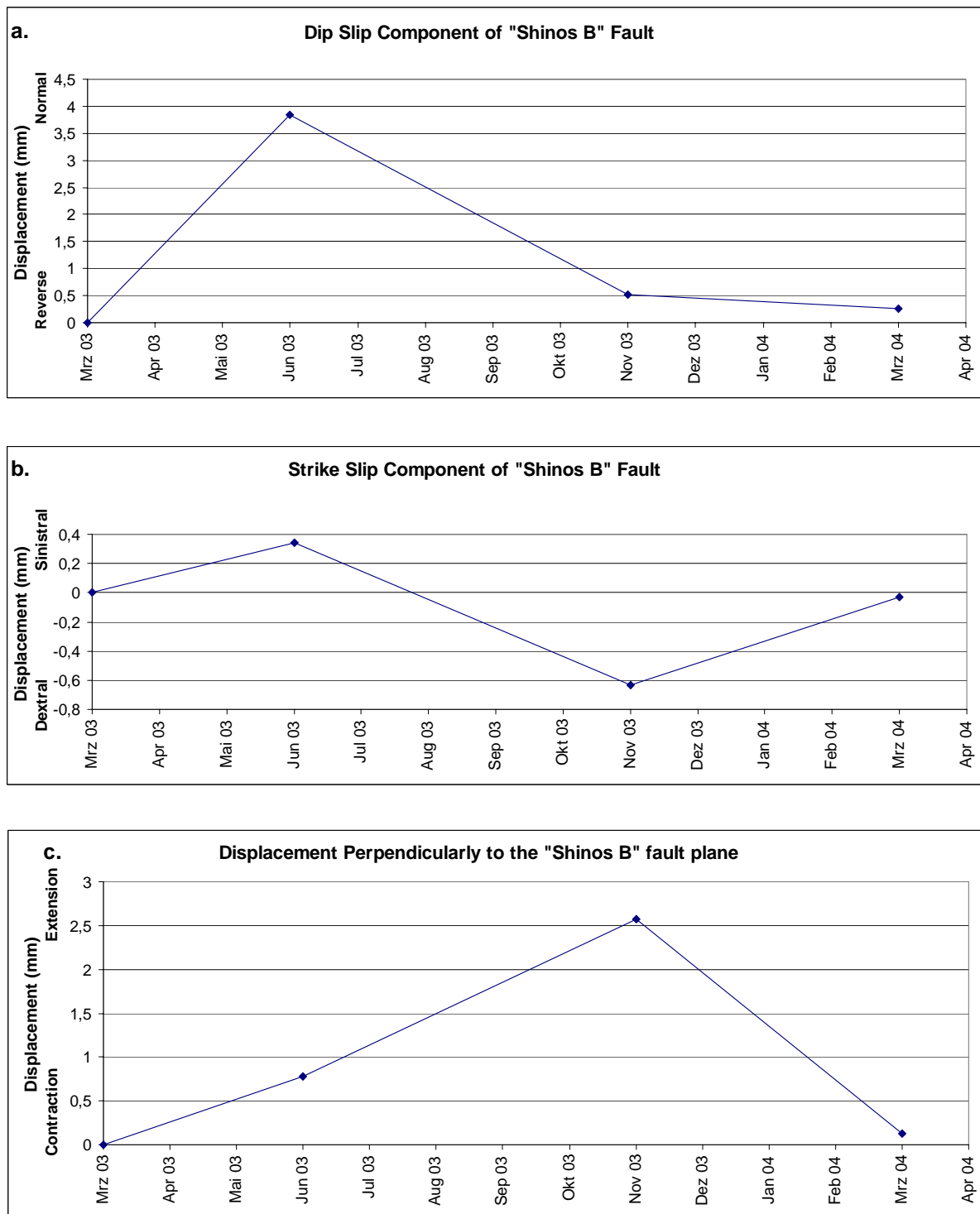


Fig. 4.24: Displacement progress at the "Shinos B" monitoring site as measured by means of Moiré extensometer (TM71 device)

4.4.6 Remarks on the observed oscillations of the displacement progress

A common characteristic of all the curves describing the fault displacements measured by means of TM71 are oscillations with a more or less seasonal character along all measurement components. At all three monitoring sites of the present study, the TM71 instruments were installed as linear bridges between the footwall and the hanging wall of the fault (see paragraph 4.3) and therefore dilatation effects of the instruments themselves could take place only along their x component. These effects along the x component are already compensated in the displacement diagrams according to the well defined formula of paragraph 4.1.2.2. Therefore the cause of the oscillations should be sought in other processes such as the response of the rock to temperature changes. Such climatically depended oscillations have also been observed by others (KOSTAK & CRUDEN. 1990, KOSTAK et al.1998, PETRO et al. 2005). KOSTAK & CRUDEN. (1990), for example, mention that temperature oscillations of 20°C in limestone and sandstone correspond to displacements with amplitude up to 2mm.

In the present study, by controlling the indications of the TM71 devices several times on each day of measurement, it was found that the daily fluctuations of the temperature had no effect on the measurements. In addition the indications of the TM71 were controlled in intervals of 10-14days during each fieldwork/reading campaign in order to verify the reliability and the stability of the instruments. During these controls at the three monitoring sites, no significant displacement was measured. Hence, it was confirmed that the fault displacements at the monitoring sites were taking place at very slow rates and that no short-term fluctuations were occurring. Consequently, the volumetric response of the rocks to temperature changes had a seasonal character.

From the above observations it can be concluded that in cases of fault monitoring by means of in-situ installed instruments, long periods of monitoring are essential. In fact, the longer the monitoring period, the more reliable the established trends will be. Such long term monitoring activities help to understand the seasonal effects and allow to distinguish any displacement trends. Most characteristic are the examples of the “Pisia” and “Shinos A” monitoring sites where after two years of monitoring the seasonal fluctuations and any actual displacement trends are visible. In the case of the “Shinos B” monitoring site, the extent and the character of the fluctuations is relatively unclear due to the relatively short time of monitoring (only one year).

As far as the instrument itself (TM71) is concerned, potential inhomogeneities within the metal parts and constructional asymmetries could cause a differential deformation in response to temperature also along the y and z components. Such effects might be partly responsible for the profound fluctuations observed in the displacement diagrams of the “Shinos B” monitoring site (fig. 4.24 and fig. 4.25). At this monitoring site the length of the instrument bridge, that is the length of the steel bars and the instrument itself, was 1055mm. Compared to the TM71 bridges at the two other monitoring sites, the TM71 bridge at the “Shinos B” monitoring site was almost three times longer and thus more susceptible to bending due to any inhomogeneous dilatations of the steel bars.

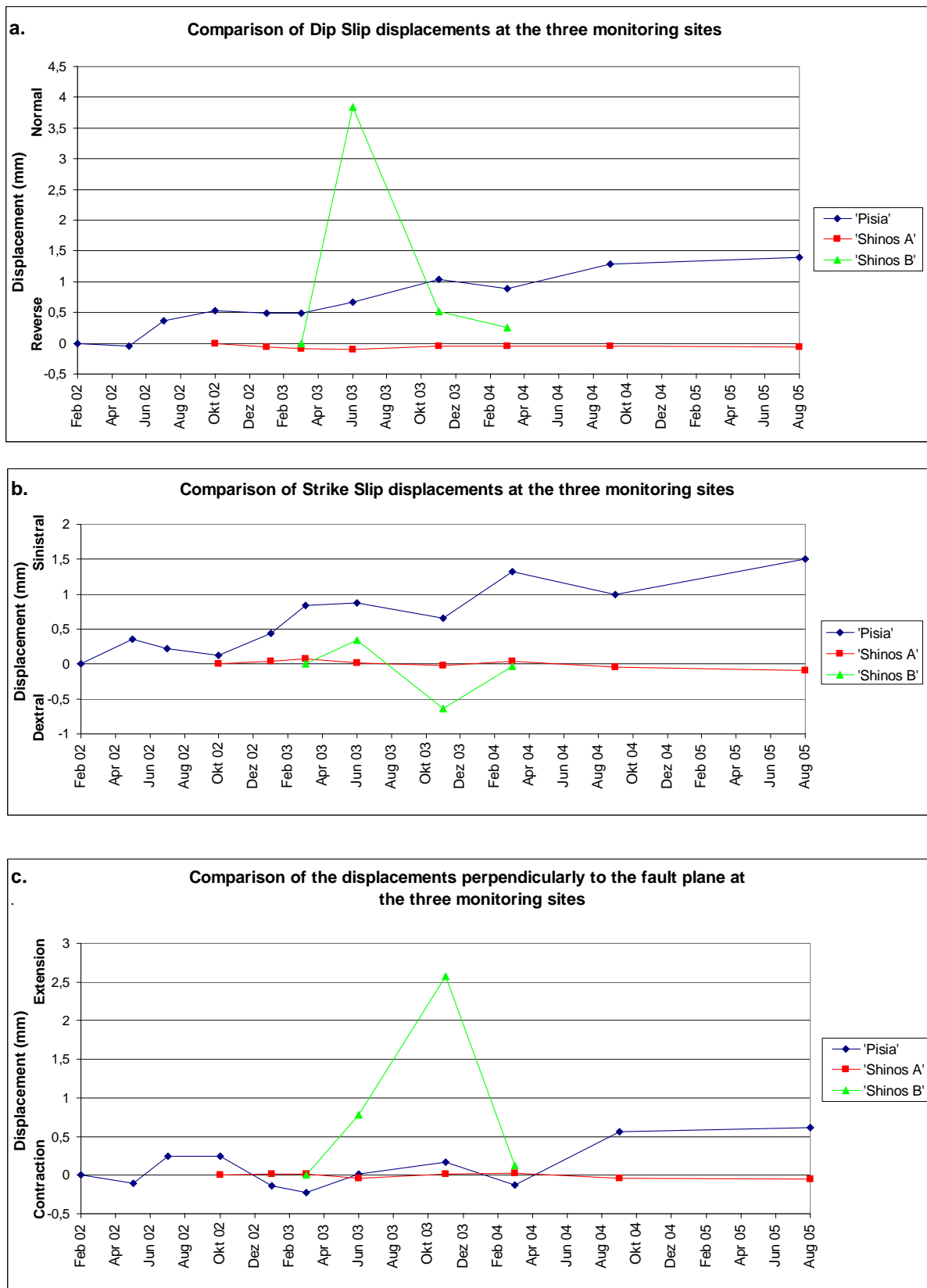


Fig. 4.25: Comparison of the displacement progress along each measuring component at the at the three monitoring sites as measured by means of Moiré extensometer (TM71 device).

4.4.7 Comparison of the results from the Moiré and Bragg-Grating extensometers

One of the aims of the present study was to compare the relatively modern technique of the Bragg-Grating extensometers (BGX) with the well established displacement monitoring technique of the TM71 devices. As already mentioned, the configuration of the BGX instruments in the present study allowed a 1-dimensional displacement monitoring. The BGX rods at the “Pisia” and “Shinos A” monitoring sites measured the displacement in the direction which was perpendicular to the fault planes. It was therefore possible to compare the BGX results with the respective results TM71s which were installed at the same locations.

The diagrams in figures 4.26 and 4.27 depict the comparison of the two types of instruments at the “Pisia” and “Shinos A” monitoring sites respectively. In each diagram, both the BGX and TM71 displacement curves begin at zero so that a comparison is possible. Simultaneously with each BGX measurement, a reading of the TM71 indication was also obtained. Unfortunately, the number of BGX readings was restricted because the readout unit, necessary for obtaining them, was not available for each fieldwork/measurement campaign.

As far as the “Pisia” monitoring site is concerned (fig. 4.26) it is obvious that the curves of the TM71 and the BGX measurements do not coincide. Nonetheless, between each consecutive measurement points, both curves show the same direction of displacement. This means that when the TM71 device indicated a contraction, the BGX rod indicated a contraction as well and this applies also in the case of extensional movements (opening of the fault gap). By examining the diagram of fig. 4.26, it becomes apparent that since the end of November 2003 the curves are practically parallel to each other i.e. the recorded relative displacements since then have the same amount and the same direction. The disparity between the two displacement curves is mainly located between their second and third measurement points and is related to technical issues which concerned the BGX measurements. More precisely, up to the second measurement by means of BGX, the read out unit and the connecting optic fibre cables were different to those used for the rest of the measurements. Apparently, this inconsistency induced the significant deviation of the BGX curve from the TM71 curve at the third measurement (Nov. 2003). Another error inducing factor may be the measurement of the temperature of the BGX rod. It was practically impossible to measure the temperature directly on the sensor area of the BGX rod because the rod was within the protective PVC tube (see fig. 4.11). Instead, the necessary temperature compensation for the each BGX value was carried out by using the respective temperature indication of the TM71 device, which was

situated immediately next to the BGX rod. This compromise might also be responsible for a part of the discrepancy between the BGX and TM71 displacement curves.

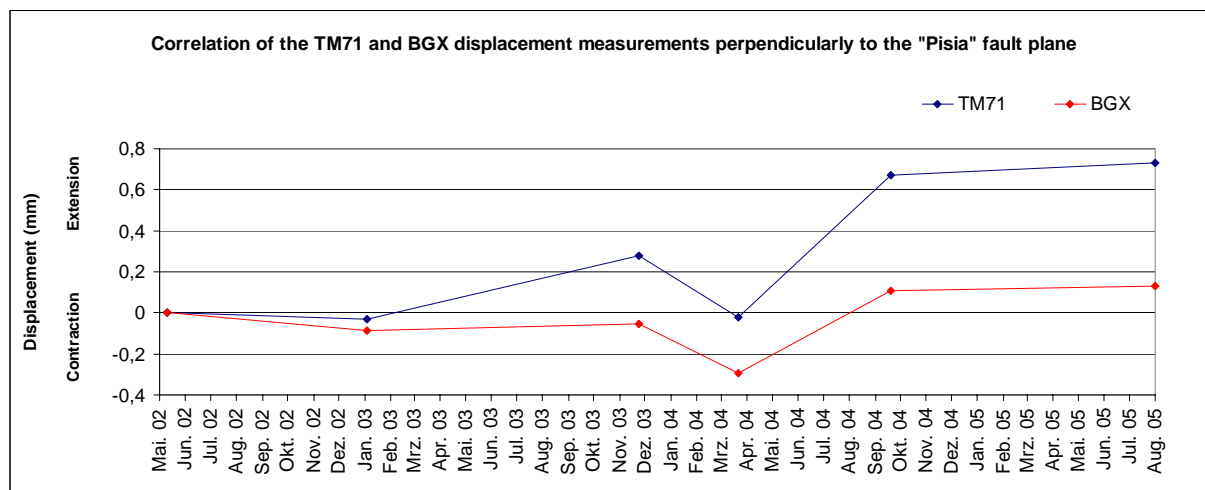


Fig. 4.26: Comparison between the displacement measurements obtained by means of the Moiré extensometer (TM71) and the Bragg-Grating Extensometer (BGX) at the “Pisia” monitoring site (component perpendicular to the fault plane).

As mentioned above, in the diagram of fig. 4.26 the measurement of November 2003 the BGX and the TM71 curve are progressing practically parallel to each other. Hence, since November 2003 both instrument types indicate the same amount and the same direction of relative displacements. Evidently, the consistency and the reliability of the BGX results were improved by the fact that for the measurement of November 2003 and for the following measurements the same read-out unit and connecting optic fibre cables were always used.

The curves in fig. 4.27 describe the displacement progress perpendicularly to the fault plane as registered by the TM71 device and the accompanying BGX rod at the “Shinos A” monitoring site. It is apparent that the two curves do not exhibit any convincing similarities. Only some segments of the BGX displacement curve show similarities in the direction of motion with the TM71 curve but the amounts of displacements do not coincide.

The potential reasons for this unconformity between the two instruments might be several. Most plausible is, however, the fact that the registered displacements are marginally greater than the resolution of the TM71 and the resolution of the BGX rod. As far as the resolution of the BGX is concerned, the use of a relatively long connecting cable (2,5m long) between the read-out unit and the rod at this monitoring site was proved to be disadvantageous. The use of this longer cable was necessary due to the position of the BGX rod high above the ground.

Such a long cable was susceptible to trembling already in the case of a slight wind and this induced noise into the measured signal which reduced the resolution of the BGX rod to approximately 0,03mm. Other sources of error included uncertainties concerning the temperature measurement and the condition of the connector on the BGX rod. The latter was frequently found to be directly exposed to open air and rain as the protective cap was repeatedly missing.

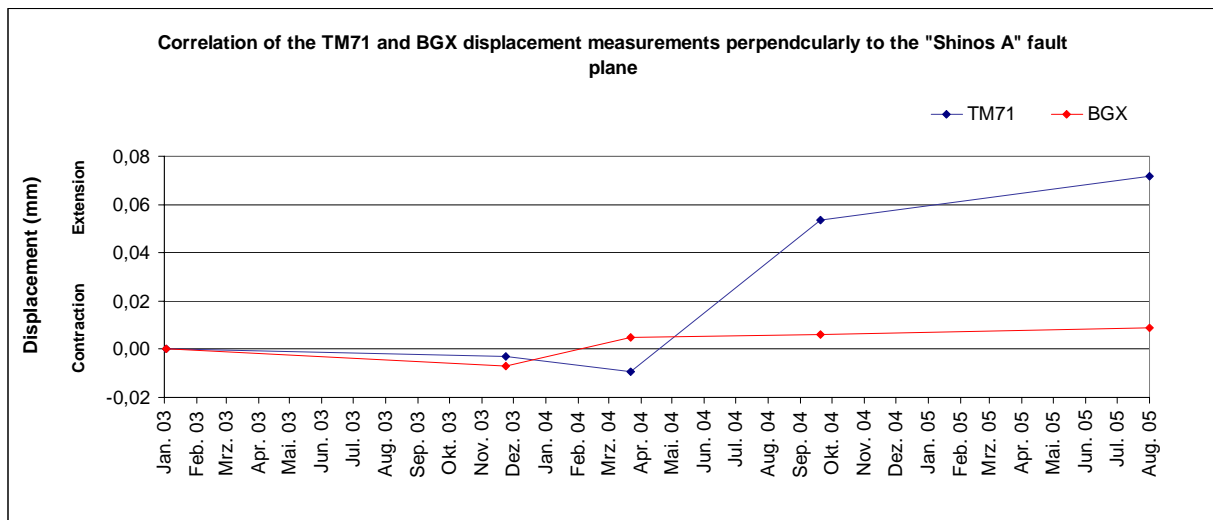


Fig. 4.27: Comparison between the displacement measurements obtained by means of the Moiré extensometer (TM71) and the Bragg-Grating Extensometer (BGX) at the “Pisia” monitoring site (component perpendicular to the fault plane)

It is evident that, in the case of the “Shinos A” monitoring site, the negligible amounts of displacement perpendicularly to the fault plane render the performance of the instruments questionable and therefore inhibit a correlation between the TM71 and BGX results. Presumably, a reliable comparison between the two instrument types at the “Shinos A” monitoring site would have been possible after a longer monitoring period (several years), which would allow the cumulative displacement to reach higher, more discernible levels.

In conclusion, the application of the Bragg-Grating Extensometer at the Pisia monitoring site proved that such an instrument can be used successfully to measure displacements of at least 0.1mm perpendicularly to a fault plane. Important prerequisites are a consistent measurement of the sensor temperature and the use of the same equipment (readout unit and connecting optic fibre cables) throughout the monitoring period. The use of long, instable fibre optic cables for the connection of the BGX rod to the readout unit can be an additional source of error.

In general, the experience which was gained by the application of the Bragg-Grating Extensometer at the “Pisia” and “Shinos A” monitoring sites showed that the BGX method is not as sensitive as the TM71 method. In addition, concerning the readout procedure itself, there are more error-inducing factors which can affect the performance of the Bragg-Grating extensometer (BGX) in comparison with the Moiré extensometer (TM71).

4.5 Kinematic evaluation and interpretation of the fault monitoring results

4.5.1 The fault displacement regime at the “Pisia” monitoring site

As already described, the trend of the normal dip-slip motion at the “Pisia” monitoring site, according to the TM71 results, has an average rate of 0,44mm/year (fig. 4.20a). At the “Pisia” monitoring site the fault is dipping to the north and the fact that the fault displacement has a normal character is in accordance with the roughly N-S directed extensional tectonic regime which dominates within the Gulf of Corinth. This rate of normal displacement concerns the local behaviour of the fault at the “Pisia” monitoring site. Nevertheless, if it is taken into consideration that the “Pisia” monitoring site is located in the middle of the Pisias fault zone and on a major fault segment then it can be assumed that the normal-slip rate, as measured by the TM71, is representative for the main part of the Pisias fault zone. Conversely, at the tips of the Pisias fault zone, where the escarpment height attenuates, the displacement rate is expected to be lower. The co-seismic displacement of the 1981 events was also lower at the tips of the Pisias fault zone, whereas the greatest co-seismic throws occurred in the central parts of the fault zone (JACKSON et al. 1982).

At the “Pisia” monitoring site, the annual rate of normal displacement, as measured by means of TM71, is representative for a period of almost 3.5years i.e. for a very short period compared to the duration of tectonic processes. ROBERTS et al. (1993) estimated the slip rate at exactly the same location for the last 350ka based on Uranium-series dating methods and morphological observations. The long term slip rate, according to the aforementioned author, is 0.14-0.37mm/year. Apparently, this estimation is of the same order of magnitude with the slip rate measured by the TM71 within 3,5years (0.44mm/year). The fact that the slip rate measured in the present study is 0.07mm/year higher than the upper limit of the long term slip rate suggested by ROBERTS et al. (1993) implies that in the present state the fault, at least locally at Pisias, is probably moving faster than the average of the last 350ka.

Concerning the displacement along the strike slip direction, a relatively strong sinistral trend of 0.40mm/year was recorded (fig. 4.20b). The left lateral character of this trend is incompatible with the local striations on the fault plane, and the co-seismic displacements of the 1981 earthquake events, which both have a normal-slip character at the “Pisia” monitoring site (MOREWOOD & ROBERTS 2001, JACKSON et al. 1982).

A plausible explanation for the present sinistral trend at the “Pisia” monitoring site might be related to particular fault kinematics that occur at the termination of fault segments or faults. As seen in fig. 4.6 the “Pisia” monitoring site is located at the eastern end of a north dipping fault segment. In such cases, apart from the dip-slip, a lateral motion of the hanging wall is expected in a converging sense towards the centre of the fault segment as described in fig.4.28 (MOREWOOD & ROBERTS 1999, MOREWOOD & ROBERTS 2001, ROBERTS 1996a,b). Furthermore, from the model of fig.4.28 it emanates that larger dip-slip displacements might be taking place in the central parts of the fault segment at Pisias.

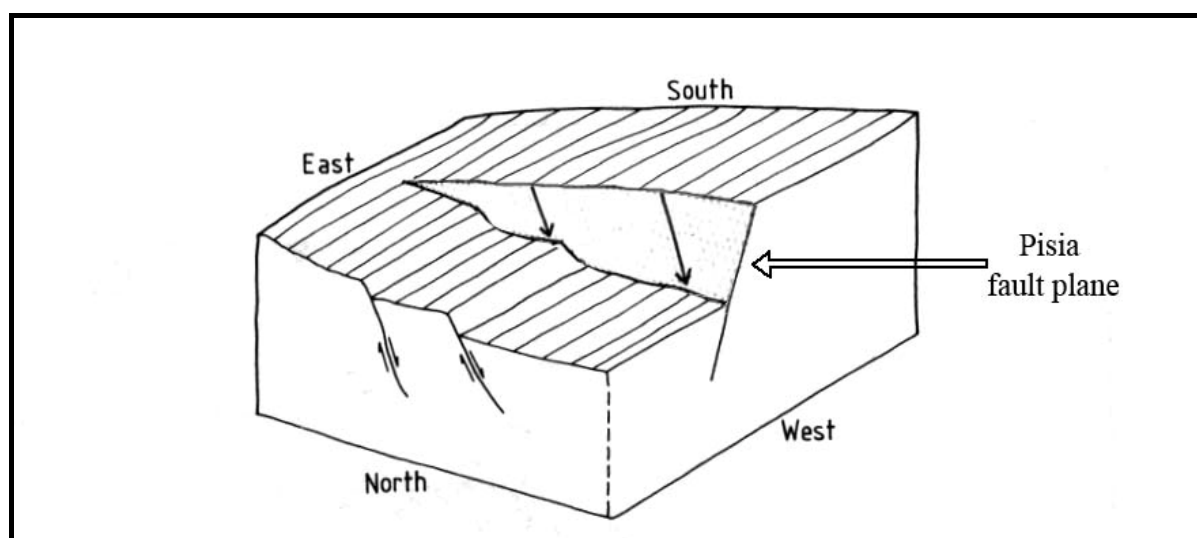


Fig. 4.28: A schematic describing how a sinistral component of motion is possible during interseismic periods at the the “Pisia” monitoring site (located at the eastern end of a north dipping fault segment) (adapted from KING et al 1985).

Strong earthquakes (e.g. the 1981 earthquakes) can break segment boundaries (ROBERTS 1996b), activate more than one consecutive segments as a whole and induce dip-slip along the entire fault length. During the interseismic periods, however, the fault segments could be individually active and the areas between them might be functioning as conservative barriers (equivalent to material-bridges) (fig.4.29). In such cases, lateral motions are expected at their tips like the ones schematically shown in fig.4.28.

The aforementioned model explains the left lateral trend registered by the TM71 at the “Pisia” monitoring site but also the dip slip co-seismic motions of the 1981 events and the dip-slip striations which were formed in depth by previous earthquakes.

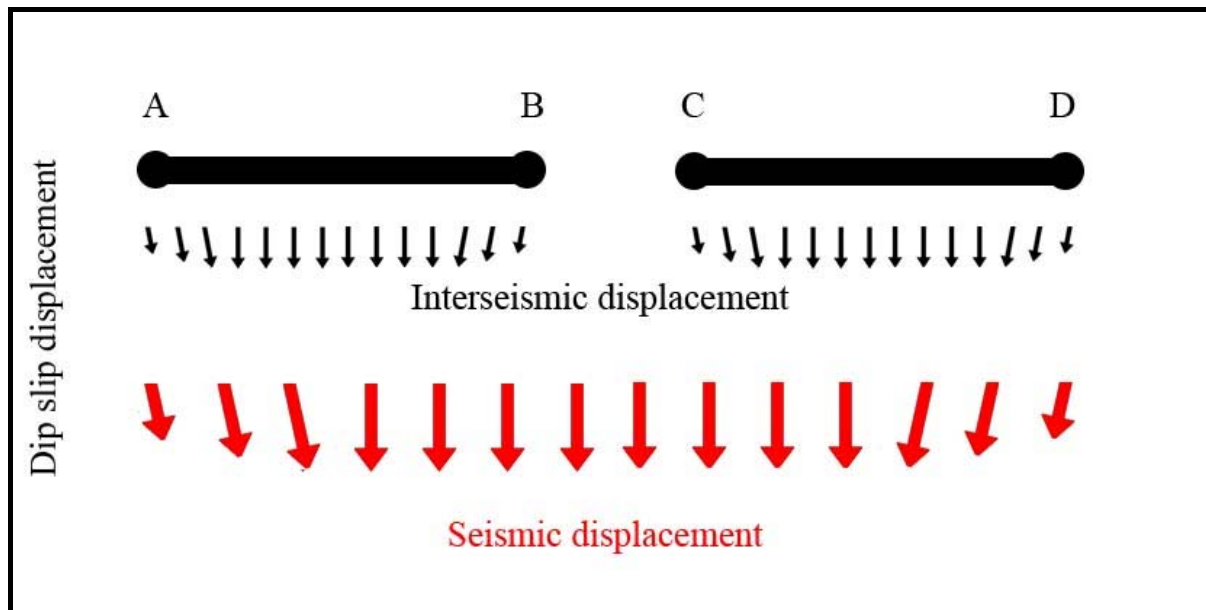


Fig.4.29: Schematic description of the difference between co-seismic and interseismic fault slip (the arrows show the direction of slip on the fault plane). The fault A-D consists of two fault segments A-B and C-D. During interseismic periods the area B-C functions as a barrier (equivalent to a material-bridge) and near the points B and C lateral motions occur according to fig.4.28. In case of an earthquake the area B-C is also broken, the entire fault (A-D) is activated and dip slip movements occur in the areas round the points B and C.

However, the short-term character of the measurements i.e. the time factor should not be neglected. Short term movements or trends do not necessarily have to agree with the long term trends (thousands of years). During the three years of observation the established trend of the strike slip component is clearly left-lateral but on a longer term basis it might be compensated by dextral movements.

Finally, as far as the displacement component perpendicularly to the fault plane is concerned, the TM71 as well as the BGX measurements indicate that the fault gap is slightly extending. The rate of extension (opening of the fault gap) is 0.18mm/year according to the more reliable measurements of the TM71 device (fig.4.20c) and is rather low and insignificant compared to the rate along the other two components. The fact that the fault gap is opening is conformable to the N-S extensional regime of the Gulf of Corinth.

4.5.2 The fault displacement regime at the “Shinos A” monitoring site

The fault displacements registered by means of the TM71 device at the “Shinos A” monitoring site are presented in the diagrams of fig. 4.22. A common characteristic of the displacements along all three components of motion is that they are substantially lower (by a factor of 10), compared to the ones recorded at the “Pisia” monitoring site (fig. 4.25c). The

lower amounts of displacement indicate that, at least during the period of monitoring (11.10.2002 - 01.08.05), the local tectonic activity at the “Shinos A” monitoring site was significantly weaker than that at the “Pisia” monitoring site.

The lower amount of displacements at the “Shinos A” monitoring site is likely owing to the fact that the monitoring site is situated approximately 100m to the south of the main Shinos fault on a fault plane which is oblique to the main Shinos fault (fig.4.30). The main Shinos fault in the area has a long term normal slip rate of 1.2-2.3mm/year according to COLLIER et al.(1998) and was activated by the 1981 earthquake events (JACKSON et al. 1982) and, therefore it can be considered as currently active. The displacements measured at the “Shinos A” monitoring site are probably a side effect of the stronger movement which is potentially taking place on the main fault. Unfortunately, a reliable installation of monitoring instruments directly on the main Shinos fault in the area was not possible due to the lack of locations which would provide a stable instrument fixation.

It has to be underlined that the registered displacements at the “Shinos A” monitoring site are very low and thus comparable to the accuracy of the TM71 (0.03mm according to STEMBERK et al. 2003) and therefore the monitoring results are not completely reliable for a secure tectonic interpretation. Nevertheless, an interpretation will be attempted in the following paragraphs.

Regarding the TM71 component along the dip-slip direction, the curve in fig.4.22a begins with a reverse motion and evolves further into a sinusoidal form i.e. no further trend is recognizable. Therefore, it can be stated that the dip slip displacement remains stable after the January of 2003.

The clear reverse movement indicated by the beginning of the curve is discrepant with the stress regime of the Gulf of Alkyonides. More precisely, the fault of the “Shinos A” monitoring site is dipping towards the NW and since the extension at the Perachora region is NNW-SSE directed (paragraph 4.2.4) a normal displacement on the fault would have been expected. In addition, morphologically and stratigraphically, it is indisputable that the fault is normal. Reverse motions were also indicated by the TM71 at the “Pisia” monitoring site (fig.4.20a) but these were clearly part of the climatically induced fluctuations. In the case of “Shinos A” monitoring site no regular seasonal effects can be recognized along the curve of

the dip-slip direction. Consequently, it is not certain whether the reverse movement at the beginning of the monitoring period is induced by climatic factors (e.g. temperature), technical factors (instrument related) or if it is indeed related to endogenic processes.

If an actual reverse movement took place at the beginning of the monitoring period then it was likely the result of local rotations about sub-horizontal axes within the hanging wall of the monitored fault. Such rotations are described in fig. 4.30 and are expected due to the interaction with the main active fault immediately to the north.

In respect to the lateral component of displacement at the “Shinos A” monitoring site (fig. 4.22b), it has been already mentioned that the respective curve displays a clear undulating character related to seasonal temperature effects. Nevertheless, in addition to the seasonal fluctuations and despite the very small amount of displacements a clear dextral trend of 0.04mm/year is obvious. This overall dextral behaviour could be induced by the previously assumed local rotations but is most probably a direct result of the regional NNW-SSE directed extension on the monitored fault as shown in (fig. 4.30). The monitored fault strikes, namely, towards the NNE i.e. obliquely to the NNW-SSE directed extension and consequently a substantial lateral movement of dextral sense is plausible.

Along the third component of measurement by means of TM71 at the “Shinos A” monitoring site, i.e. perpendicularly to the fault plane, no trend was established during the monitoring period. The respective displacement curve of fig. 4.22c is only characterised by seasonal, and systematic fluctuations. Consequently, it is evident that the fault gap between the hanging wall and the footwall remained practically stable during the monitoring period. Firstly, this result indicates once again that the tectonic activity is significantly lower at the “Shinos A” monitoring site and secondly it does not provide with significant information about the character of the local tectonic processes.

In general, the displacements at the “Shinos A” monitoring site are comparably too small to be safely used for conclusions concerning the local fault kinematics (fig. 4.25). Taking into account the progress of the displacements during the approximately 3 years of monitoring it is obvious that over a longer monitoring period of 5 to 10 years or even longer, the accumulated displacements would show clearer trends and would predominate over the climatically induced measurement effects.

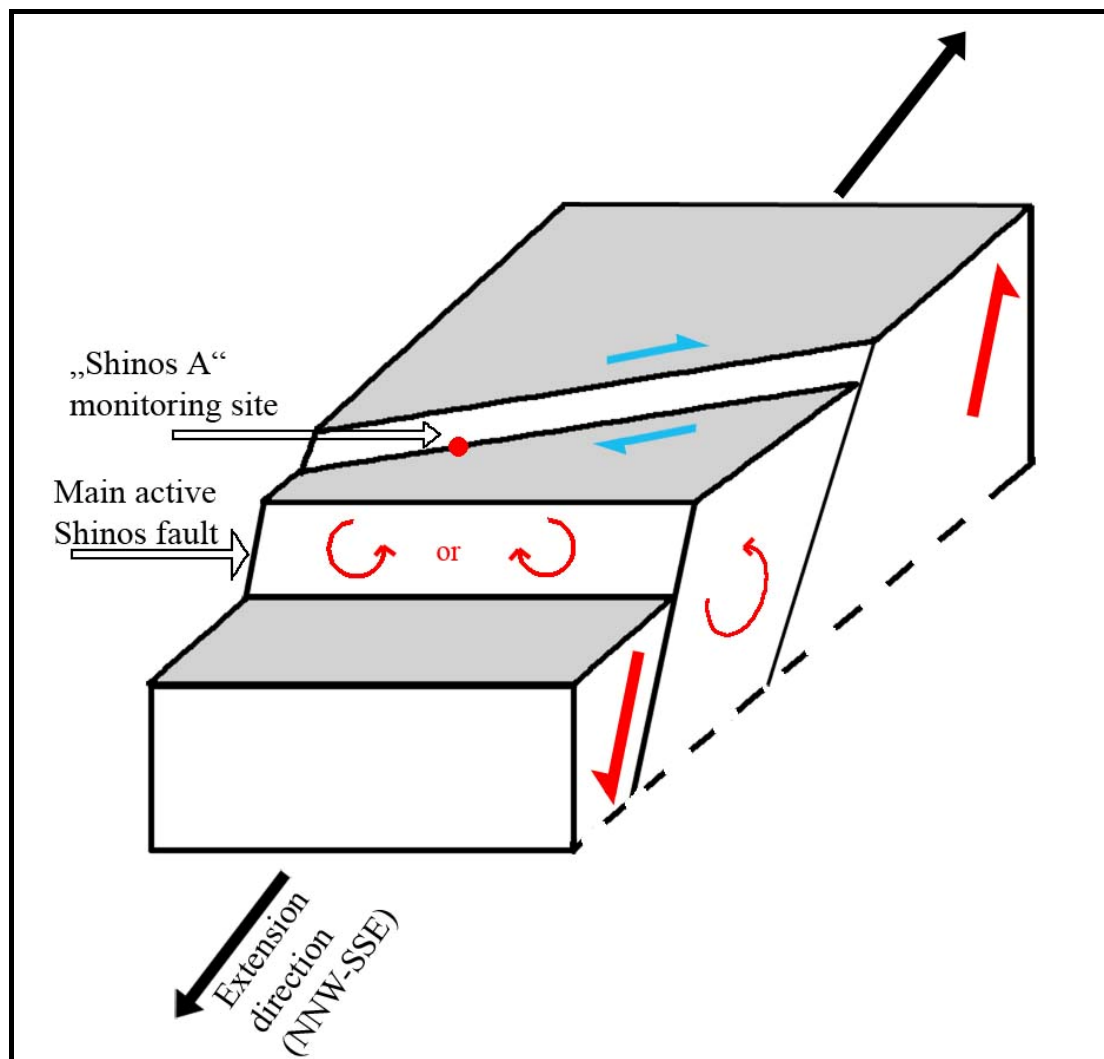


Fig. 4.30: Schematic description of the potential rotations within the hanging wall of the “Shinos A” fault due to its interaction with the main Shinos fault (red circles). The diagram also depicts the mechanism inducing the overall dextral component on the “Shinos A” monitoring site (blue arrows).

4.5.3 The fault displacement regime at the “Shinos B” monitoring site

The “Shinos B” monitoring site, as already mentioned, delivered useful data from the 5th of March 2003 to the 22nd of March 2004. During this one year of displacement monitoring, four readings were taken including the reference reading at the beginning. Due to the short duration of monitoring and the restricted number of measurements (fig. 4.24) it is not possible to define reliable annual displacement rates along the three measurement components. Nevertheless, it is possible to postulate about the annual trend of the movements by considering the amount of residual displacement at the end of the monitoring period which lasted one year (from March 2003 to March 2004).

The main characteristic of the curve describing the displacement along the dip-slip direction (fig. 4.24a) is the normal displacement of 3.8mm measured in June 2003. In March 2004, however, the normal displacement had been reduced to only 0.26mm, thus the peak of June 2003 belongs probably to a seasonal fluctuation. The residual normal displacement of 0.26mm at the end of the one year long observation is an indication that the fault displays an overall normal-slip and is in the same order of magnitude with the normal slip rate at the “Pisia” monitoring site. Normal slip on the ca. E-W orientated monitored fault is an expected consequence of the NNW-SSW orientated extension that is taking place at the Perachora region.

Also the residual displacement perpendicularly to the fault plane at the end of the monitoring period is compatible with the extensional regime of the Perachora region. In diagram c of fig. 4.24 it is obvious that at the end of the annual fluctuation, the fault gap was wider by 0.13mm.

Along the strike slip component of measurement, there was no substantial residual displacement at the end of the monitoring period (fig. 4.24b). A dextral displacement of only 0,03mm remained after a clear annual fluctuation. Taking into consideration the small amount of the remaining displacement and the accuracy of the TM71 device which is 0.03mm (STEMBERK et al. 2003) it is apparent that practically no displacement trend was established along the strike slip direction at the “Shinos B” monitoring site.

Apparently, the tectonic activity measured at the “Shinos B” monitoring site represents only a small part of the movement that is taking place on the Shinos fault zone in this area. Despite the fact that the fault plane at the “Shinos B” site was activated by the earthquakes of 1981 the current tectonic activity is obviously taking place along other fault planes. For example in fig. 4.6 it can be seen that immediately to the north of the “Shinos B” monitoring site, other fault segments belonging to the Shinos fault zone exist. In fact, the main Shinos fault to the north of the monitoring site (see fig. 4.32) exhibits fresh fault planes within soft rocks such as alluvial deposits and weathered ophiolites. Some of these fault planes demonstrate striations with a substantial lateral character. The following features indicate that these are apparently long-term motions. Firstly, at their crossing with the main fault, the valleys of the local torrential streams are deflected in a dextral sense. Secondly, at the same locations, the valleys of the torrential streams have unusually large depths which can be attributed to processes analogous to the formation of pull-apart structures (see fig. 4.31).

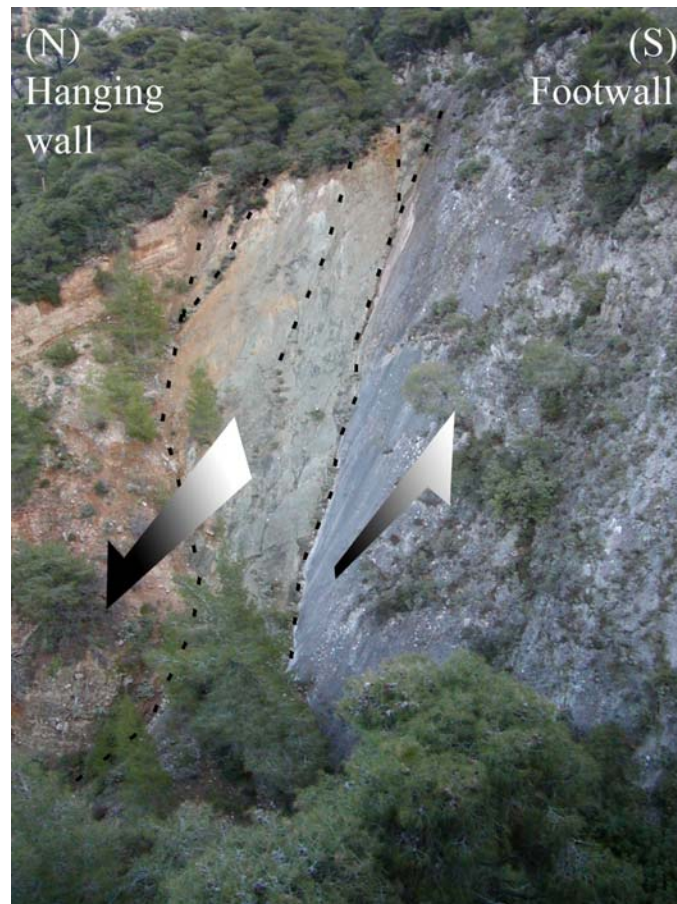


Fig. 4.31: To the north of the “Shinos B” monitoring site the main Shinos fault has a dip-slip character whereas the secondary faults in the immediate hanging wall are characterised by a substantial dextral component. The latter is probably responsible for a pull-apart effect which causes the torrential valley to become wider and deeper at that point.

Apart from tectonic processes, the normal slip and especially opening of the fault gap at the “Shinos B” monitoring site might also be related to gravity and rock relaxation/loosening processes. More precisely the monitored fault is situated at the top of the Shinos fault escarpment and very near to its edge (some tenths of meters). Taking into account that the Shinos fault escarpment is steep and approximately 200m high at this location, it is possible that monitored fault plane functions as a joint which is expanding under the effect of gravity, rock disintegration and lack of support towards the free escarpment face (fig. 4.32).

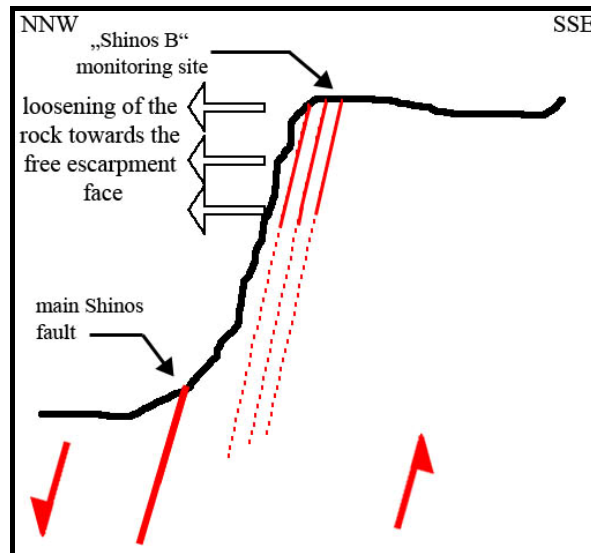


Fig. 4.32: Schematic description of the potential loosening of the rock mass and expansion of the fault gap at the “Shinos B” monitoring site due to the effects of gravity, rock disintegration and lack of support towards the free escarpment face.

4.6 Correlation between the monitored displacements and the local seismicity

In the preceding chapters, the effort was concentrated on the analysis and the kinematic interpretation of the measured displacements and displacement trends. The Gulf of Corinth is, however, seismically active and consequently the question that arises is whether the monitored displacements are directly induced by earthquakes or if they occur independently of the seismic activity.

In order to investigate the potential dependence of the recorded displacements on the local seismicity, the seismic data concerning the Perachora region for the period of monitoring, were extracted from the seismic catalogue of Greece (NATIONAL OBSERVATORY OF ATHENS 2005). The seismicity was investigated over a wider area extending between the latitudes of 38.4° and 37.7° and the longitudes 22.7° and 23.4° . In this way the monitored faults as well as the entire graben-horst system of the Gulf of Alkyonides and the Perachora peninsula were included in the selected area (fig. 4.33). Unfortunately, the seismic catalogue does not include the focal mechanisms and only the date, time, location, magnitude and focal depth are given. As far as the focal depths were concerned, only the earthquakes that occurred within the upper 15km of the crust were taken into consideration. This discrimination was based on the estimation of JACKSON et al. (1982), KING et al. (1985) and ROBERTS & GAWTHORPE (1995) that the faults of the eastern Gulf of Corinth reach down to the depth of 15km where the transition from ductile to brittle conditions begins. Deeper earthquakes represent other processes and it is rather improbable that they can affect the behaviour of the faults on the surface.

The earthquakes that fulfilled the foregoing criteria are listed in table 4.1. As opposed to the strong earthquakes of 1981 which caused extensive surface ruptures, the ones that occurred during the monitoring period had substantially lower magnitudes. The average magnitude of the 153 events in table 4.1 is 2.5 and none of them can be characterized as a strong event. The activity belongs to the regular microseismicity of the area. As far as the distribution in time is concerned, it was possible to distinguish a higher activity in June 2004 as seen in fig. 4.34. This activity was concentrated on the north-eastern part of the Gulf of Alkyonides offshore as well as onshore i.e. it was not hosted within the monitored faults.

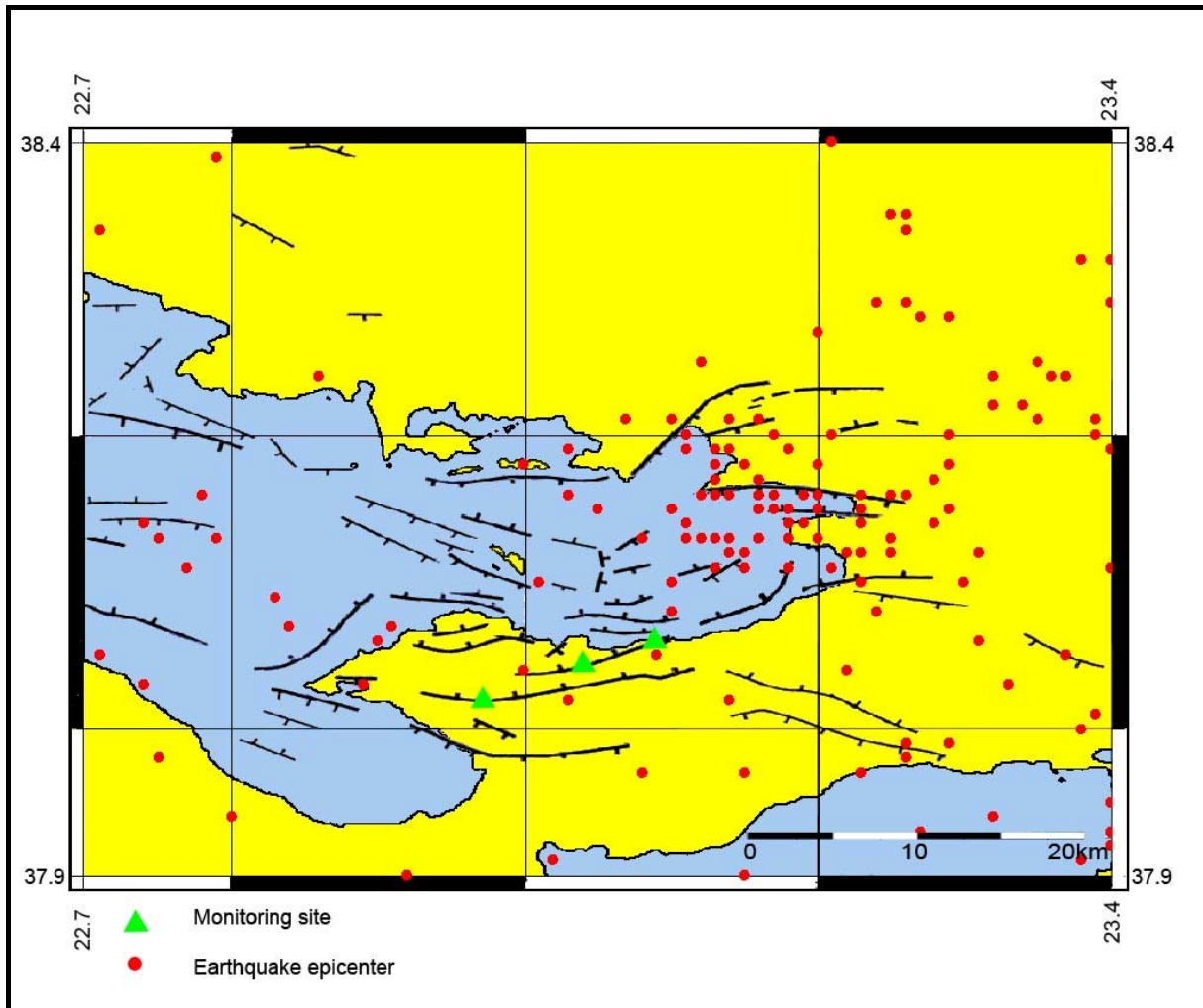


Fig. 4.33: Earthquake epicenters in the Gulf of Alkyonides area during the fault monitoring period

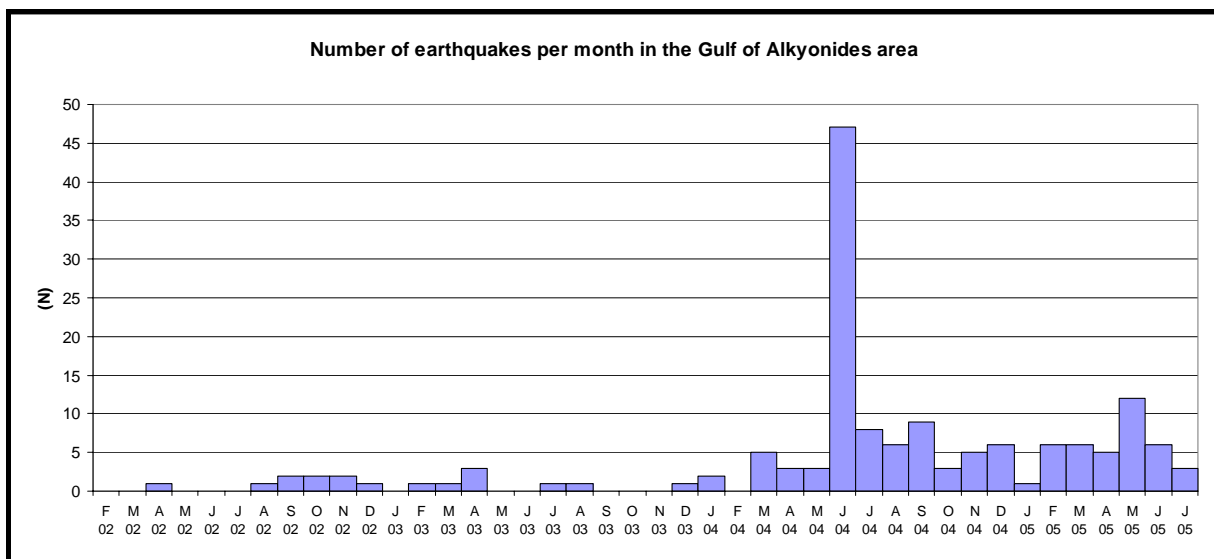


Fig. 4.34: Frequency of earthquakes per month in the Gulf of Alkyonides area.

In general, the displacement curves in fig. 4.25 display no abrupt characteristic in the summer of 2004 which could indicate a direct relation to the intense microearthquake activity of June 2004. Only perpendicularly to the fault plane at the “Pisia” monitoring site there is a slight shift which indicates a stronger opening motion of the fault gap between the measurement of March and September 2004 (fig. 4.20c). For the same period of time, however, the displacement progress along the strike slip and the dip slip components at the “Pisia” monitoring site does not seem to be influenced by the microearthquake activity of June 2004 and has a similar character with the displacement progress of summer 2003. Due to the temporal coincidence of the acceleration of the fault opening trend with the increased frequency of microearthquakes in June 2004, the former might plausibly be a result of the latter. Nevertheless, the acceleration of the fault opening motion might also be a result of climatic effects on the measurement or of other unknown factors. Unfortunately, no other exaltation of microseismicity took place during the monitoring period and therefore there was no opportunity to verify whether there is a relation between fault displacements and increased microseismicity.

Another feature which should be examined is the irregular reverse motion between October 2002 and January 2003 which characterises the dip slip curve at “Shinos A” monitoring site (fig. 4.22a). This feature has been described in paragraph 4.5.2 and it is not certain whether the reverse movement at the beginning of the monitoring period is induced by climatic factors (e.g. temperature), technical factors (instrument related) or if it is indeed related to endogenic processes. Concerning the relation of this feature to the local seismicity, no earthquakes can be correlated with the reverse motion itself. Nevertheless it is interesting that the reverse trend changed between June 2003 and November 2003 to a normal motion, because on the 11th of August 2003 an earthquake of magnitude 2.6 took place less than 1km south from the monitoring site at a depth of 4km. It is of course unclear whether this earthquake was indeed responsible for the change of slip direction because the respective displacement measurements were taken on the 19th of Jun. and the 24th of Nov. and not immediately before and after that earthquake.

The considerations and observations above imply that only two isolated cases of fault displacements have a potential relation to earthquakes. Therefore the majority of the displacements and in general the established displacement trends at the monitoring sites evolved rather independently from the progress of the microseismic activity. As a

consequence, the general behaviour of the faults during the monitoring period can be characterised as creeping. This creeping, which is observed on the surface, should not be considered to have a purely aseismical origin. Earthquakes with magnitudes in the range of 3, such as the ones observed during the monitoring period, correspond to a small source radius of 300-400m and only a few millimetres of slip at depth (RIGO et al. 1996). Hence, it can also be assumed that the weak displacements of the frequent microearthquakes in Gulf of Corinth, which occur as distinct events at depth, are expressed on the surface as a more or less constant displacement trend dispersed in time.

The fault creeping, ascertained in the present study, corroborates the findings of CLARKE et al. (1998) and BRIOLE et al. (2000). These authors compared, on regional scale, the geodetically measured deformation (GPS) of the entire Gulf of Corinth with its seismicity and also postulated that part of the regional deformation on the surface should be taking place along some faults as creeping.

In the case of the present study the fault displacements were measured directly on certain fault outcrops and for a period of 1 to 3,5 years depending on the monitoring site. The intervals between the displacement readings had lengths of 3 to 6 months apart from the last one which was about 10 months long. The discontinuous way of reading the fault displacements did not allow a more precise correlation between the displacement progress of the faults and the ongoing local seismicity. In addition the seismic data derived from the national seismographic network of Greece and their accuracy is not optimal. Ideally, a local and dense seismographic network in combination with a technique of continuous displacement monitoring would provide satisfactory data to reveal in detail the relation between the fault displacements and the seismicity.

Table 4.1
 Earthquake data for the period of fault monitoring at the Perachora peninsula

| DATE | TIME | LAT. | LONG. | DEPTH | M | 20. Jun 04 | 11 14 54.0 | 38.15 | 23.23 | 3 | 2.5 |
|------------|------------|-------|-------|-------|-----|------------|------------|-------|-------|----|-----|
| 22. Apr 02 | 09 54 9.3 | 37.94 | 22.8 | 4 | 2.7 | 21. Jun 04 | 19 41 56.3 | 38.15 | 23.1 | 5 | 2.2 |
| 21. Aug 02 | 15 43 53.5 | 38.17 | 23.28 | 4 | 2.4 | 21. Jun 04 | 09 22 8.0 | 38.19 | 23.11 | 5 | 2.7 |
| 16. Sep 02 | 07 50 36.6 | 37.98 | 22.75 | 3 | 3.1 | 21. Jun 04 | 14 00 30.6 | 38.19 | 23.18 | 7 | 2.5 |
| 20. Sep 02 | 05 36 51.1 | 38.13 | 22.75 | 13 | 3.2 | 21. Jun 04 | 01 19 21.3 | 38.11 | 23.21 | 5 | 2.3 |
| 05. Oct 02 | 19 03 46.0 | 38.07 | 22.91 | 14 | 3.2 | 22. Jun 04 | 14 33 57.1 | 38.35 | 23.25 | 4 | 2.2 |
| 26. Oct 02 | 18 19 43.3 | 38.11 | 22.77 | 12 | 3.6 | 23. Jun 04 | 10 55 9.9 | 38.16 | 23.03 | 10 | 2.4 |
| 21. Nov 02 | 20 08 24.7 | 38.09 | 22.83 | 10 | 2.9 | 25. Jun 04 | 03 33 6.7 | 38.1 | 23.1 | 5 | 3.1 |
| 28. Nov 02 | 20 25 13.8 | 37.93 | 23.27 | 5 | 3.5 | 27. Jun 04 | 14 53 1.6 | 38.01 | 23.39 | 5 | 2.4 |
| 05. Dec 02 | 01 42 0.9 | 38.02 | 23.14 | 10 | 3.3 | 28. Jun 04 | 00 18 3.4 | 38.15 | 23.1 | 5 | 2.2 |
| 24. Feb 03 | 06 49 45.2 | 38.29 | 23.4 | 4 | 2.4 | 29. Jun 04 | 18 54 36.8 | 38.19 | 23.13 | 14 | 2.7 |
| 27. Mar 03 | 05 04 32.3 | 38.16 | 23.26 | 5 | 2.5 | 29. Jun 04 | 18 47 8.7 | 38.15 | 23.18 | 8 | 2.1 |
| 04. Apr 03 | 14 22 21.3 | 38.28 | 23.29 | 10 | 2.7 | 29. Jun 04 | 15 20 48.5 | 38.24 | 23.37 | 5 | 2.2 |
| 08. Apr 03 | 18 17 30.4 | 38.14 | 22.74 | 10 | 3.3 | 30. Jun 04 | 14 58 27.8 | 38.13 | 23.13 | 5 | 2.6 |
| 21. Apr 03 | 22 46 13.3 | 38.05 | 22.71 | 10 | 2.9 | 30. Jun 04 | 03 08 13.7 | 38.18 | 23.13 | 11 | 2.2 |
| 20. Jul 03 | 21 31 11.6 | 38.03 | 22.89 | 10 | 3.1 | 02. Jul 04 | 11 41 6.0 | 38.13 | 23.13 | 4 | 2.5 |
| 11. Aug 03 | 17 24 16.0 | 38.05 | 23.09 | 4 | 2.6 | 13. Jul 04 | 21 46 34.7 | 38.21 | 23.07 | 12 | 2.4 |
| 21. Dec 03 | 17 49 23.8 | 38.08 | 23.1 | 4 | 2.3 | 20. Jul 04 | 09 20 58.5 | 38.16 | 23.16 | 3 | 2.2 |
| 02. Jan 04 | 20 45 28.2 | 38.18 | 23.29 | 6 | 2.5 | 26. Jul 04 | 09 14 6.8 | 38.2 | 23.11 | 7 | 2.3 |
| 12. Jan 04 | 02 20 24.5 | 38.11 | 22.77 | 5 | 3.1 | 28. Jul 04 | 15 23 24.9 | 38.13 | 23.11 | 5 | 2.4 |
| 03. Mar 04 | 23 00 31.0 | 38.02 | 23.03 | 10 | 3.1 | 29. Jul 04 | 00 09 21.8 | 38.13 | 23.25 | 5 | 2.3 |
| 03. Mar 04 | 23 15 54.4 | 38.27 | 23.2 | 5 | 2.5 | 30. Jul 04 | 07 43 18.2 | 38.15 | 23.16 | 10 | 2.7 |
| 19. Mar 04 | 02 38 56.8 | 38.13 | 23.2 | 5 | 2.3 | 31. Jul 04 | 22 50 11.3 | 38.13 | 23.08 | 4 | 2.3 |
| 27. Mar 04 | 17 53 23.8 | 37.97 | 23.23 | 10 | 2.3 | 01. Aug 04 | 13 23 12.3 | 38.16 | 23.14 | 5 | 2.3 |
| 29. Mar 04 | 13 57 6.2 | 38.12 | 23.22 | 11 | 2.5 | 08. Aug 04 | 19 43 56.1 | 38.39 | 22.79 | 5 | 2.5 |
| 10. Apr 04 | 12 43 49.1 | 38.1 | 23.23 | 13 | 2.4 | 10. Aug 04 | 23 41 38.9 | 38.12 | 23.25 | 2 | 2.3 |
| 10. Apr 04 | 15 47 45.3 | 38.12 | 23.31 | 4 | 2.1 | 23. Aug 04 | 06 48 10.9 | 38.12 | 23.15 | 5 | 2.3 |
| 11. Apr 04 | 03 01 29.0 | 38.14 | 23.19 | 5 | 2.6 | 24. Aug 04 | 20 08 59.2 | 38.1 | 23.01 | 2 | 2.4 |
| 19. May 04 | 23 57 26.9 | 38.32 | 23.38 | 5 | 2.3 | 29. Aug 04 | 06 43 46.3 | 38.11 | 23.15 | 5 | 2.8 |
| 21. May 04 | 22 49 32.9 | 38.11 | 23.18 | 5 | 2.3 | 06. Sep 04 | 00 17 0.1 | 38.16 | 23.2 | 4 | 2.6 |
| 22. May 04 | 09 18 56.5 | 38.03 | 23.33 | 14 | 2.3 | 19. Sep 04 | 09 28 28.8 | 38.16 | 23.12 | 9 | 2.3 |
| 08. Jun 04 | 02 16 10.2 | 38.15 | 23.29 | 2 | 2.4 | 19. Sep 04 | 18 32 0.7 | 38.16 | 23.13 | 2 | 2.4 |
| 10. Jun 04 | 18 25 2.3 | 38.15 | 23.17 | 14 | 2 | 20. Sep 04 | 14 17 2.8 | 38.19 | 23.03 | 5 | 2.4 |
| 10. Jun 04 | 17 44 5.1 | 38.12 | 23.23 | 5 | 3 | 20. Sep 04 | 09 13 19.2 | 38.04 | 23.22 | 5 | 2.6 |
| 10. Jun 04 | 18 09 55.3 | 38.15 | 23.23 | 9 | 2.2 | 21. Sep 04 | 16 50 41.7 | 38.19 | 23.14 | 6 | 2.5 |
| 11. Jun 04 | 17 50 15.4 | 38.14 | 23.23 | 2 | 2.6 | 21. Sep 04 | 20 47 30.2 | 38.25 | 23.35 | 12 | 2.3 |
| 11. Jun 04 | 12 60 24.6 | 38.15 | 23.29 | 5 | 2.2 | 22. Sep 04 | 05 44 45.6 | 38.16 | 23.26 | 5 | 2.4 |
| 12. Jun 04 | 06 56 5.9 | 38.15 | 23.2 | 4 | 2.4 | 23. Sep 04 | 02 39 35.4 | 38.16 | 23.16 | 6 | 2.3 |
| 13. Jun 04 | 06 40 29.2 | 38.34 | 22.71 | 5 | 2.8 | 17. Oct 04 | 08 52 36.2 | 38.16 | 23.13 | 4 | 2.2 |
| 13. Jun 04 | 19 37 14.3 | 38.12 | 23.22 | 12 | 3.4 | 26. Oct 04 | 00 39 59.5 | 38.4 | 23.21 | 4 | 2.5 |
| 13. Jun 04 | 20 25 56.2 | 38.24 | 23.32 | 7 | 2 | 29. Oct 04 | 09 48 58.3 | 38.19 | 23.4 | 4 | 2.2 |
| 14. Jun 04 | 00 39 3.6 | 38.13 | 23.16 | 5 | 2.3 | 02. Nov 04 | 01 27 15.4 | 37.92 | 23.4 | 4 | 2 |
| 14. Jun 04 | 01 33 53.9 | 38.13 | 23.2 | 5 | 2.5 | 03. Nov 04 | 23 32 29.8 | 37.9 | 22.92 | 4 | 2.7 |
| 14. Jun 04 | 21 19 45.0 | 38.16 | 23.23 | 10 | 3 | 08. Nov 04 | 01 43 31.0 | 38.14 | 23.28 | 2 | 2.4 |
| 15. Jun 04 | 16 02 43.0 | 38.2 | 23.29 | 12 | 2.2 | 13. Nov 04 | 03 57 53.5 | 38.25 | 23.12 | 3 | 2.6 |
| 15. Jun 04 | 16 57 15.0 | 38.22 | 23.32 | 13 | 2.2 | 13. Nov 04 | 19 26 46.2 | 38.2 | 23.39 | 15 | 2.3 |
| 16. Jun 04 | 19 45 29.5 | 38.11 | 23.13 | 5 | 2.1 | 01. Dec 04 | 09 56 48.9 | 38.29 | 23.24 | 10 | 2.2 |
| 16. Jun 04 | 08 32 28.9 | 38.16 | 23.14 | 7 | 2.5 | 05. Dec 04 | 23 44 24.1 | 38.2 | 23.21 | 4 | 2.6 |
| 16. Jun 04 | 11 30 25.9 | 38.13 | 23.14 | 8 | 2.4 | 05. Dec 04 | 23 38 54.3 | 38.34 | 23.26 | 4 | 2.6 |
| 16. Jun 04 | 23 59 19.0 | 38.16 | 23.14 | 8 | 2.1 | 06. Dec 04 | 22 18 15.8 | 38.17 | 23.13 | 5 | 2.5 |
| 16. Jun 04 | 02 51 2.8 | 38.14 | 23.18 | 3 | 2.2 | 28. Dec 04 | 07 14 34.3 | 38.17 | 23.13 | 4 | 2.5 |
| 17. Jun 04 | 12 55 25.6 | 37.91 | 23.02 | 4 | 2.4 | 30. Dec 04 | 11 02 33.6 | 38.24 | 23.36 | 8 | 2.2 |
| 17. Jun 04 | 07 42 33.3 | 38.21 | 23.1 | 8 | 2.3 | 22. Jan 05 | 20 24 13.1 | 38.07 | 22.84 | 3 | 2.8 |
| 17. Jun 04 | 17 13 9.3 | 38.14 | 23.11 | 5 | 2.3 | 06. Feb 05 | 20 08 54.3 | 38.21 | 23.16 | 5 | 2.4 |
| 17. Jun 04 | 00 18 56.8 | 38.15 | 23.16 | 8 | 2.3 | 07. Feb 05 | 08 09 43.8 | 38.29 | 23.26 | 10 | 2.5 |
| 18. Jun 04 | 10 41 40.7 | 38.17 | 23.16 | 2 | 2.6 | 09. Feb 05 | 05 00 54.1 | 38.18 | 23 | 10 | 2.8 |
| 18. Jun 04 | 12 37 6.3 | 38.16 | 23.17 | 9 | 2.5 | 09. Feb 05 | 04 58 19.4 | 38.18 | 23.15 | 11 | 2.5 |
| 19. Jun 04 | 23 30 55.7 | 38.13 | 23.12 | 5 | 2.3 | 09. Feb 05 | 01 17 47.0 | 37.99 | 23.26 | 10 | 2.4 |
| 19. Jun 04 | 13 40 58.7 | 38.12 | 23.14 | 5 | 2 | 09. Feb 05 | 01 33 52.8 | 38.11 | 23.4 | 10 | 2.3 |
| 19. Jun 04 | 23 01 6.5 | 38.11 | 23.18 | 5 | 2.1 | 08. Mar 05 | 14 34 8.4 | 38.21 | 23.35 | 4 | 2.4 |
| 19. Jun 04 | 21 39 21.4 | 38.13 | 23.18 | 6 | 2.2 | 10. Mar 05 | 18 52 30.9 | 38.1 | 23.3 | 5 | 2.4 |
| 19. Jun 04 | 20 00 44.8 | 38.32 | 23.4 | 5 | 2.8 | 16. Mar 05 | 02 59 33.6 | 37.97 | 23.08 | 5 | 2.3 |
| 20. Jun 04 | 04 03 0.2 | 38.15 | 23.05 | 5 | 2.1 | 21. Mar 05 | 18 08 23.1 | 38.04 | 23 | 3 | 2.8 |
| | | | | | | 29. Mar 05 | 22 46 36.6 | 38.03 | 23.33 | 10 | 2 |

| | | | | | | | | | | | |
|------------|------------|-------|-------|----|-----|------------|------------|-------|-------|----|-----|
| 29. Mar 05 | 21 49 16.7 | 37.95 | 23.4 | 2 | 2.2 | 13. May 05 | 00 48 40.3 | 37.99 | 23.29 | 3 | 3.3 |
| 01. Apr 05 | 21 41 49.2 | 38.2 | 23.17 | 14 | 3.1 | 13. May 05 | 03 54 3.7 | 38.22 | 23.34 | 3 | 2.6 |
| 01. Apr 05 | 21 47 46.9 | 38.16 | 23.19 | 5 | 2.4 | 21. May 05 | 00 10 53.9 | 38.03 | 22.74 | 4 | 2.8 |
| 02. Apr 05 | 08 39 10.1 | 38.18 | 23.2 | 5 | 2.5 | 21. May 05 | 00 10 15.0 | 38.06 | 22.9 | 7 | 2.7 |
| 02. Apr 05 | 03 17 35.8 | 38.28 | 23.27 | 3 | 2.7 | 06. Jun 05 | 22 27 23.9 | 37.99 | 23.12 | 15 | 2.7 |
| 24. Apr 05 | 19 27 32.5 | 38.13 | 22.79 | 5 | 2.8 | 06. Jun 05 | 21 24 25.0 | 38.08 | 23.24 | 10 | 2.6 |
| 03. May 05 | 22 38 18.4 | 37.97 | 23.15 | 5 | 2.2 | 10. Jun 05 | 16 32 37.7 | 38.24 | 22.86 | 3 | 2.6 |
| 03. May 05 | 21 38 38.8 | 37.91 | 23.38 | 6 | 1.9 | 13. Jun 05 | 16 55 23.0 | 38.35 | 23.26 | 5 | 2.6 |
| 05. May 05 | 23 48 49.6 | 38.06 | 23.31 | 15 | 3.3 | 16. Jun 05 | 05 04 19.5 | 38 | 23.38 | 12 | 2.9 |
| 09. May 05 | 21 51 1.4 | 38.16 | 22.78 | 2 | 3 | 30. Jun 05 | 11 56 57.6 | 37.94 | 23.32 | 5 | 2.4 |
| 09. May 05 | 11 14 26.3 | 38.05 | 23.37 | 10 | 2.5 | 04. Jul 05 | 14 58 11.1 | 38.21 | 23.14 | 5 | 2.5 |
| 12. May 05 | 22 41 15.5 | 37.98 | 23.26 | 5 | 2.4 | 18. Jul 05 | 23 41 45.4 | 37.9 | 23.15 | 2 | 2.8 |
| 12. May 05 | 21 25 19.6 | 38.21 | 23.39 | 4 | 2.4 | 25. Jul 05 | 20 07 36.9 | 38.16 | 23.25 | 5 | 2.3 |
| 12. May 05 | 21 50 48.5 | 37.93 | 23.4 | 5 | 2.3 | | | | | | |

4.7 An approach to the regional extension rate of the eastern Gulf of Corinth

Through the utilization of the three monitoring sites at the Perachora peninsula it has been demonstrated that the corresponding faults display an undisputable displacement activity on the surface. Although the measured displacements should be considered as the local manifestation of the tectonic activity at each monitoring site, they can be used in order to evaluate the regional extension rates at the eastern Gulf of Corinth.

For the purpose of such an evaluation, the following factors need to be considered. First of all, the number of faults which are responsible for the extension at the eastern Gulf of Corinth should be taken into account. Second, a characteristic horizontal extension rate is needed, which can be used as a rule for each fault. Finally, possible differences in the degree of activity of the faults should be estimated.

As far as the number of faults in the eastern Gulf of Corinth is concerned, it is important to include not only the faults on the Perachora peninsula but also the offshore faults at the bottom of the Gulf of Alkyonides. Fig. 4.35 depicts a NNW-SSE directed cross section across the Gulf of Alkyonides and the Perachora peninsula which includes 15 faults. The location and the number of the offshore faults in this cross-section are based on seismic reflection images of STEFATOS et al. (2002).

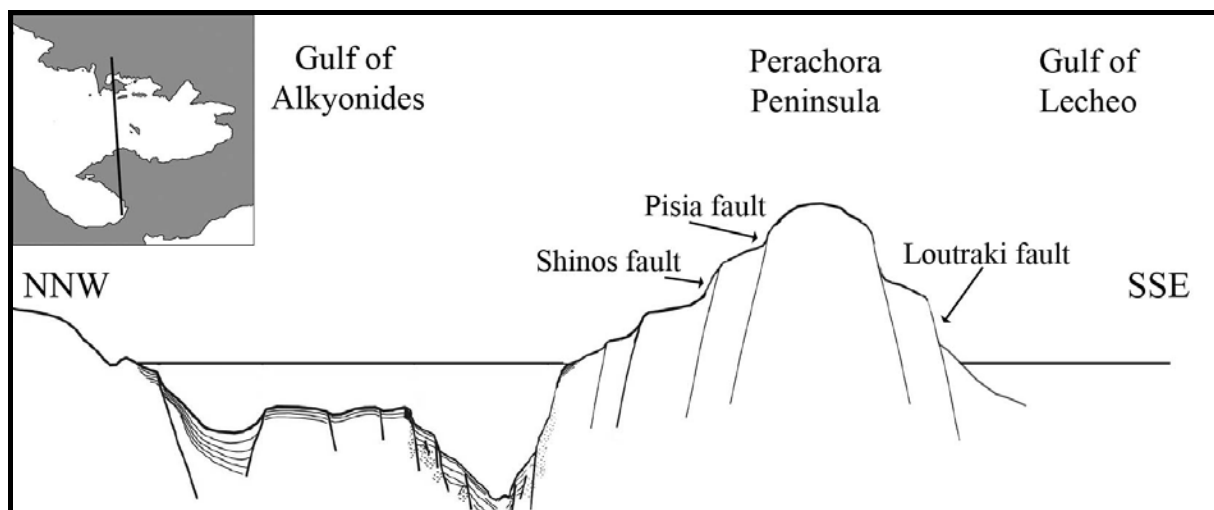


Fig. 4.35: NNW-SSE directed cross section through Gulf of Alkyonides, Perachora peninsula and Gulf of Lecheo.(based on STEFATOS et al. 2002).

Regarding the horizontal extension taking place at each fault, the results from the “Pisia” monitoring site can be considered as the most representative ones because the duration of

displacement monitoring at this site was the longest one and the concerned fault plane belongs to a main fault of the area. If we consider that the Pisia fault is WSW-ENE orientated then it is obvious that only the dip-slip movements and the movements perpendicularly to the fault plane contribute to the NNW-SSE directed extension whereas the strike slip displacements have no effect on it. The dip angle of the Pisia fault at the “Pisia” monitoring site is 40° and therefore, by using simple trigonometry, the dip-slip rate and the rate of displacement perpendicularly to the fault plane yield a horizontal extension of 0.45mm/year.

If the aforementioned extension rate is assigned to each of the faults in fig. 4.35 then the total horizontal extension along the cross section is calculated at 6.75mm/year. This amount of extension is fairly comparable to the average of 4-10mm/year which are proposed by GPS measurements for the eastern area of the Gulf of Corinth (DAVIES et al. 1997, CLARKE et al. 1997, CLARKE et al. 1998, BRIOLE et al. 2000, AVALLONE et al. 2004). The foregoing assumption is, of course, rather arbitrary because it is not certain that all the faults in the area behave in the same way as the Pisia fault. In addition, the Pisia fault might accommodate larger amounts of extension at locations other than that of the monitoring site. In the latter case, the current extension along the cross section of fig.4.35 will be expected to be higher i.e. similar to the upper limit of the GPS based estimations.

It is possible to refine the distribution of the extension on the faults of fig. 4.35 by considering that the south dipping faults, i.e. the ones that are antithetic to the major north dipping onshore and offshore faults, are less active. According to ARMIJO et al. (1996) and BENEDETTI et al. (2003) the antithetic faults at the eastern Gulf of Corinth have slip rates of about 10% of the rates of the major north dipping faults. Consequently, if the number of antithetic faults (8) in fig. 4.35 is taken into account then the total extension along the cross section amounts 3.5mm/year (when extension of 0.45mm/year is still assigned to the north dipping faults). This rate is still plausible as it is similar to the lower limit of the geodetically (GPS) estimated extension at the eastern Gulf of Corinth.

The regional extension rates which were estimated above concern an interseismic period. Hence, in case of a strong earthquake or earthquake series the overall extension will be larger. Moreover, it is uncertain whether the entire deformation is concentrated only on the distinct faults of fig. 4.35 or if it is also taking place within the blocks between them, on unknown faults or on faults located further to the south. The aforementioned considerations imply once

again that the calculation of the extension rate at the eastern Gulf of Corinth, as described above, is a fair approximation and that actual values may vary.

The important outcome from these two modelling attempts is that a horizontal extension rate of at least 0,45mm/year is indeed a representative value which can be realistically proposed as the characteristic one for the major north dipping faults at the eastern Gulf of Corinth.

5 Summary

The present study concerns the tectonic activity at the Gulf of Corinth in Greece. The Gulf of Corinth is an extensional feature within the general extension which characterises the Aegean region since Miocene. The formation of the Gulf of Corinth initiated in Pliocene times and today the gulf has evolved to a complex graben structure.

Within the present study, the tectonic fabric of the Gulf of Corinth is evaluated by means of satellite image interpretation and fieldwork observations. The satellite image interpretation reveals a dense tectonic fabric along the southern coast of Gulf of Corinth. The azimuthal distribution of the tectonic lineaments indicates two orthogonal faults systems: an older fault system consisting of NNW-SSE and WSW-ENE trending faults and a younger system consisting of WNW-ESE and NNE-SSW trending faults. The younger fault system is the prevailing one and is responsible for the formation of the Gulf of Corinth.

The stress field of the Gulf of Corinth is determined by evaluating the azimuthal distribution of the tectonic lineaments and by analysing the fault kinematic data (lineations) collected in the field. Two successive stress regimes are recognized: a paleo-stress regime of NNW-SSE directed extension which was gradually replaced in Pliocene times by a younger regime of NNE-SSW directed extension. The older stress regime was responsible for the formation of the older fault system. The younger stress regime is still active today and it has been responsible for the formation of the younger fault system and consequently for the Gulf of Corinth.

The dense tectonic fabric has a particular impact on the frequent manifestation of the landslides in the area of the Gulf of Corinth. In the present study, this impact is investigated in a selected area where 61 landslides were located by means of fieldwork and air-photograph evaluation. The spatial and azimuthal distribution of the landslides is imposed to a great degree by the distribution of the tectonic fabric. Approximately 50% of the studied landslides were found to be related with the presence of faults and 30% had failure planes with strike directions similar to that of the present faults. Moreover it is concluded that the increased frequency of mass movements within the area is primarily owing to the combination of steep morphology, poor physical properties of the prevailing fine grained sediments and the dense

and active tectonic elements of the area. Nevertheless, other elements such as water (precipitation) and anthropogenic influence act as significant landslide triggering factors.

The primary objective of the present study is to quantify the displacement behaviour of representative faults at the Gulf of Corinth. Two types of instruments are utilized for this purpose at three fault monitoring sites along the Pisias-Shinos fault zone which is located at the Perachora peninsula (eastern termination of the Gulf of Corinth). The first type, known as TM71 is a device based on the phenomenon of the Moiré optical interference and provides 3-dimensional measurement capability. The second type of instrument, known as BGX, is an extensometer based on Bragg-Grating fibre-optic sensors and in the present study it is proved to be reliable for 1-dimensional measurements.

According to the local paleo-stress analysis, the direction of extension which is responsible for the creation of the Pisias-Shinos fault zone (and the local fault systems parallel to it at the Perachora peninsula) was NNW-SSE orientated i.e. discrepant to the NNE-SSW extension prevailing at the rest of the Gulf of Corinth. The NNW-SSE directed extension at the Perachora peninsula has been established since 1Mio years and is found to be in agreement with that determined by recent GPS-based studies and focal mechanism analyses. Therefore it is concluded that this type of stress field is still active at the Perachora peninsula.

As far as the monitoring of fault displacements is concerned, three fault monitoring sites were established along the Pisias-Shinos fault zone: The “Pisia”, the “Shinos A” and “Shinos B” monitoring site. At all three monitoring sites the dip slip movements, the strike slip movements and the movements perpendicularly to the fault plane were measured by means of TM71 devices. A BGX device was installed only at the “Pisia” and “Shinos A” monitoring sites and measured the displacement perpendicularly to the fault planes. The length of the monitoring periods was 12 months at the youngest monitoring site (“Shinos B”), 34 months for the “Shinos A” monitoring site and 42 months for the “Pisia” monitoring site.

The monitoring results from the “Pisia” site indicate stable trends of displacement along all three components of motion. More precisely, the Pisias fault at this monitoring site demonstrates 0.44mm/year normal slip, 0.40mm/year dextral slip and 0.18mm/year opening of the fault gap (perpendicularly to the fault plane). The other two monitoring sites are characterised by weaker displacements. The “Shinos A” monitoring site displays only a weak

dextral trend (0.04mm/year) whereas along the other two components of measurement no significant long term tendency is observed. At the “Shinos B” monitoring site, the length of the monitoring period is not sufficient for a reliable estimation of annual displacement trends. However a tendency to normal slip and opening of the fault gap can be postulated.

Regarding the performance of the monitoring methods, climatic effects induce periodic fluctuations on the displacement curves. Most probably, the main cause is the volumetric response of the rocks to seasonal temperature changes perhaps in combination with non-compensated temperature effects on the instruments. However, these fluctuations cannot obscure long term displacement trends. Regarding the performance of the Bragg-Gitter extensometer, it is comparable to that of the TM71 when some technical prerequisite are fulfilled and when the displacements are relatively large, e.g. at the “Pisia” monitoring site where the displacements perpendicularly to fault plane are significant (see trend above).

The measured displacements and trends at each monitoring site are, in general, consistent with the extensional stress field at the Perachora peninsula. Some discrepancies e.g. noticeable lateral trends (strike slip) can be plausibly explained as a result of local fault kinematics and as a result of stronger motion at neighbouring faults.

During the monitoring activities, no significant earthquakes took place in the Perachora region. The displacements and the established displacement trends at the fault monitoring sites evolved rather independently from the contemporaneous microseismic activity. Only two isolated cases of fault displacements have a potential relation to earthquakes but these can be considered only as indications. In general, it can be stated that the fault displacements have a creeping character. However, it remains unclear whether this creeping behaviour is induced by purely aseismical processes. Another possibility is that the abrupt and minor displacements at depth (few millimetres), that correspond to the ongoing microseismic activity, reach the surface with delay and dispersed in time, i.e. are expressed on the surface as more or less constant displacement trends.

Finally the extension rate across the eastern extremity of the Gulf of Corinth is determined. For this estimation the local rate of horizontal extension at the “Pisia” monitoring site is chosen as representative and is extrapolated to a regional scale by taking into consideration the number of major faults in the area and their potential degree of activity. The overall

displacement trend at the “Pisia” monitoring site corresponds to a local, NNW-SSE directed extension of 0.45mm/year and the estimated extension rate across the eastern end of the Gulf of Corinth is between 3.5mm/year and 6.75mm/year. This estimation is realistic as it is within the range proposed by geodetical surveys for the area (based on GPS) but it should be considered only as a fair approximation. The important outcome from this extrapolation is that a horizontal extension rate of at least 0.45mm/year can be realistically proposed as the average one for each major north dipping fault at the eastern Gulf of Corinth.

References

- ADVANCED OPTIC SOLUTIONS, 2002. Betriebsanleitung für AWE-MxX-RS (Auswerte-Einheit für Faser-Bragg-Gitter-Sensoren)
- AMBRASEYS N. N., JACKSON, J. A., 1990 Seismicity and associated strain of central Greece between 1890 and 1988. *Geophys. J. Int.* 101, 663-708.
- ANGELIER, J. & MECHLER, P., 1977. Sur une méthode graphique de recherche des contraintes principales également utilisable en tectonique et enséismologie: la methode des diédres droits. – *Bull. Soc. Géol. France* , VII, 19: 1309-1318; Paris.
- ARMIJO, R., MEYER, B., KING, G.C.P., RIGO, A., PAPANASTASIOU, D., 1996. Quaternary evolution of the Corinth rift and ist impications for the Late Cenozoic evolution of the Aegean. *Geophysical Journal International* 126, 11-53.
- AVALLONE, A., BRIOLE, P., AGATZA-BALODIMOU, A.M., BILLIRIS, H., CHARADE, O., MITSAKAKI, CH., NERCESSIAN, A., PAPAZISSI, K., PARADISSIS, D., VEIS, G., 2004. Analysis of eleven years of deformation measured by GPS in the Corinth Rift Laboratory area. *C. R. Geoscience*, 336, 301–311.
- BENEDETTI, L., FINKEL, R., KING, G., ARMIJO, R., PAPANASTASIOU, D., RYERSON, F.J., FLERIT, F., FARBER, D., STAVRAKAKIS, G., 2003. Motion on the Kaparelli fault (Greece) prior to the 1981 earthquake sequence determined from ³⁶Cl cosmogenic dating. *Terra Nova*, 15, 118-124.
- BERNARD, P., MEYER, B., LYON-CAEN, H., GOMEZ, J.-M., TIBERI, C., BERGE, C., CATTIN, R., HATZFELD, D., LACHET, C., LEBRUN, B., DESCHAMPS, A., COURBOULEX, F., LARROQUE, C., RIGO, A., MASSONNET, D., PAPADIMITRIOU, P., KASSARAS, J., DIAGOURTAS, D., MAKROPOULOS, K., VEIS G., E. PAPAZISI, MITSAKAKI, C., KARAKOSTAS, V., PAPADIMITRIOU, E., PAPANASTASSIOU, D., CHOULIARAS, G., STAVRAKAKIS, G., 1997. The Ms=6.2, June 15, 1995 Aigion earthquake (Greece): Evidence for low-angle normal faulting in the Corinth rift, *J. Seismol.* 1, 131-150.
- BRIOLE, P., RIGO, A., LYON-CAEN, H., RUEGG, J.C., PAPAZISSI, K., MITSKAKI, C., BALODIMOU, A., VEIS, G., HATZFELD, D., DESCHAMPS, A., 2000, Active deformation of the Corinth rift, Greece: Results from repeated Global Positioning System surveys between 1990 and 1995. *Journal of Geophysical Research*, vol 105, 25,605-266,25.
- BROOKS, M., FERENTINOS, G., 1984. Tectonics and sedimentation in the Gulf of Corinth and the Zakynthos and Kefallinia channels, western Greece. *Tectonophysics* 101, 25-54.

- BURGER, H., 1981. Untersuchungen zur Klassifizierung von Gesteinsoberflächen auf Landsat-Aufnahmen mit Hilfe von Signatur- und Texturparametern. Berl. Geowiss. Abh., Reihe A, 35: 102S.
- CLARKE, P.J., DAVIES R.R., ENGLAND, P.C., PARSONS, B.E., BILLIRIS, H., PARADISSIS, D., VEIS, G., CROSS, P.A., DENYS, P.H. ASHKENAZI, V., BINGLEY, R., KAHLE H.G., MULLER M.V., BRIOLE, P., 1998. Crustal strain in central Greece from repeated GPS measurements in the interval 1989-1997.). *Geophys. J. Int.* 135, 195-214.
- CLARKE, P.J., DAVIES R.R., ENGLAND, P.C., PARSONS, B.E., BILLIRIS, H., PARADISSIS, D., VEIS, G., DENYS, P.H., CROSS, P.A., ASHKENAZI, V., BINGLEY, R., 1997. Geodetic estimate of seismic hazard in the Gulf of Korinthos. *Geophysical Research Letters*, Vol 24, No. 11, 1003-1306.
- CLEMENT, C., SACHPAZI, M., PHILIPPE CHARVIS, PH., GRAINDORGE, D., LAIGLE, M., HIRN, A., ZAFIROPOULOS, G., 2004. Reflection–refraction seismics in the Gulf of Corinth: hints at deep structure and control of the deep marine basin. *Tectonophysics* 391, 97–108
- COLLIER, R.E.L., LEEDER, M.R., JACKSON, J.A., 1995. Quaternary drainage development, sediment fluxes and extensional tectonics in Greece. In: Lewinn, J., Mackli, M.G., Woodward, J.C., (Eds), *Mediterranean Quaternary River Environments*, Balkema, Rotterdam, 31-44.
- COLLIER, R.E.L., LEEDER, M.R., ROWE, P.J., ATKINSON, T.C., 1992. Rates of tectonic uplift in the Corinth and Megara basins, central Greece. *Tectonics* 11, 1159-1167.
- COLLIER, R.E.L., PANTOSTI, D., D' ADDEZIO, G., DE MARTINI, P.M., MASANA, E., SAKELLARIOU, D., 1998. Paleoseismicity of the 1981 earthquake fault: Seismic contribution to extensional strain in central Greece and implications for seismic hazard. *Journal of Geophysical Research* 103, 30,001-30,019.
- DAVIES, P., ENGLAND, P., PARSONS, B., BILLIRIS, H., PARADISSIS, D., VEIS, G., 1997. Geodetic strain of Greece in the interval 1892-1992. *Journal of Geophysical Research*, Vol 102, No. 11, 24,571-24,588.
- DOUSOS, T., KOKKALAS, S., 2001. Stress and deformation patterns in the Aegean Region. *Journal of Structural Geology*, Vol. 23, pp. 455-472.
- DOUSOS, T., KONTOPOULOS, N., FERENTINOS, G., 1985. Das westliche Ende des Korinth-Grabens. *N. Jb. Geol. Paläont. Mh.* 11, 652-666.
- DOUSOS, T., KONTOPOULOS, N., FRYDAS, D., 1987. Neotectonic evolution of the northwestern-continental Greece. *Geologische Rundschau*, 76/2, 433-450.

- DOUSOS, T., PIPER, D.J.W., 1990. Listric faulting, sedimentation, and morphological evolution of the Quaternary eastern Corinth rift, Greece: First stages of continental rifting. *Geological Society of America Bulletin*, v. 102, 812-829.
- DOUSOS, T., POULIMENOS, G., 1992. Geometry and kinematics of active faults and their seismotectonic significance in the western Corinth-Patras rift (Greece). *Journal of Structural Geology*, Vol. 14, No. 6, pp. 689-699.
- EURIMAGE, 2001. Products and Services catalogue (European). www.eurimage.com
- FECKER, E., KOSTAK, B., RYBAR, J., STEMBERK, J., 1999. Beobachtung rezenter tectonischer bewegungen im Wattkopf tunnel bei Ettlingen. *Jber. Mitt. Oberrhein. Geol. Ver., N.F.*, 81, 355-364.
- GILLESPIE, A.R. 1980. Digital techniques of image enhancement. In: Siegal, B.S., Gillespie, A.R., Eds. 1980 *Remote Sensing in Geology*. -701p., Willey & Sons, New York, (139-226).
- H.M.G.S. 1989a. Ayion Sheet. General purpose topographical map 1:50000. Hellenic Military Geographical Service.
- H.M.G.S. 1989b. Dervenion Sheet. General purpose topographical map 1:50000. Hellenic Military Geographical Service.
- H.M.G.S. 1989c. Xilokastron Sheet. General purpose topographical map 1:50000. Hellenic Military Geographical Service.
- H.G.M.S. 1998. Aerial Photography of Greece 1:15000, 24187-24190. Hellenic Military Geographical Service, Athens, Greece.
- HARP, E.L., JIBSON, R.W., 1995. Seismic instrumentation of landslides. Building a better model of dynamic landslide behaviour. *Bull. of the Seismological Society of America*. 85,93-99.
- HATZFELD, D., KARAKOSTAS, V., ZIAZIA, M., KASSARAS, I., PAPADIMITRIOU, E., MAKROPOULOS, K., VOULGARIS, N., PAPAIOANNOU, C., 2000. Microseismicity and faulting geometry in the Gulf of Corinth (Greece). *Geophys. J. Int.* 141, 438– 456.
- HIGGS, B., 1988. Syn-sedimentary structural controls on basin deformation in the Gulf of Corinth, Greece. *Basin Research*, 1, 155-165.
- HUBERT, A., KING, G.C.P., ARMIJO, R., MEYER, B., PAPANASTASIOU, D., 1996. Fault re-activation, stress interaction and rupture propagation of the 1981 Corinth earthquake sequence. *Earth Planetary Science Letters* 142, 573-585.
- I.G.M.E. 1984. Perachora Sheet. Geological map of Greece 1:50000, Institute of Geology and Mineral Exploration, Greece.

- I.G.M.E. 1989. Xilocastron Sheet. Geological map of Greece 1:50000, Institute of Geology and Mineral Exploration, Greece.
- I.G.M.E. 1993. Dhervenion Sheet. Geological map of Greece 1:50000, Institute of Geology and Mineral Exploration, Greece.
- INAUDI, D., VULLIET, L., PFLUG, L., VURPILLOT, S., WYSER, A., 1995. Low-coherence interferometry for the monitoring of underground work,. SPIE, North American Conference on Smart Structures and Materials, San Diego, USA, Vol 2444, p 171-178, 1995
- JACKSON, J.A., GAGNEPAIN, J., HOUSEMAN, G., KING, G.C.P., PAPADIMITRIOU, P., SOUFLERIS, P., VIRIEUX, J., 1982. Seismicity, normal faulting and the geomorphological development of the Gulf of Corinth (Greece): The Corinth earthquakes of February and March 1981, *Earth and Planetary Science Letters* 57, 377-397.
- KARAPIPERIS, L., 1974. Distribution of rainfalls in the Greek Territory. *Bull of the Geol. Soc. Greece*, XI(1), 1-27.
- KEEFER, V.K., 1984. Landslides caused by earthquakes. *Bull of Geol Soc. of America*, 95, 406-421.
- KING, G.C.P., OUYANG, Z.X., PAPADIMITRIOU, P., DESCHAMPS, A., GAGNEPAIN, L., HOUSEMAN, G., JACKSON, J.A., SOUFLERIS, C., VIRIEUX, J., 1985. The evolution of the Gulf of Corinth: An aftershock study of the 1981 earthquakes. *Geophys. J. R. Astron. Soc.* 77, 915-933.
- KOSTAK, B., 1969. A New Device for In-situ Movement detection and Measurement. *Experimental Mechanics*, vol. 9, 374-379.
- KOSTAK, B., 1991. Combined indicator using Moiré technique. *Proceedings of 3rd International Symposium on Field Measurements in Geomechanics*, Oslo, Norway, 53-60.
- KOSTAK, B., 2001. Crack gauge TM71 – an instrument for 3D microdisplacement measurements: TM71 instructions for use. (User's Manual)
- KOSTAK, B., 2002 . 3D crack gauging device TM71: Displacement calculations and compensation of temperature variation. (User's Manual)
- KOSTAK, B., AVRAMOVA-TACEVA, E., 1988. A method for contemporary displacement measurement on a tectonic fault. *Journal of Geodynamics*, vol. 10, 115-125.
- KOSTAK, B., CRUDEN, D.M. 1990. The Moiré crack gauges on the crown of the Frank Slide. *Canadian Geotechnical Journal*, vol. 27, 835-840.

- KOSTAK, B., DOBREV, N., ZIKA, P., IVANOV, P., 1998. Joint monitoring on a rock face bearing a historical bas-relief. *Quarterly Eng. Geol.*, vol. 31, 37-45.
- KOUKIS, G., ROZOS, D., HADZINAKOS, I., 1996a. Rainfall induced landslides in Achaia county, Greece. In: *Landslides*, Senneset (ed.) Balkema, Rotterdam.
- KOUKIS, G., TSIAMBAOS, G., SABATAKAKIS, N., 1996b. Landslides in Greece: Research evolution and qualitative analysis. In: *Landslides*, Senneset (ed.) Balkema, Rotterdam.
- KOUKIS, G., ZIOURKAS, C., 1991. Slope instability phenomena in Greece: a statistical analysis. *Bulletin of the International Association of Engineering Geology*, 34, 47-60.
- KOUKOUVELAS, I.K., 1998. The Egeion fault, earthquake-related and long term deformation, Gulf of Corinth, Greece. *Journal of Geodynamics*, 26, 501-513.
- KOUKOUVELAS, I.K., DOUSOS, T.T., 1996. Implications of structural segmentation during earthquakes: the 1995 Egeion earthquake, Gulf of Corinth, Greece. *Journal of Structural Geology*, Vol. 18, No. 12, pp.1381-1388.
- KOUKOUVELAS, I.K., STAMATOPOULOS, L., KATSONOPOULOU, D., PAVLIDES, S., 2001. A palaeoseismological and geoarchaeological investigation of the Eliki fault, Gulf of Corinth, Greece. *Journal of Structural Geology* 23, 531-543.
- KRONBERG, P., 1985. *Fernerkundung der Erde. Grundlagen und Methoden des Remote Sensing in der Geologie.* -394p., Enke, Stuttgart.
- KRONBERG, P., TSOMBOS, P. & SURBORG, B., 1981. Karte der Häufigkeitsverteilung von Landsat-Lineationen im Bereich Griechenland und der West-Türkei, 1:1 000 000. – Geologisches Institut TU Clausthal.
- LEEDER, M.R., COLLIER, R.E. LI., ABDUL AZIZ, L.H., TROUT, M., FERENTINOS, G., PAPTAEODOROU, G., LYBERIS, E., 2002. Tectono-sedimentary processes along an active marine/lacustrine half-graben margin: Alkyonides Gulf, E. Gulf of Corinth, Greece. *Basin Research* 14, 25-41.
- LEEDER, M.R., JACKSON, J.A., 1993. The interaction between normal faulting and drainage in active extensional basins, with examples from the western United States and central Greece. *Basin Research* 5, 79-102.
- LEEDER, M.R., SEGER, M., STARK, C.P., 1991. Sedimentology and tectonic geomorphology adjacent to active and inactive normal faults in the Megara basin and Alkyonides gulf, Central Greece. *J. Geol. Soc. London* 148, 331-343.
- LIMPERIS, E., PAPTAEODOROU, G., HASIOTIS, TH., FERENTINOS, G., 1998. Submarine faults within the active tectonic graben of the Gulf of Corinth. Four typical examples of

- modern tectonic control on morphology and sedimentation processes under the sea level. *Bulleting of the Geological Society of Greece* vol XXXII/2, 223-234.
- LIU, J.-G., SCHMIDT-HATTENBERGER, C., BORM, G., 2002. Dynamic strain measurement with a fibre Bragg grating sensor system. *Measurement*, 32, 151-161.
- LOVE, J., 1999. PIT (Photo interpretation tool). <http://rst.gsfs.nasa.gov/AppB/B1.html>
- MCCLUSKY, S., BALASSANIAN, S., BARKA, A., DEMIR, C., ERGINTAV, S., GEORGIEV, I., GURKAN, O., HAMBURGER, M., HURST, K., KAHLE, H., KASTENS, K., KEKELIDZE, G., KING, R., KOTZEV, V., LENK, O., MAHMOUD, S., MISHIN, A., NADARIYA, M., OUZOUNIS, A., PARADISSIS, D., PETER, Y., PRILEPIN, M., REILINGER, R., SANLI, I., SEEGER, H., TEALEB, A., TOKS, M. N., VEIS, G., 2000. Global Positioning System constraints on plate kinematics and dynamics in the eastern Mediterranean and Caucasus. *Journal of Geophysical. Research*, 105, 5695–5719.
- MORETTI, I., DELHOMME, J.P., CORNET, F., BERARD, P., SCHMIDT-HATTENBERGER, C., BORM, G., 2002. The Corinth rift laboratory: monitoring of active faults. *First break*, vol. 20.2, 91-97.
- MORETTI, I., SAKELARIOU, D., LYKOUSIS, V., MICARELLI, L., 2003. The Gulf of Corinth: an active half graben? *Journal of Geodynamics*, 36, 323-340.
- MOREWOOD, N.C., ROBERTS, G.P., 1997. The geometry, kinematics and rates of deformation in a normal fault segment boundary, central Greece. *Geophysical Research Letters* 24, 3081-3084.
- MOREWOOD, N.C., ROBERTS, G.P., 1999. Lateral propagation of the surface trace of the South Alkyonides normal fault segment, central Greece: its impact on models of fault growth and displacement-length relationships. *Journal of Structural Geology* 21, 635-652.
- MOREWOOD, N.C., ROBERTS, G.P., 2001. Comparison of surface slip and focal mechanism slip data along normal faults: an example from the eastern Gulf of Corinth, Greece. *Journal of Structural Geology* 23, 473-487.
- NATIONAL OBSERVATORY OF ATHENS, 2005. Earthquake Catalogue of Greece, www.noa.gr
- PANTOSTI, D., COLLIER, R.E.L., D'ADDEZIO, G., MASANA, E., SAKELLARIOU, D., 1996. Direct geological evidence for prior earthquakes on the 1981 Corinth fault (central Greece). *Geophys. Res. Lett.* 23, 3795-3798.
- PAPAZACHOS, B., 1975. Seismic activity along the Saronikos-Corinth-Patras gulfs. *Month Bull. Seism. Inst. Nat Observ. Athens.* 1-16.

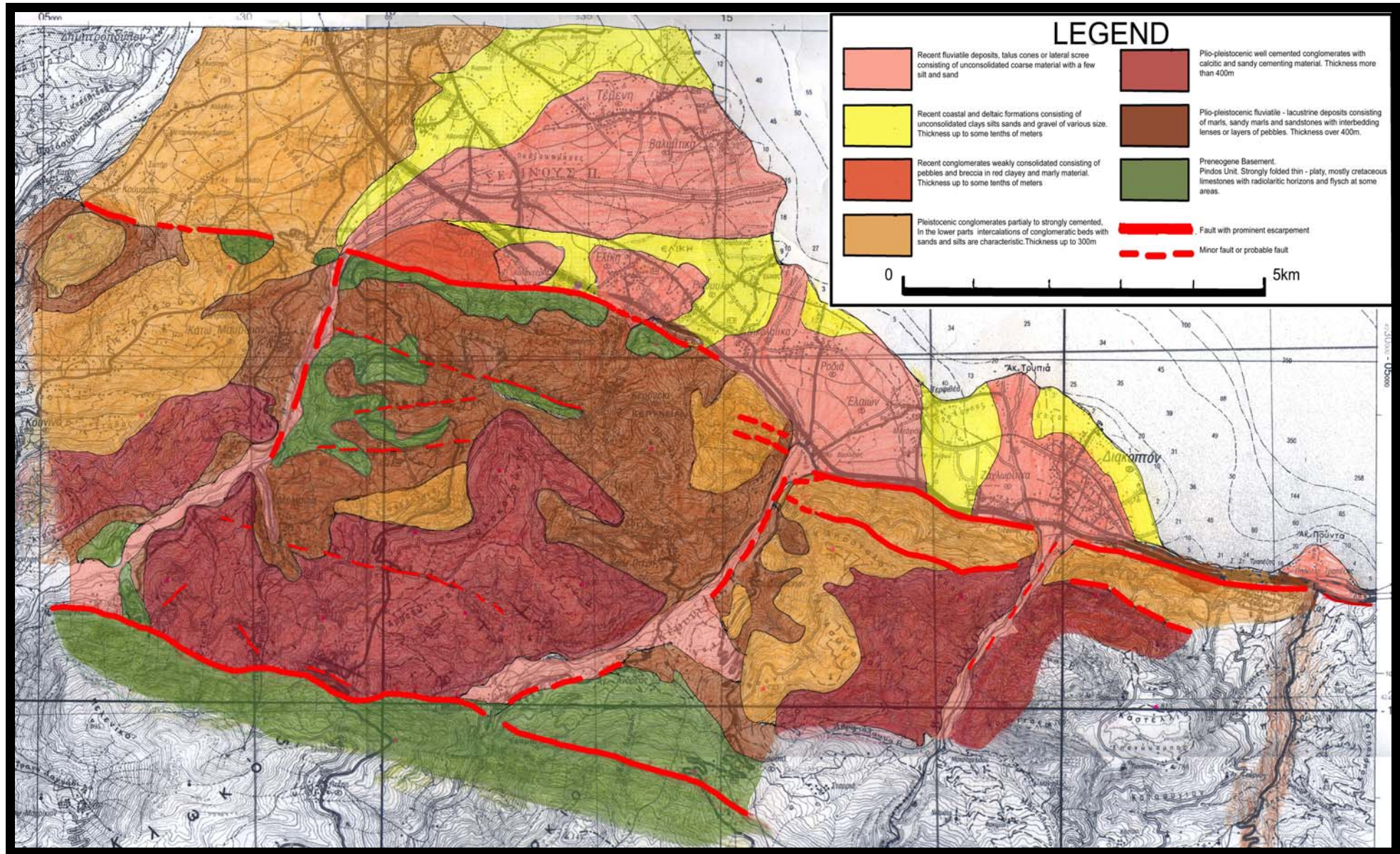
- PAPAZACHOS, B., COMINAKIS, P., MOUNDRAKIS, D., PAVLIDES, S., 1981. Preliminary results of an investigation of the february March Alkionides Gulf (Greece) earthquakes. *Int. Symp. Hellen. Arc and Trench (H.E.A.T.)*. Vol 2, 74-78.
- PETRO, L., POLASCINOVA, E., STERCZ, M., KOSTAK, B., 2005. Current results from 3-D monitoring of active faults in the western Carpathians. *Acta Geodyn. Geomater.* Vol.2, No.1 (137), 37-43.
- PIRAZZOLI, P.A., STIROS, S.C., ARNOLD, M., LABOREL, J., LABOREL-DEGUEN, F., PAPAGEORGIOU, S., 1994. Episodic uplift deduced from Holocene shorelines in the Perachora peninsula, Corinth area, Greece. *Tectonophysics* 229, 201-209.
- POULIMENOS, G., 1993. Tectonics and sedimentation in the western Corinth Graben, Greece. *N. Jb. Geol. Paläont. Mh.*, 1993, H. 10, 607-630.
- POULIMENOS, G., 2000. Scaling properties of normal fault populations in the western Corinth Graben, Greece: implications for fault growth in large strain settings. *Journal of Structural geology* 22, 307-322.
- POULIMENOS, G., ALBERS, G., DOUSOS, T., 1989 Neotectonic Evolution of the Central Section of the Corinth Graben. *Z. dt. geol. Ges.* 140, 173-182.
- REITER, F., ACS, P., 2003. *TectonicsFP (demo version)*. <http://go.to/tectonicsFP>
- RETTENMAIER, D. GUIRGEA V. HÖTZL H. FÖRSTER A NIKAS C. 2002. Geological mapping and hydrogeological testing of the block-faulted system in the hinterland of Egon. *Wissenschaftliches Programm und Abstracts. Gemeinsames ICDP-ODP Kolloquium* 06.-08. Juni 2002 Universität Potsdam.
- RIETBROCK, A., TIBERI, C., SCHERBAUM, F. & LYON-CAEN, H., 1996. Seismic slip on a low angle normal fault in the Gulf of Corinth: evidence from high-resolution cluster analysis of microearthquakes. *Geophys. Res. Lett.*, 23, 1817-1820.
- RIGO, A., LYON-CAEN, H., ARMIJO, R., DESCHAMPS, A., HATZFELD, D., MAKROPOULOS, K., PAPADIMITRIOU, P., KASSARAS, I., 1996. A microseismic study in the western part of the Gulf of Corinth (Greece): implications for large-scale normal faulting mechanisms. *Geophysical Journal International* 126, 663-688.
- ROBERTS, G.P., 1996a. Variation in fault-slip directions along active and segmented normal fault systems. *Journal of Structural Geology* 18, 835-845.
- ROBERTS, G.P., 1996b. Noncharacteristic normal faulting surface ruptures from the Gulf of Corinth, Greece. *Journal of Geophysical Research* 101, 25255-25267.
- ROBERTS, G.P., GAWTHORPE, R.L., 1995. Strike variation in deformation and diagenesis along segmented normal faults: an example from the eastern Gulf of Corinth, Greece. In:

- Lambiase, J.J. (Ed.), *Hydrocarbon Habitat in Rift Basins*. Geological Society Special Publication 80, 57-54.
- ROBERTS, G.P., GAWTHORPE, R.L., STEWART, I.S., 1993. Surface faulting within active normal fault zones: examples from the Gulf of Corinth Fault System, Greece. *Zeitschrift für Geomorphologie, Suppl.-Bd.*, 94, 303-328.
- ROBERTS, S. & JACKSON J., 1991. Active normal faulting in central Greece: an overview. In: Roberts, A.M., Yielding, G., Freeman, B. (Eds), *The geometry of Normal Faults*. Geol. Soc. London, Spec. Publ. Vol 56, 125-142.
- ROZOS, D.E., 1991. Engineering-geological conditions in Achaia Province. Geomechanical characteristics of the plio-pleistocene sediments. In: *Engineering geology investigations No. 16*. Institute of Geology and Mineral Exploration-Athens.
- RYBAR, J., KOSTAK,B., CZURDA, K., FECKER, E., SCHWEIZER, R., 2001. Verschiebungsmessungen an der östlichen Randverwerfung des Rheingrabens. *Geotechnik, Sonderband zur 13. Nationale Tagung für Ingenieurgeologie*, 41-48.
- SABINS, F.F. 1996. *Remote Sensing: Principles and interpretation*. 3rd ed., -394., Freeman and Company, New York.
- SACHPAZI, M., CLEMENT, CH., LAIGLE, M., HIRRN, A., ROUSSOS, N., 2003. Rift structure, evolution and earthquakes in Gulf of Corinth, from reflection seismic images. *Earth and Planetary Science Letters* 216, 243-257.
- SCHMIDT-HATTENBERGER, C., BORM, G., 1998. Bragg Grating Extensometer Rods (BGX) for Geotechnical Strain Measurements. *Proc. SPIE Workshop Opt. Fiber Sens.*, vol. 3483, 214-217.
- SCHMIDT-HATTENBERGER, C., NAUMANN, M., BORM, G., 2003. Fiber Bragg grating strain measurements in comparison with additional techniques for rock mechanical testing. *Sensors Journal, IEEE*, vol. 3, No. 1, 50-55.
- SEGER, M., ALEXANDER, J., 1993. Distribution of Plio-Pleistocene and Modern coarse-grained deltas south of the Gulf of Corinth, Greece. *Spec. Publs. Int. Ass. Sediment.* 20, 37-48.
- SIEGAL, B.S., GILLESPIE, A.R., Eds. 1980 *Remote Sensing in Geology*. -701p., Willey & Sons, New York.
- SOREL, D., 2000. A Pleistocene and still-active detachment fault and the origin of the Corinth-Patras rift (Greece), *Geology*, 28, 83-86.
- SPRENGER, W.L., 1996. Das Periadriatische Lineament südlich der Lienzer Dolomiten. *Abh. Geol. B.-A.*, 52, 1-120.

- STEFATOS, A., PAPANTHEODOROU, G., FERENTINOS, G., LEEDER, M., COLLIER, R., 2002. Seismic reflection imaging of active offshore faults in the Gulf of Corinth: their seismotectonic significance. *Basin Research* 14, 487-502.
- STEMBERK, J., KOSTAK, B., VILIMEK, V., 2003. 3D monitoring of active tectonic structures. *Journal of Geodynamics*, vol. 36, 103-112.
- STROMEYER, D., 2001. Finite Element Program system GT_32 (GTE 3.2, GTF 3.2, GTG 3.2)
- STOURNARAS, G., TSIMPIDIS, G., TSOUMANIS, P., YANNATOS, G., GUILLANDE, R., 1998. Instability Phenomena in the Neogene Deposits of Northern Peloponnesus, Greece. *Bull. Eng. Geol. Env.* 57, 65-68.
- TIBERI, C., DIAMENT, M., LYON-CAEN, H., KING, T., 2001. Moho topography beneath the Corinth Rift area (Greece) from inversion of gravity data. *Geophysical Journal International*, 145, 797-808.
- TSELENTIS, G. A., MAKROPOULOS, K., 1986 Rate of crustal deformation in the Gulf of Corinth (central Greece) as determined from seismicity. *Tectonophysics*, 24, 55-61.
- ZELILIDIS, A., KOUKOUVELAS, I., DOUTSOS, D., 1988. Neogene paleostress changes behind the forearc fold belt in the Patraikos Gulf area, western Greece. *N. Jb. Geol. Paläont. Mh.*, 1988, 21, 311-325.

Appendix

§1 Geological map of the area south of Aegion



§2 Interpretation of the linear grids on the TM71 indicators

The linear grids on each TM 71 indicator provide a way to measure rotation about an axis perpendicular to each indicator plane. Each indicator contains two linear grids perpendicular to each other (fig. 4.2 and 4.1). The Moiré pattern appears as parallel fringes across the grids. The following equation describes the relation of the rotation $\Delta\gamma$ with the fringe density a_n/b_n .

$$\Delta\gamma = \arctg \left| \frac{r * a_n}{b_n} - \frac{r * a_{n-1}}{b_{n-1}} \right|$$

where: $\Delta\gamma$ is the amount of the rotation in radians

r is a constant of 0.01mm

a_n is the number of fringes

b_n is the length of the pattern

a_{n-1} is the previous number of fringes

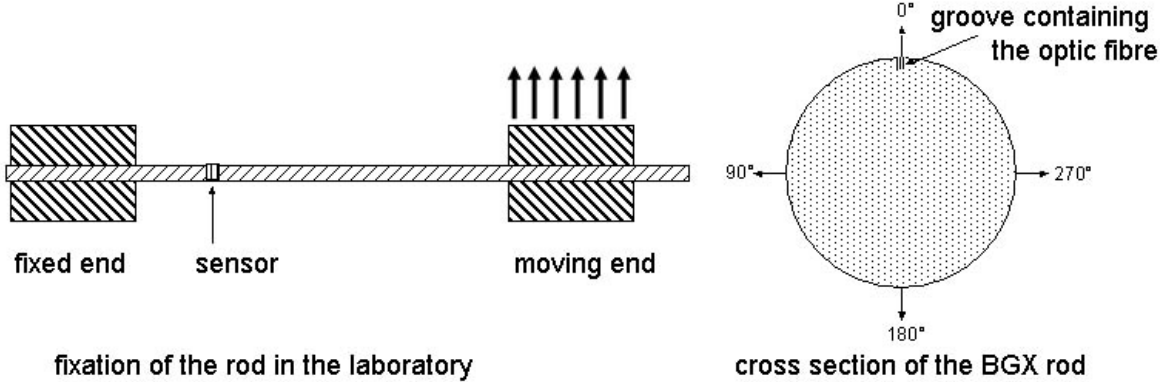
b_{n-1} is the previous length of the pattern

For better accuracy, the grid with the higher density of fringes should always be preferred to calculate the rotation. In this case the direction of rotation should be considered as positive for a density increase in the grid parallel to the instrument bridge (or negative for a density decrease) and negative for a density increase in the linear grid perpendicular to the instrument bridge (or positive for a density decrease) (KOSTAK 1991). The unmovable object is determined in the same way as for the displacement calculations. The accuracy is $3.2 \cdot 10^{-4}$ rad (STEMBERK 2003).

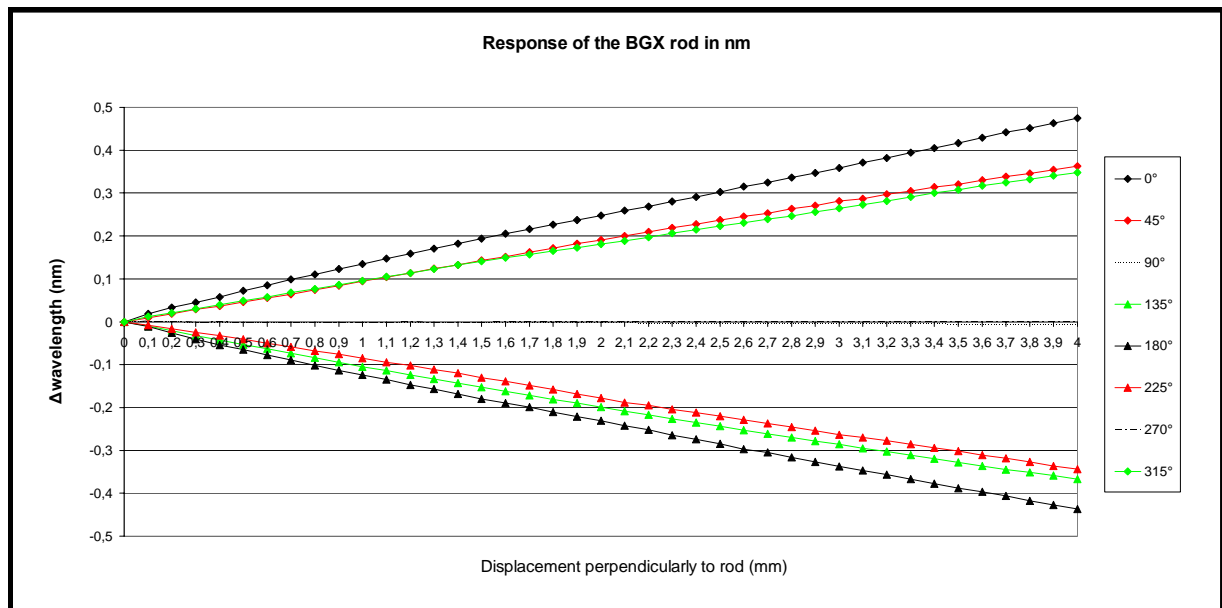
§3 Investigation of the performance of the BGX rod for displacements perpendicularly to it

The Bragg-grating extensometers that were used in the present study are equipped with one optic fibre which was embedded in a groove along the fibreglass rod near its surface (see following schematic). This allows the Bragg Grating sensor within the optic fibre to be axially strained also when the rod is bent because it then belongs to a convexity or concavity.

In order to inspect the sensitivity of these BGX rods to bending, a laboratory test was carried out which simulated the installation of the BGX rods at the fault monitoring sites. I.e. this test simulated a BGX rod with both ends firmly fastened along several centimetres of their length. One end was kept stable while the other was displaced perpendicularly to the rod as shown in the following schematic.



This configuration forced the deformation to take place on the middle segment of the rod containing the sensor and simulated the motion between two fault sides (footwall and hanginwall) moving laterally to each other. The movement was directed perpendicularly to the rod at different angles with respect to the position of the groove containing the optic fibre. The response of the system is described in the following diagramm.



The displacement perpendicular to the BGX rod was induced in increments of 0.1mm and reached a maximum of 4mm. By observing the diagram above it is obvious that:

-the results are subject to more than one interpretations. For example, the curves corresponding to the displacements directed at 45° and 315° with respect to the position of the optic fibre on the cross section of the rod are identical. This is also happening for other angles such as for 90° and 270° or for 135° and 225°. Also different combinations of displacement and direction produce the same change of wavelength. For example, 1mm displacement directed at 45° with respect to the position of the optic fibre induces a Δ wavelength of 0,1nm. The same Δ wavelength is induced by 0.7mm displacement directed at 0° with respect to the position of the optic fibre.

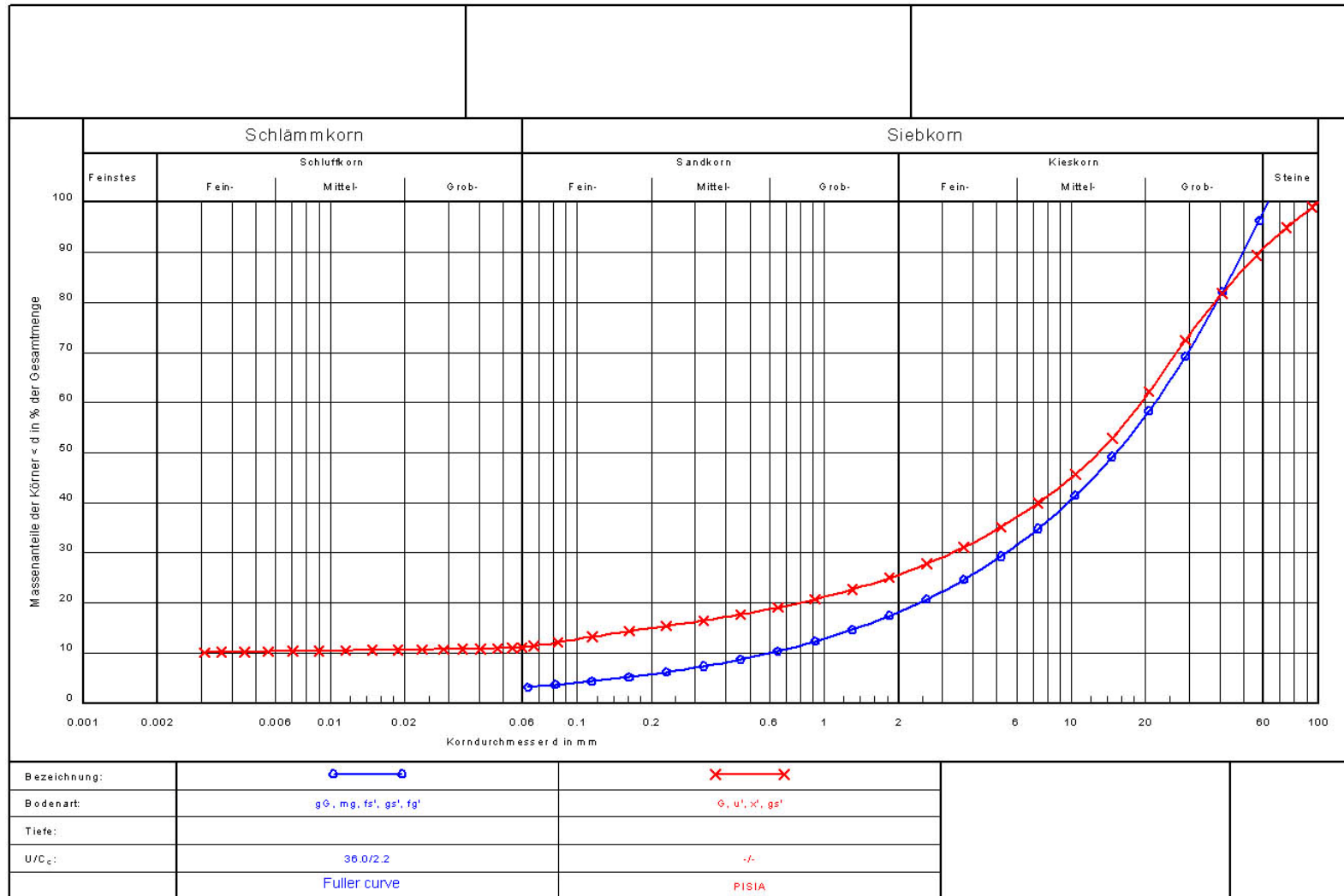
-for displacements directed at an angle of 90° or 270° in with respect to the position of the optic fibre, the reflected wavelength does not change.

Apart from the uncertainties described above, an axial deformation of the BGX rod i.e an elongation or shortening of the rod induces a substantially higher change of wavelength. For instance, 1mm elongation of the BGX rod induces a Δ wavelength of ca. 3.1nm (when the free length between the fixed parts is ca 39.5cm as at “Pisia monitoring” site). Whereas, a displacement of 1mm perpendicular to the rod, can cause a Δ wavelength between 0nm and 0.13nm (depending on the direction in respect with the position of the optic fibre). As a result, in case of simultaneous axial strain and bending of the rod the response to the axial strain

substantially overprints the response to bending. Therefore, in cases of installations such as those at “Pisia” and “Shinos A” monitoring sites, it is plausible to interpret the changes of wavelength only as elongation or shortening of the rod (1dimensional measurements) and neglect possible effects from movements perpendicularly to it.

§4 Grain size distribution of the pleistocenic material at the hanging wall of the fault at the “Pisia” monitoring site

The grain size distribution of the pleistocenic is similar to the respective Fuller curve .



§5 Fault displacements at the monitoring sites, measured by means of TM71

| Displacements at "Pisia" monitoring site | | | |
|--|--|------------------|---------------|
| date | Displacement perpendicular to the fault plane (mm) | Strike-slip (mm) | Dip-Slip (mm) |
| 23.02.2002 | 0 | 0 | 0 |
| 09.05.2002 | -0.11 | 0.36 | -0.04 |
| 29.07.2002 | 0.24 | 0.22 | 0.37 |
| 11.10.2002 | 0.24 | 0.13 | 0.53 |
| 03.01.2003 | -0.14 | 0.44 | 0.49 |
| 02.03.2003 | -0.23 | 0.84 | 0.49 |
| 19.06.2003 | 0.01 | 0.88 | 0.67 |
| 24.11.2003 | 0.17 | 0.66 | 1.04 |
| 22.03.2004 | -0.13 | 1.32 | 0.89 |
| 20.09.2004 | 0.56 | 1 | 1.28 |
| 01.08.2005 | 0.62 | 1.5 | 1.39 |

| Displacements at "Shinos A" monitoring site | | | |
|---|--|------------------|---------------|
| date | Displacement perpendicular to the fault plane (mm) | Strike slip (mm) | Dip-slip (mm) |
| 11.10.2002 | 0.00 | 0.00 | 0.00 |
| 03.01.2003 | 0.01 | 0.04 | -0.06 |
| 02.03.2003 | 0.02 | 0.08 | -0.09 |
| 19.06.2003 | -0.04 | 0.02 | -0.10 |
| 24.11.2003 | 0.01 | -0.02 | -0.05 |
| 22.03.2004 | 0.02 | 0.04 | -0.04 |
| 20.09.2004 | -0.04 | -0.05 | -0.05 |
| 01.08.2005 | -0.06 | -0.10 | -0.06 |

| Displacements at "Shinos B" monitoring site | | | |
|---|--|------------------|---------------|
| date | Displacement perpendicular to the fault plane (mm) | Strike slip (mm) | Dip-slip (mm) |
| 05.03.2003 | 0.00 | 0.00 | 0.00 |
| 19.06.2003 | 0.78 | 0.34 | 3.84 |
| 24.11.2003 | 2.57 | -0.64 | 0.52 |
| 22.03.2004 | 0.13 | -0.03 | 0.26 |

Displacement perpendicular to the fault plane: (+) extension (opening of the fault gap)
 (-) contraction (closing of the fault gap)

Strike-slip: (+) sinistral (-) dextral

Dip-slip (+) normal slip (-) reverse slip

§6 Fault displacements at the monitoring sites. measured by means of BGX

| Displacement perpendicularly to the fault plane at "Pisia" monitoring site | |
|--|-------------------|
| date | Displacement (mm) |
| 10.05.2002 | 0.00 |
| 03.01.2003 | -0.09 |
| 24.11.2003 | -0.06 |
| 22.03.2004 | -0.29 |
| 20.09.2004 | 0.11 |
| 01.08.2005 | 0.13 |

| Displacement perpendicularly to the fault plane at "Shinos A" monitoring site | |
|---|-------------------|
| date | Displacement (mm) |
| 03.01.2003 | 0.000 |
| 24.11.2003 | -0.007 |
| 22.03.2004 | 0.005 |
| 20.09.2004 | 0.006 |
| 01.08.2005 | 0.009 |

Displacement perpendicular to the fault plane: (+) extension (opening of the fault gap)
(-) contraction (closing of the fault gap)

List of Publications

- G. Maniatis, Ch. Lempp & H. Heinisch** (2002): 3D Monitoring of onshore active faults in the region of the Gulf of Corinth (Greece). Abstract Volume of Int. Workshop Active Faults: Analysis, Process and Monitoring, 89-92, Univ. di Camerino/It., 3-6 May 2002, Camerina/It..
- G. Maniatis, Ch. Lempp & H. Heinisch** (2002): 3D Monitoring of onshore active faults. Poster, Abstract, DFG-SPP ICDP/ODP, Potsdam 6-8 June 2002.
- G. Maniatis, Ch. Lempp & H. Heinisch** (2003): 3D strain monitoring of onshore active faults at the eastern end of the Gulf of Corinth (Greece). Journal of Geodynamics, 36, 95-102, Pergamon/Elsevier.
- G. Maniatis, Ch. Lempp & H. Heinisch** (2004): 3D monitoring of onshore active faults in the region of the Gulf of Corinth (Greece). In: Active faults: analysis, processes and monitoring, COST-action 625. Studi Geologici Camerti Vol. Spec. 2004, 79-82.
- G. Maniatis, Ch. Lempp & H. Heinisch** (2005): 3D Monitoring of Onshore Active Faults in the Region of the Gulf of Corinth (Greece). Abstract, Geophysical Research Abstracts Vol. 7, 02523, European Geosciences Union 2005
- G. Maniatis, Ch. Lempp & H. Heinisch** (2005): 3D Monitoring of Onshore Active Faults in the Region of the Gulf of Corinth (Greece). Poster, EGU Meeting, Vienna, Austria, 24 – 29 April 2005.

Lebenslauf

Name: Georgios Maniatis

Geburtsdatum: 19.04.1975

Geburtsort: Sparta

Schulbildung:

1981 - 1987 Griechische Volksschule in Sparta

1987 - 1990 Griechisches Gymnasium in Sparta

1990 - 1993 Griechische gymnasiale Oberstufe in Kesariani, Athen

Studium:

1993 - 1999 Geologie-Studium (Diplom) an der Nationale und Kapodistrias Universität Athen, Griechenland

1999 - 2000 „International Masters Course: Tropical Hydrogeology“ (MSc) an der Eberhard-Karls-Universität Tübingen

2000 - 2005 Promotion, Fachbereich Geowissenschaften, Martin Luther Universität Halle Wittenberg

Berufsweg:

06/2001-07/2001 Wissenschaftlicher Mitarbeiter, GFZ Potsdam, Berlin

08/2001-02/2002 Wissenschaftlicher Mitarbeiter, DFG Project „Golf von Korinth“ Fachbereich Geowissenschaften, Ingenieurgeologie Prof. Lempp und Allgemeine Geologie, Prof. Heinisch, Martin Luther Universität Halle-Wittenberg

03/2002-12/2004 Stipendiat, Fachbereich Geowissenschaften, Martin Luther Universität Halle-Wittenberg

Erklärung

Hiermit erkläre ich, dass die vorliegende Arbeit mit dem Titel “Quantification of the Activity of Tectonic Fault Systems in the Region of the Gulf of Corinth (Greece)” von mir selbständig und ohne fremde Hilfe verfasst wurde. Ich habe keine anderen Hilfsmittel und Quellen als die in der Arbeit genannten benutzt. Wörtlich oder inhaltlich aus fremden Werken benutzte Stellen habe ich als solche kenntlich gemacht.

Georgios Maniatis